PONTIFICIA UNIVERSIDAD CATÓLICA DE CHILE
SCHOOL OF ENGINEERING

ELECTROCHEMICAL AND TRIBOLOGICAL EVALUATION OF POROUS TI ALLOYS FOR ORTHOPEDIC USE

CAROLINA ANDREA GUERRA FIGUEROA

Thesis submitted to the Office of Graduate Studies in partial fulfillment of the requirements for the Degree of Doctor in Engineering Sciences

Advisors:
MAGDALENA WALCZAK
MAMIÉ SANCY

Santiago de Chile, September 2020

PONTIFICIA UNIVERSIDAD CATOLICA DE CHILE

SCHOOL OF ENGINEERING

ELECTROCHEMICAL AND TRIBOLOGICAL EVALUATION OF POROUS TI ALLOYS FOR ORTHOPEDIC USE

CAROLINA ANDREA GUERRA FIGUEROA

Members of the Committee:

MAGDALENA WALCZAK DocuSigned by: 4404B94C10BD452...

MAMIÉ SANCY DocuSigned by: 8822...

JORGE RAMOS 3C9E909C56D64B4...

NÉSTOR ESCALONA DocuSigned by: FE...

CLAUDIO AGUILAR FA0897AFF1184F7...

HERCÍLIO GOMES DE MELO DocuSigned by: 8E3EA09A8BCB4CB...

JUAN DE DIOS ORTÚZAR DocuSigned by: 376BE4D3F7A24BE...

Thesis submitted to the Office of Graduate Studies in partial fulfillment of the requirements for the Degree Doctor in Engineering Sciences

Santiago de Chile, September, 2020

ACKNOWLEDGEMENTS

Firstly, I would like to manifest my motivation to entered the doctoral program. Always I wanted to be a professor, and although I still want it with all my strength, I think the research is also my passion that I would like to explore further. Since I was a child, my vocation was to be a professor, because I love to teach and to amaze others with something that they have not considered or have not thought about. It is like when they tell you how your favorite cookies are made (at an industrial level), a small space is opened up in mind that needs to be filled. In essence, it opens up the curiosity spirit. That is what I like to see when I teach someone else, interest to understand the world.
On the other hand, to investigate is to be in a continuous questioning state of wanting to know, and what happens if? It is a timeless exercise that you think today to project and predict to the future based on the past. I compare this with video games; when you go unlocking stages, and you advance, you are increasing your spectrum, leaving places to explore, gaps where you passed, and you can always return, but looking ahead to continue the challenge. So I already feel trapped, and I like what I see.

I think writing a thesis is not a simple job, let alone an acknowledgment. This because I believe I could not write the name of all people who have participated and collaborated in this doctoral study hierarchically. Another reason is that I am afraid to forget someone inside these lines, and finally, because I have so many names that I am worried about required more than one page. However, I know that I would like to thank and dedicate this thesis to the people who have been with me all this time, have supported me, and have placed their trust in me. Thanks to all those who have taught me and those who have been supported my training. So for all of them, THANK YOU VERY MUCH, we have achieved it as a team.

Finally, I would like to thank the organization that provided the primary funding to this work: The National Commission for Scientific and Technological Research (CONICYT), which granted principally by PFCHA/DOCTORADO BECAS CHILE/2019 N°21190220 and Fondecyt grant N°1160604. I also thank full to Pontificia Universidad Católica de Chile grant through both the scholarship granted by VRI and Engineering Department, which partially funded this doctoral study in Chile.

TABLE OF CONTENTS

PONTIFICIA UNIVERSIDAD CATÓLICA DE CHILE

SCHOOL OF ENGINEERING

ELECTROCHEMICAL AND TRIBOLOGICAL EVALUATION OF POROUS TI ALLOYS FOR ORTHOPEDIC USE

Thesis submitted to the Office of Graduate Studies in partial fulfillment of the requirements for the Degree of Doctor in Engineering Sciences

CAROLINA ANDREA GUERRA FIGUEROA

Abstract

The demand for materials used in biomedicine applications has grown in recent years, triggering the interest in study new metallic materials for orthopedic. Porous Ti-based alloys have demonstrated suitability for bone replacement, such as dental implants and hip prostheses since they have a similar elastic modulus to the bone. However, the presence of pores implies a broader surface in contact with body fluids, which presents a potential risk in terms of corrosion and/or wear, as metal ions, metallic particles into the bloodstream. In this context, the objective of this doctoral thesis was to explore Ti-based alloys with a porous structure and evaluate their degradation in simulated body solutions.

Therefore, samples were prepared by powder metallurgy with a variation of porosity percentages, which were characterized mainly by electrochemical and mechanical techniques.

The electrochemical results suggested that porous Ti-based alloy were not influenced by porosity percentage, since the passivity was maintained even in confined spaces. Thus, an increase in the corrosion rate did not occur. On the other hand, the porosity enhanced the biomechanical compatibility through elastic modulus. At the same time, the tribological properties showed that the presence of porous would avoid the three-body wear mechanism, enhancing the wear and coefficient of friction.

Members of the Committee:
MAGDALENA WALCZAK
MAMIÉ SANCY
JORGE RAMOS
NÉSTOR ESCALONA
CLAUDIO AGUILAR
HERCÍLIO GOMES DE MELO
JUAN DE DIOS ORTÚZAR

Keywords: Porous material; Orthopedic implants; Corrosion; Electrochemical performance; Elastic modulus; Tribological properties; Wear; Titanium alloy; Impedance spectroscopy; Potentiodynamic curves.

PONTIFICIA UNIVERSIDAD CATÓLICA DE CHILE

ESCUELA DE INGENIERÍA

EVALUACIÓN ELECTROQUÍMICA Y TRIBOLÓGICA DE TITANIO POROSO PARA USO ORTOPÉDICO

Tesis enviada a la Dirección de Investigación y Postgrado en cumplimiento parcial de los requisitos para el grado de Doctor en Ciencias de la Ingeniería

CAROLINA ANDREA GUERRA FIGUEROA

Resumen

La demanda de materiales utilizados en aplicaciones de biomedicina ha crecido en los últimos años, lo que ha provocado el interés por estudiar nuevos materiales metálicos. Las aleaciones porosas a base de Ti han demostrado su idoneidad para el reemplazo óseo, como los implantes dentales y las prótesis de cadera, ya que tienen un módulo de elasticidad similar al hueso. Sin embargo, la presencia de poros implica una mayor superficie en contacto con los fluidos corporales, lo que presenta un riesgo potencial en términos de corrosión y/o desgaste, como iones metálicos, partículas metálicas en el torrente sanguíneo. En este contexto, el objetivo de esta tesis doctoral fue explorar las aleaciones a base de Ti con estructura porosa y evaluar su degradación en soluciones corporales simuladas.

Por tanto, las muestras se prepararon mediante pulvimetalurgia con variación de porcentajes de porosidad, caracterizadas principalmente por técnicas electroquímicas y mecánicas.

Los resultados electroquímicos sugirieron que la aleación porosa a base de Ti no se vio influenciada por el porcentaje de porosidad, ya que la pasividad se mantuvo incluso en espacios reducidos. Por tanto, no se produjo un aumento en la velocidad de corrosión. Por otro lado, la porosidad mejoró la compatibilidad biomecánica a través del módulo elástico. Al mismo tiempo, las propiedades tribológicas mostraron que la presencia de poros evitaría el mecanismo de desgaste de tres cuerpos, mejorando el desgaste y coeficiente de fricción.

Miembros del comité
MAGDALENA WALCZAK
MAMIÉ SANCY
JORGE RAMOS
NÉSTOR ESCALONA
CLAUDIO AGUILAR
HERCÍLIO GOMES DE MELO
JUAN DE DIOS ORTÚZAR

Palabras clave: Material poroso; Implantes; Corrosión; Comportamiento electroquímico; Módulo elástico; Tribología; Desgaste; Aleación de Titanio; Espectroscopia de impedancia; Curvas potenciodinámicas.

PROLOGUE

The demand for materials used in biomedicine applications has grown in recent years, triggering the interest in developing new metallic materials for orthopedic use as well as new technologies of advanced manufacturing, to meet the high standards and necessities of an aging population. In this context, the objective of this doctoral thesis was to explore Ti-based alloys with a porous structure and evaluate their degradation in simulated body solutions. The primary premise for researching porous Ti-based alloys is the recently shown suitability for bone replacement, such as dental implants and hip prostheses, derived from the remarkable similarity of elastic modulus and the high porosity shown to favor osteointegration. However, the presence of pores implies a wider surface in contact with body fluids, which presents a potential risk in terms of corrosion and/or wear, as metal ions, metallic particles and other degradation products might be released into the bloodstream.

The research conducted within the scope of the present doctoral thesis has been made public by four scientific articles, all focusing on the understanding of the degradation process of the porous matrix obtained by powder metallurgy. The thesis is thus structured as follows: at the beginning, a general framework is developed, which includes the introduction, the bibliographic review, the methodology, and the principal conclusions, in order to show the most significant aspects of the thesis, as well as the future outlook, which is briefly developed. Towards the end, the scientific articles are presented, ordered according to the established objectives, where each one represents a chapter of the doctoral thesis. Firstly, **Article I**, which seeks to understand the differences between bulk and porous material from one of the most widely used Ti-based alloys. Then, **Article II**, which deals with a new titanium-based alloy with a fixed porosity percentage and its electrochemical behavior, which was studied during a month of monitoring, and corresponds to the second specific goal of the thesis. **Article III** studies a novel porous titanium alloy, with a variable of porosity percentage, which was characterized mechanically and electrochemically between 1 and 91 days of exposure. Additionally, auxiliary characterization methods were carried out to understand the influence of porosity percentages on the techniques mentioned above. Finally, **Article IV** addresses the tribological properties of the alloy studied in the previous article, regarding the porosity influence on the coefficient of friction and wear rate in dry conditions.

DISCLAIMER

This thesis is documented by the published articles listed below. These articles are included in the text of the thesis as chapters, preceded by general formulation and relevant description of the experimental work and pertinent analysis.

Article I. C. Martinez, **C. Guerra*,** M. Sancy*, C. Aguilar et al. (2020), "Effect of porosity on mechanical and electrochemical properties of Ti-6Al-4V alloy". *Electrochim. Acta*, vol. 338, . DOI: 10.1016/j.electacta.2020.135858.
ISI journal | First Quartile | Impact Factor (2019): 6.20.

Article II. **C. Guerra**, M. Sancy*, M. Walczak, C. Aguilar et al. (2018), "Evolution of oxide film on the internal porosity of Ti-30Nb-13Ta-2Mn alloy foam". *Electrochim. Acta*, vol. 283, pp. 676-682. DOI: 10.1016/j.electacta.2018.05.010.
ISI journal | First Quartile | Impact Factor (2019): 6.20.

Article III. **C. Guerra*,** M. Sancy*, M. Walczak, C. Aguilar et al. (2020), "Effect of added porosity on a novel porous Ti-Nb-Ta-Fe-Mn alloy exposed to simulated body fluid".
Material Science and Engineering: C. Vol. 111. DOI: 10.1016/j.msec.2020.110758.
ISI journal | First Quartile | Impact Factor (2019): 5.88.

Article IV. **C. Guerra**, M. Walczak*, M. Sancy, C. Aguilar et al. (2020), "Tribological performance of porous Ti-Nb-Ta-Fe-Mn alloy in dry condition". *Materials* vol. 13, pp. 3284. DOI:10.3390/ma13153284.
ISI journal | Second Quartile | Impact Factor (2019): 3.06.

1 INTRODUCCION

Currently, the world is experiencing a growth in population density, which is associated with a 5-year increase in people's life expectancy [1]. However, living longer does not mean having a better quality of life; in fact, it is estimated that diseases associated with the human musculoskeletal system will increase the disability of the population, even reaching about 45% for women [2]. For this reason, nowadays, there are several studies related to medical conditions in older people, who have high demands that will be even more frequent in the future. Such is the case of those diseases that are related to joint disorders: for instance, osteoarthritis, which is the most common condition of elderly males and females, resulting in hip replacement surgery [3, 4]. According to the US Office of the Surgeon General (US) [5], as people get older, they are 30% more likely to suffer a hip fracture when they are between 60 and 80 years old. It is also expected that in the United States, the THA (total hip arthroplasty) will increase by 174% by 2030 compared to 2005, which would result in the government spending $50 billion per year on hip and knee replacement Not only is the economy of a country affected when prosthetic surgeries increase, but also the quality of life in the family group can suffer the consequences of this issue. Therefore, extending the service life of the materials becomes imperative. The review burden can be seen as a general measure of arthroplasty success in a joint registry, as primary surgeries often fail. Between 2012 and 2017, about 12.4% of the total procedures were hip revisions in the US, while just in the UK, during 2017, there were 27,605 revisions after primary hip replacement [6]. It is even worse because the number of revisions for different causes is expected to triple after five years since the first procedure [6].

Within the first revisions dataset available for analysis, the most prevalent indications are the aseptic loosening in 24.3% of the cases, attributed to stress shielding [6], which is closely linked to the mechanical properties of the implant [7]. The stress shielding in hip prostheses occurs when the metallic stem implanted in the femoral bone is stiffer than the bone, because the body loads are now shared between the prosthesis and the bone structure. Then the bone is subjected to lower tensions, which could lead to a decrease in the bone mass due to the lack of stimulation of the surrounding bones, resulting in the loosening of the prosthesis and the need of a new implant [8,9]. A decrease in the elastic modulus (E), attempting to achieve bone value (30 GPa), has been seen as a successful process to improve the mechanic biocompatibility between the body and the material. That could be obtained by changes in the alloy composition [10] as well as by the incorporation of porosity to the metal matrix [11].

Ti and its alloys have been widely used as a bone replacement due to their mechanical properties, non-toxicity, and good corrosion resistance [12]. In particular, Ti-6Al-4V wt.%

is the most typical commercial alloy, which exhibits an elastic modulus between 90 and 110 GPa, while Ti-based alloys with Nb and Ta as alloying elements, which are stabilizers of the β-phase, decrease E around 30% getting values near to an average of 70 GPa [10,13]. However, this has not been sufficient to reach bone values.

On the other hand, the porosity addition is being explored to reduce further the stiffness gap between the human bone and the titanium implant [10,12]. This has been possible in part due to the "advanced manufacturing" development, and the revival of the powder metallurgy (PM) technique, which allows to produce scaffolds or metallic foams, as they are known. Several studies have reported that it is possible to achieve low E values between 5 and 25 GPa by using porous materials of different alloys and porosity percentages [14,15]. Nevertheless, changes in the alloy and the structure of the material can produce a drop on the yield strength from a mechanical point of view, and accelerate a degradation process by wear and corrosion [16,17]. The yield strength is diminished due to the porosity addition to a metallic matrix, since it provokes discontinuities in the material that imply that the plastic deformation begins earlier than expected [18]. Nonetheless, it has been observed that the alloying elements promote the eutectic Ti component and the formation of an intermetallic phase, like TiFe and TiMn, which would improve the yield strength and also the hardness of the alloy [19–22]. Therefore, the alloying elements should be chosen carefully, as well as the pore structure, to reduce the impact on the other properties.

Regarding the degradation process, tribological properties have been extensively studied, as joint replacements constitute one of the leading causes of the high rate of hip revisions [6]. Specifically, the Ti-based alloys are generally considered to have poor tribological properties [23], even when sliding against a softer material [10,24], requiring targeted alloying or coating. Moreover, there are few studies related to the wear of porous materials, making it challenging to clarify the influence of the porous structure on wear, lubrication, and friction.

It is well known that the addition of porosity increases the active area, which can influence the corrosion resistance. However, it is still not fully understood. Surface characterization techniques are often used to determine surface evolution and corrosion products, after exposure to a medium of interest, such as XPS, RAMAN, ICP, as well as electrochemical methods. Among the latter, the most widely used are Linear Sweep Voltammetry (LSV) and Electrochemical Impedance Spectroscopy (EIS), which allow material to be monitored in a simulated environment. Several studies suggest that porous Ti alloys would suffer corrosion damage as the porosity increases. Indeed, Xie *et al*. studied Ti-x%Mo (x = 4, 6, 8, and 10 wt.%) porous alloys [25–27] and found that higher corrosion resistance was linked to a lower porosity grade, that in turn was attributed to a decrease in the volume of open and interconnected pores [25–27].

On the other hand, Alves et al. [28] reported that a larger porosity amount of porous CP-Ti would slightly increase the corrosion current density (i_{corr}) and change the corrosion potential (E_{corr}). This was attributed to the lack of passivation inside pores due to the difficult diffusion of oxygen through them. In general, the authors believe that with increased porosity, E_{corr} may be shifted towards more negative values and accompanied by an increase in i_{corr} [29]. Nonetheless, it should be noted that i_{corr} values reported in literature lack information on the active area participating in the electrochemical reaction. In fact, while some works considered a 1 cm^2 area [25–27], others estimated the geometrical area [17], and an attempt is rarely made to estimate the real area using, for instance, geometrical relations and pore numbers [28]. Therefore, perhaps the i_{corr} has been overestimated due to the incorrect area estimation, which leads to a wrong interpretation.

This thesis work is aimed at understanding the effect of added porosity of a novel Ti alloy, in terms of mechanical and electrochemical properties. In this context, samples were prepared by PM with a variation of porosity percentages, which were characterized mainly by electrochemical and mechanical techniques. Auxiliary methods of characterization were employed as XRD, XPS, and FE-SEM to go further and seek a better understanding of the research.

2 LIERATURE REVIEW

This section describes the most salient aspects that were considered in the project: firstly, a review of the alloying elements of Ti regarding their influence on mechanical and electrochemical properties; secondly, the bibliographic background related to the mechanical properties of porous Ti-based alloys, such as the elastic modulus (E) and the wear resistance; finally, a brief literature revision regarding the electrochemical results and analysis of Ti-based alloys.

2.1 Selection of the alloy and its alloying elements

There is a wide range of metallic alloys that have been used as biomaterial for joint replacement, as well as for bone fixation. Among them are stainless steel (316L), cobalt-chromium (Co-Cr), and Ti-based alloys, which have been demonstrated to have adequate mechanical properties and high corrosion resistance in simulated body solutions. However, alloying elements such as Ni, Cr, Al, and Co are harmful to the body when they are released through particles or ions into the bloodstream [30]. These alloys, including CP-Ti and Ti-6Al-4V wt.%, belong to the first generation of biomaterials, which demonstrated to be stiffer compared with the cortical bone [10].

In particular, Ti and its alloys exhibit values around 110 GPa, at least three times higher than the human bone (~ 30 GPa), making the material mechanically non-compatible, which could trigger the most common aseptic failure of stress shielding [6,31]. In this sense, new research has been developed on material based on Ti, using Nb, Zr, Ta, and Mo as alloying elements, decreasing the elastic modulus of the alloy. It is worth mentioning that titanium has an allotropic transformation at 882°C, from α- to β-phase as the temperature increases; while Al, O, N and C are α-phase stabilizers, V, Nb, Mo and Ta are for the β-phase. In the crystalline systems, α-phase has a hexagonal closest packed (HCP), and β-phase corresponds to a body-centered cubic (BCC). It is a well-known fact that they exhibit different mechanical properties. Among them, the E of BCC is lower compared with HCP; therefore, several recent studies have mainly focused on the β-type titanium alloys [10]. Currently, other alloying elements are being researched to decrease E with high yield stress at low costs, like Fe and Mn [22,32]. Indeed, Louzguine et al. [33] studied the mechanical properties of Ti-35Fe wt.%, demonstrating that Fe is a β-Ti stabilizer achieving high strength, ductility, and an E of 149 GPa, in ingot condition. Zhou et al. studied the Ti-50Fe wt.% alloy, accomplishing a high corrosion resistance (i_{corr}=$1.15 \cdot 10^{-5}$ $A \cdot cm^{-2}$) after being immersed for 1 hour in 3.5 wt.% NaCl. Regarding Mn addition, Zhang et al. [34] studied the cell bioactivity in the Ti-Mn alloys with a low amount of Mn, determining that over 2 wt.% Mn would increase the cell metabolic activity and proliferation of human osteoblasts, which

makes this material a candidate for bone substitutes. Additionally, it has been demonstrated that a small quantity of Mn would exhibit suitable mechanical properties, as was reported by Alshammari et al. [32], who studied the Ti-xMn (x: 1, 5 and 10 wt.%). The study, which obtained the alloy through the Powder Metallurgy technique (PM), found that, using the stress-strain test, Ti-5Mn should have a balance in the mechanical properties of elongation and ultimate tensile strength.

2.2 Mechanical properties of bulk and porous Titanium alloys

2.2.1 Elastic modulus

In order to reduce E, several strategies have been used, such as the addition of new alloying elements, but also the modification of the material structure: for instance, adding pores to the metal matrix. As was mentioned previously, Ti and its alloys have an allotropic transformation at 882 °C, which changes from HCP to BCC, where α-type exhibits an elastic modulus similar to 105 GPa. The combination of α+β phases also has values between 90 and 110 GPa, while the β-type pure phase decreases by around 30%, getting 70 GPa as an average [10,13]. The β-phase stabilization and modification of alloy composition have not been enough to achieve the E of the bone (~30 GPa); therefore, it has been necessary to develop other strategies, such as incorporating pores into the metal matrix. Table 1 shows a summary of Ti alloys regarding their mechanical properties, such as E and tensile strength and their relationship with the alloy type/composition.

Table 1. Mechanical properties of biomedical titanium alloys [10].

Material	Standard	Modulus / GPa	Tensile strength / MPa	Alloy type
First generation biomaterials (1950-1990)				
CP-Ti (grade: 1-4)	ASTM 1341	100	240-550	α
Ti6Al4V ELI wrought	ASTM F136	110	860-965	α+β
Ti6Al4V ELI std. grade	ASTM F1472	112	895-930	α+β
Ti6Al7Nb wrought	ASTM F1295	110	900-1050	α+β
Ti5Al2.5Fe	-	110	1020	α+β
Second generation biomaterials (1990-to date)				
Ti13Nb13Zr wrought	ASTM F1713	79-84	973-1037	Metastable β
Ti12Mo6Zr2Fe (TMZF)	ASTM F1813	74-85	1060-1100	β
Ti29Nb13Ta4.6Zr	-	65	911	β
TiMo	ASTM F2066	-	-	β

Porous materials or metal foam based on Ti have obtained good results, reaching values between 0.4 and 100 GPa, as was reported by Singh et al. [35]. To estimate the E of porous

samples, Gibson-Ashby established a relationship between the E and the porosity percentage, as is shown in Eq. (1).

$$\frac{E}{E_S} = C \cdot \left(\frac{\rho}{\rho_S}\right)^n \quad (1)$$

where E and ρ are the elastic modulus and the density of the porous alloys, while E_s and ρ_s represent a bulk (completely dense material) alloy. C and n denote the coefficient and exponential, respectively, where commonly n takes a 0.5 value, and the C constant varied between 0.1 and 4 [18]. In this context, several studies have been carried out on novel porous alloys obtained by different methods, such as additive manufacturing and Powder Metallurgy (PM). The reviews are focused, among others, on the variation of the porosity percentage, the control of the pore size, and the powder particle size, and they study the appropriate combination to obtain a less stiff material not susceptible to cracks [14].

2.2.2 Tribological properties

Tribological properties have been extensively studied regarding joint replacements, like hips and knees, since they constitute 14.1% of the total post-surgery revisions [6]. Particularly in hip arthroplasty, it is due to the wear of paired materials as metal-polymer, metal-ceramic, or metal-metal, which, when in contact with each other, can produce the degradation of one of the parts. One of the risks involved is that the wear debris which is released could interact with tissue, resulting in bone resorption and ultimately leading to the loosening of the implant, as shown in a simplified schematic in Figure 1 [36,37]. The other risk is the luxation or dislocation of the implant associated with the wear of the pair of materials, which causes a transient loss of contact [38]. It should be noted that the femoral heads are the pieces of a hip prosthesis, which suffer more wear [36,39].

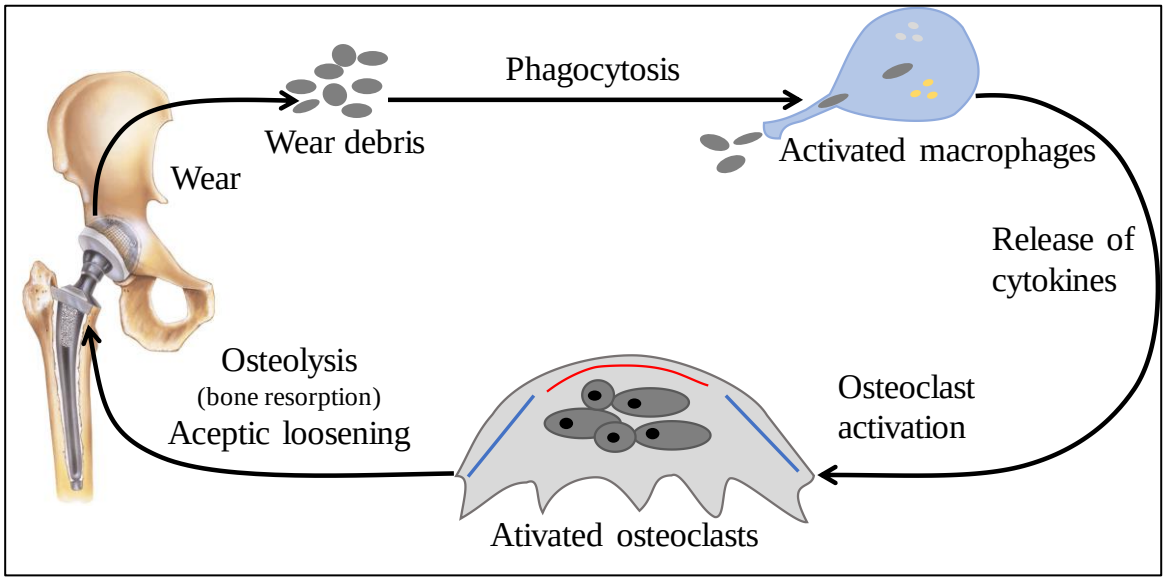

Figure 1. Simplified schematic of an inflammatory response triggered by wear debris leading to bone resorption and aseptic loosening [37].

In consequence, wear and friction are valued tests in the joint implant research field, due to the issues related to them. Ti and its alloys have demonstrated to have poor tribological properties [23], such as high and unstable friction, severe adhesive wear, low resistance to abrasion, susceptibility to fretting wear, and a strong tendency to seize [10,39]. Xia [40] directly compared the wear of γ-based Ti-48Al-2Nb-2Cr-1B with the work-horse, Ti-6Al-4 V, sliding against an 8-mm WC ball under 10 N load without lubrication. The results revealed that the γ-based Ti-48Al-2Nb-2Cr-1B displays very high wear volumes, almost the same as the Ti-6Al-4V alloy, with an average wear rate of 2.55×10^{-3} mm^3m^{-1} [39]. With regard to porous materials and tribological properties, only a few studies have been carried out. Liu et al. [41] reported reduced resistance to wear of CP-Ti porous (commercially pure Ti) as evaluated by the coefficient of friction (COF) and wear. Although the porous materials presented even worse tribological properties, Choi et al. [42] showed the potential of improving the wear resistance of Ti-foam through the incorporation of alloying elements.

2.3 Electrochemical behavior

Electrochemical techniques are highly useful to understand the material's reaction and its evolution when exposed to a medium of interest. The relevance lies in the possibility to monitor the unfolding of the surface and determine mechanisms that affect them like passivation, reduction of species, and diffusion, among others. A summary of the electrochemical responses of bulk and porous titanium alloys is presented below, emphasizing the most remarkable characteristics found in the literature, using two electrodynamic techniques.

2.3.1 Linear sweep voltammetry (LSV)

Potentiodynamic curves or LSV have been extensively studied on flat surfaces in Ti-based materials. Titanium exposed to simulated body fluid (SBF) solutions has been found to have low current densities (i_{corr}), around 0.04 $\mu A \cdot cm^{-2}$ for Ti-6Al-4V wt.% at 37 °C, which is lower than for other alloys also used in orthopedic implants, such as stainless steel (i_{corr} of 0.4 $\mu A \cdot cm^{-2}$) [43]. As an example, Figure 2 shows a comparative LSV of different alloys also used as prosthesis, while Table 2 summarizes several Ti-based alloys and electrochemical parameters. It has been reported that the passive range of Ti alloys fluctuates between 300 mV and 600 mV, whereas the pitting potential occurs at an overpotential close to 500 mV [43]. Therefore, Ti-based alloys are considered good candidates for orthopedic use. However, it is still not well known how passivation might be affected by porosity addition, since this implies a rise in the total effective area in contact with the body fluid.

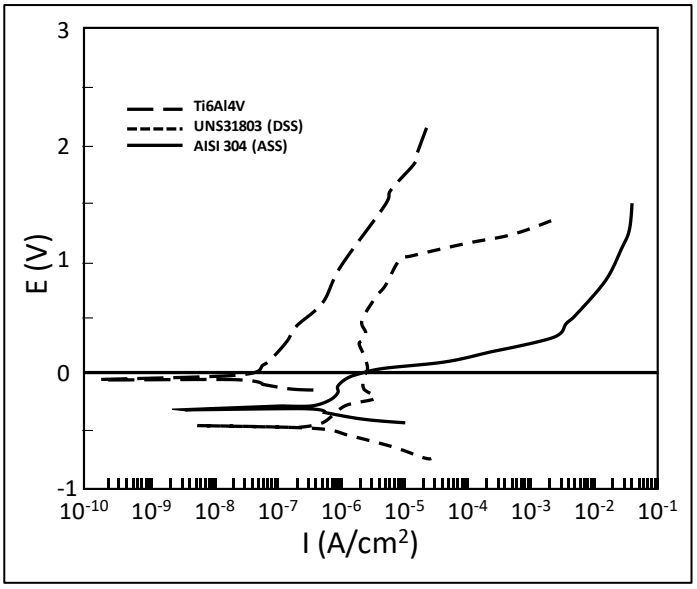

Figure 2. LSV curve comparison of orthopedic alloys as Ti-6A1-4V, duplex stainless steel, and austenitic stainless steel in SBF solution [43].

As of today, there are around fourteen works of porous titanium-based materials for orthopedic use, where it is mainly indicated that the increase of the area in contact with the electrolyte worsens the performance of the material against corrosion [29]. As shown in Figure 3, where the corrosion currents increase by two orders of magnitude with respect to the material without porosity, the resistance to corrosion is affected. However, Guerra et al. [29,44] studied the behavior of porous materials by electrochemistry, concluding that there is indeed a shift in the potential of corrosion (E_{corr}) towards negative values, through an increase of the porosity but not a significant increase in i_{corr}. The rise in i_{corr} was attributed to the difficulty of finding the right electroactive area for porous materials. Therefore, it

should be noted that an inaccurate estimate of the surface can conduce to significant errors in the interpretation of the data collected.

Table 2. Summary of literature data on electrochemical response of bulk Ti-based alloys relevant for biomedical applications

Alloy / wt.%	Fabrication method	Test medium at 37 °C	Electrochemical testing		Ref
			E_{corr} /mV vs. SCE	i_{corr} / μA·cm^{-2}	
CP-Ti	Treated	0.9 wt.% NaCl	-380 ± 42	0.13 ± 0.03	[45]
CP-Ti	Treated	SBF	-440	~10	[46]
Ti-6Al-4V	Treated	SBF	-420	~1	[46]
Ti-6Al-4V	Treated	SBF	-30	0.04	[43]
Ti-39Nb	Arc Melting	0.9 wt.% NaCl	-50	0.5	[47]
Ti-6Mo	Arc Melting	SBF		4.5 ± 0.4	[48]
Ti-10Mo	Arc Melting	SBF		3.8 ± 0.6	[48]
Ti-1Ag	Arc Melting	Artificial Saliva	−450 ± 20	5 ±2	[49]
Ti-3Ag	Arc Melting	Artificial Saliva	−290 ± 200	4.86 ± 3	[49]
Ti-10Ag	Arc Melting	0.9% NaCl	−400	−4.00	[50]
Ti-12Mo-13Nb	Arc Melting	SBF	47.4	3.77	[51]
Ti-10Mo-20Nb	Arc Melting	SBF	47.4	3.65	[51]
Ti-6Al	Arc Melting	SBF	−775 ± 12	0.241± 0.006	[52]
Ti-25Nb-10Ta-1Zr-0.2F	Arc Melting	SBF	−71.7	0.22	[53]
Ti-6Al-4V	Arc Melting	SBF	47.4	0.686	[54]
Ti-8Mo-6Nb-4Zr	Arc Melting	SBF	−301 ± 21	0.214 ± 0.07	[55]
Ti-13Nb-13Zr	Arc Melting	SBF	47.4	5	[56]
Ti-6Mn	CCLM**	SBF	−100 ± 15	0.0191 ± 0.001	[57]
Ti-5Mn-3Mo	CCLM**	SBF	−150 ± 15	0.0119 ± 0.002	[57]
Ti-6Mn-3Mo	CCLM**	SBF	−165 ± 20	0.0098 ± 0.002	[57]
Ti-12Mo	CCLM**	0.9% NaCl*	-701 ± 21	0.56 ± 0.07	[58]

*At 25°C

**Cold Crucible Levitation Melting

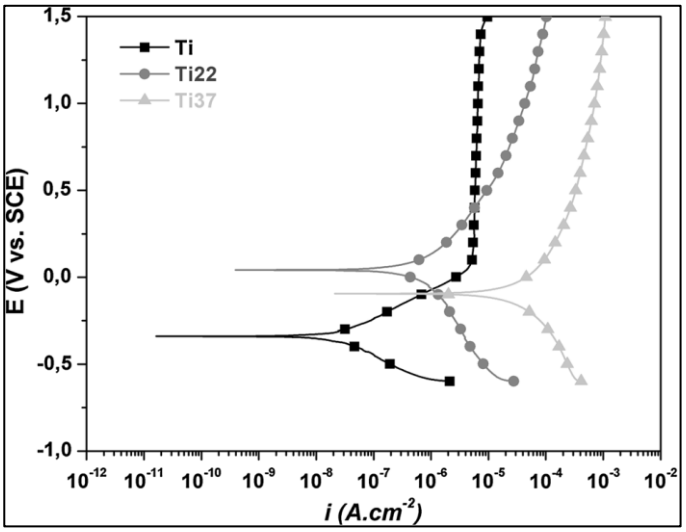

Figure 3. LSV curve of CP-Ti at different porosity percentages.

2.3.2 Electrochemical impedance spectroscopy (EIS)

Impedance spectroscopy studies of Ti-based alloys have focused on the description of the porous surface and its evolution after being exposed to SBF. The results have shown that the oxide layer suffers the most significant changes as time passes, as can be observed in Figure 4, which shows the evolution of Ti-6Al-4V after being exposed to the Hank solution at 37°C [59]. The high frequency (HF) range shows the oxide response, which varied after 168 h, and a second loop at the low frequency (LF), which was related to the double-layer capacitance. The increase in LF modulus after 168 h indicates the thickening of the passive layer on the surface, which was associated with an increase in corrosion resistance [59]. Similar behavior was also observed by Martinez et al. [44], who studied the Ti-Al-V alloy, demonstrating a stable behavior or slight increase in the total impedance modulus through 21 days of exposition to SBF.

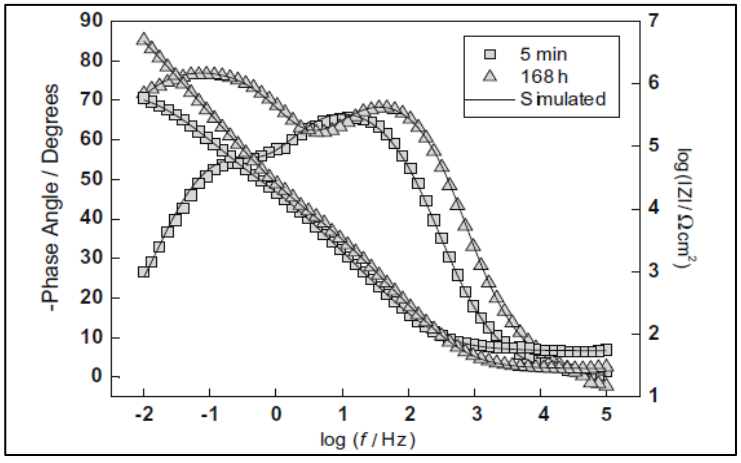

Figure 4. Bode diagram of Ti-6Al-4V as a function of immersion time in Hank solution [59].

Few studies have been carried out using the EIS technique in the description of porous Ti materials for orthopedic use. The studies that exist are generally oriented to batteries, to observe the charge and discharges of ions [60,61]. Nonetheless, the EIS model of porous materials has been well described by Lasia [62], who, based on the original De Levie model, described a linear transmission model that explains the drop of resistivities along with it. Figure 5 shows the model represented by a perfectly cylindrical pore of known dimensions.

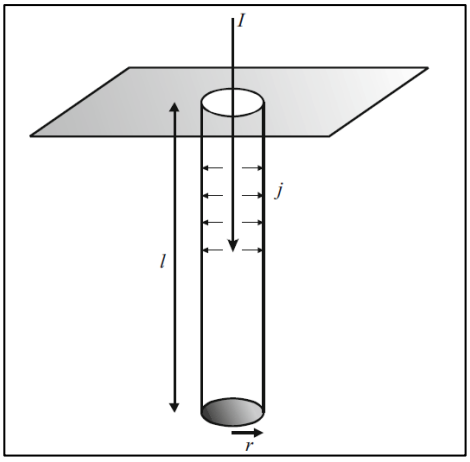

Figure 5. Model of a cylindrical pore with dimensions *l* and *r*, where the gray area is non-condutive. *I* represents the axial current flowing to the pore, and *j* the local current flowing to pore walls [62].

Commonly published articles that involve impedance analysis have suggested other equivalent circuits related to porous materials, which have a good mathematical fit, but a lack in the physical sense regarding material structure. Such is the case of Alves et al., who propose an equivalent circuit composed of three resistances and capacitances in parallel for the more porous material [28]. Itagaki et al.[60] proposed another model representing porous materials with pore size distribution and interconnection with each other: in other words, a fractal structure, which has a simulated response similar to that obtained experimentally by Guerra et al. [29,63]. This includes macro-, meso- and micro-pores that are interconnected with each other, a structure which is possible to obtain by additive manufacturing or PM with space holder.

3 HYPOTHESIS

The leading hypothesis of this work is that adding porosity to the Ti-based alloy obtained by powder metallurgy compromise neither the expected corrosion resistance of the alloy exposed to simulated body fluid nor the tribological response required for bio-applications. Moreover, the porosity allows improving the elastic biocompatibility of the material.

4 OBJECTIVES

4.1 Main goal

The main goal of this research is to study the porosity effect of Ti-based alloys on their electrochemical and tribological behavior through the time of exposure, in simulated body conditions.

4.2 Specific goals

- To characterize Titanium alloys electrochemically with varying porosity percentage, to evaluate the kinetics of the formation/dissolution of the passive layer.
- To quantify the changes in the overall porosity of the sample at different exposure times.
- To characterize the degradation process of porous Ti-alloys by tribological test.

5 METHODOLOGY

5.1 Fabrication of the porous alloys

5.1.1 Sample preparation

The Ti-30Nb-13Ta-2Mn at.% and the Ti-20Nb-11Ta-16Fe-1Mn at.% alloys were obtained through a mechanical alloying technique. Each pure metal powder (purity of 99.5%, particle size <45 μm, NOAH Technologies) was milled and mixed in a RETSCH PM400 ball mill for an effective duration of 50 h (on/off cycles of 15/15 min were used). Later, alloys were reached, under a protective Ar atmosphere and with a ball-to-powder weight ratio of 10:1 [63]. Ti-6Al-4V wt.% powder alloys were commercially acquired (purity 99.92%, sphere particle size 45-106 μm, AP&C) and also milled for 50 h. Then, all alloys were mixed with $(NH_4)_2CO_3$ (99%, Loba Chemie) as a space-holder, which was added in different percentages, from 0 to 50%. Finally, samples were obtained as cylinders of 8 and 6 mm of diameter and height, which were produced by uniaxial pressing at 400 MPa in a cylindrical die with an inner diameter of 8 mm. The thermal cycle to remove space-holder and sintering was 1.5 h at 180 °C followed by 3 h at 1250 °C in a protective Ar atmosphere. Moreover, bulk samples of Ti-20Nb-11Ta-16Fe-1Mn at.% were obtained from their powder alloy using Arc Melting (AM) and Spark plasma sintering (SPS) methods. The AM consisted of melting the powder in the Ar atmosphere, by using an electrode tip of tungsten, in a water cooler copper base. Later, the specimen was treated at 900 °C for 72 h in a high vacuum. The SPS technique achieved bulk samples at 1000 °C and 60 MPa for a 7-min holding time. The apparent porosity reached was around 3.5% and 4.2%, respectively. On the other hand, a bar Bulk Ti-6Al-4V wt.% alloy was commercially acquired and then cut into the same dimensions mentioned above.

5.1.2 Cleaning treatment

All samples were mechanically polished using SiC sandpaper with successive grit sizes, from #600 to #4000, until a polished surface was achieved. Ti-6Al-4V samples were also polished using polycrystalline diamond suspension with a size of 9, 6, and 2 mm, and colloidal silica suspension with a size of 0.05 mm as the abrasive agent. Finally, all samples were cleaned with alcohol in a sonicator bath for 10 min and stored in a vacuum.

5.2 Morphological and chemical characterization

5.2.1 Apparent porosity

Macroporosity of the samples was estimated by the Archimedes method, according to the Standard Test ASTM C373-88 [64] and under metallographic observation with optical microscopes (OM, Olympus 470). The specific surface and pore size distribution, for micro

and mesoporosity, were determined by the Brunauer–Emmett–Teller (BET) analysis from the N_2 adsorption/desorption isotherms (Micromeritics, 3 flex Physisorption). Additionally, the microstructure morphology and chemical composition were evaluated by a field emission-scanning electron microscope (FE-SEM, QUANTA FEG 250) equipped with an energy dispersive spectrometer (EDS).

5.2.2 XPS characterization

X-ray photoelectron spectroscopy (XPS) spectra of Ti-30Nb-13Ta-2Mn at.% and Ti-20Nb-11Ta-16Fe-1Mn were recorded using a ThermoVg K-alpha+ photoelectron spectrometer with Al Kα X-ray radiation (hν = 1486 eV). The analysis chamber was operated at 10^{-6} Pa, and C 1 s at 284.15 eV was used as a calibration reference. A complete survey scan and high-resolution scans of the Ta4f, Nb3d, Ti2p, O1s, Mn2p, and Fe2p signals were recorded. For depth profile characterization, a sputtering cycle was imposed consisting of 15 s Ar ions flux exposure at 3 keV. Prior to signal analysis, the spectra were processed to remove the background contribution caused by inelastically scattered electrons using the Shirley procedure. Curve fitting and peak decomposition were carried out using mixed Gauss-Lorentz shape function for each component. Furthermore, XPS spectra of Ti-Al-V were collected using an analysis chamber Phoibos 150 with a 1D-DLD detector monochromatic X-ray source: Focus 500 with an XR50 M with Ag/Al Anode. X-ray photoelectron spectroscopy data were analyzed with software Casa XPS Version 2.3.22. The energy scale of the spectra was calibrated in relation to the binding energy (BE) of advantageous hydrocarbons (CeC/CeH) in the C1s signal at 285.4 eV. High-resolution scans of the Ti2p, O1s, Al2p, and V2p signals were also recorded. Curve fitting and decomposition were performed after removing the Shirley-type background. A mixed Gausse-Lorentz shape was used for the different components.

5.2.3 XRD characterization

All X-ray diffraction (XRD) patterns were obtained using a multipurpose diffractometer (STOE STADI MP), equipped with a detector (DECTRIS MYTHEN 1K), and operating with Cu $K_{\alpha1}$-radiation (λ =1.54056 Å, curved Germanium (111) monochromator of the Johann-type) as a source. The crystallographic phases for the novel alloy were identified using MATCH! Software, comparing the combined peaks with patterns provided by crystallography open database (COD), whereas the crystallographic phases of Ti-Al-V were identified by the search-match algorithm, comparing the combined peaks with patterns provided by the X'pert HighScore database (Version: 2.1 b (2.1.2)).

5.3 Mechanical characterization

5.3.1 Elastic modulus

The elastic modulus was estimated using the transmission technique. For this, an electrical pulse was produced by an Agilent-33250A function generator and then amplified with a high-frequency amplifier NF-HSA4011 to excite the Olympus V110 ultrasonic transducer, inducing a mechanical wave in the sample. The wave is received by a transducer of the same model on the opposite side of the sample. The emitted and received waves are acquired with the Tectronix TDS-2012B oscilloscope with 1 ns of precision. With the acquired signals, the longitudinal and transversal wave speed (v_L and v_T) can be estimated using the length and diameter traveled by the pulse, employing a Mitutoyo micrometer wi th a 0.001 mm of accuracy, and the time delay that the wave takes to reach the other side. Then the E and Poisson modulus (ν) are calculated according to the ASTM International D2845-8 [65,66] standard in agreement with Eq.(2) and Eq.(3)

$$\nu = \frac{1-2\left(\frac{v_T}{v_L}\right)^2}{2-2\left(\frac{v_T}{v_L}\right)^2} \tag{2}$$

$$E = 2\rho {v_T}^2(1-\nu) \tag{3}$$

5.3.2 Tribological test

For the tribological testing, samples of Ti-46Ta-25Nb-12Fe-1Mn (at.%) with 0% porosity (obtained through SPS), 30%, and 60% porosity (obtained by PM) were mounted in a thermosetting resin. Then, they were cut and polished to get a suitable surface of low roughness, which was then cleaned using isopropyl alcohol. A ball-on-disc tribotester (NTR2 Nano tribometer produced by CSM Instruments) was used, set to oscillating mode, operated at 20±1 °C under technically dry conditions. As a counter specimen, Al_2O_3 balls of 2 mm of diameter were used, applying 1000 mN of load with a stroke of 0.6 mm (0.3 mm amplitude). The maximum linear speed was 1 $cm \cdot s^{-1}$, and the test was run for 100,000 cycles. Ball material and test parameters were selected on the base of preliminary tests. The wear tracks of tested specimens (three per sample) were analyzed using an optical profilometer (Talysurf CCI- Lite Non-contact 3D profiler), extracting three profiles from each sliding path: one central and two adjacents (100 μm from the central).

5.4 Electrochemical characterization

5.4.1 Electrochemical measurements

Electrochemical measurements were carried out using a three-electrode cell with a platinum rod as the counter electrode (CE) and a saturated calomel electrode (SCE) as the reference electrode (RE). The working electrode (WE) consisted of the Ti-based alloys that were mounted on a rotating disc electrode kit (OrigaTrod, Origalys) with an exposed geometric area of 0.28 cm^2. During the measurements, a thermostatic water bath was kept at 37±1 °C, and the rotation rate was set to 150 rpm. It should be noted that the sample holder was immersed in about 2 mm and held in this position throughout the exposure, including electrochemical characterization. Electrochemical measurements were carried out using a potentiostat/galvanostat (VSP, Biologic). Open circuit potential (OCP) curves were registered, and electrochemical impedance spectroscopy (EIS) data were collected after OCP values were stable. Impedance data were acquired over a frequency range from 25 kHz to 3 mHz with seven points per decade and using a 10 mV peak-to-peak sinusoidal voltage at E = OCP. The impedance results were fitted by using both a home-developed software called SIMAD (LISE UPR 15 CNRS, France) using the De Levie model for porous electrode response and a new model for fractal porous electrode developed by Itagaki et al. [60]. This consisted of fitting the experimental impedance data, rewriting the model (equivalent circuit) proposed in the software, using the frequency range suggested by the Kramers-Kronig relation, and repeating the adjustment every 1200 iterations until reaching the lowest $\chi 2$ value. Finally, polarization curves were performed starting from $E_1 = E_{OCP-100\ mV}$ vs SCE to $E_2 = E_{OCP+300\ mV}$ vs. SCE at a scan rate of 0.1 mV s^{-1}.

5.4.2 Quantitative analysis of metal ion release

In order to quantify the amount of released ions of the Ti-46Ta-25Nb-12Fe-1Mn (at.%) alloy, two methods were used: droplet measurements and electrochemical flow cell. The droplet measurement was carried out for the sample with 33% porosity and exposed for 30 days without renewing the SBF, to allow for accumulation of the released ions. About 150 mL of the SBF solution were sampled from the exposure system and stirred for 20 min. The solution was subsequently transported via a capillary toward the inductively coupled plasma (ICP) analyzer (Ultima 2C Horiba Jobin-Yvon), with a flow rate of 3 mL·min^{-1}, where the ions dissolved in the solution were quantified with a detection limit (DL) specific to each element, i.e., Ti (2.0 ppb), Nb (7.7 ppb), Ta (8.6 ppb), Mn (0.7 ppb) and Fe (3.2 ppb).

The electrochemical flow cell set-up, employed for the quantification of the metal ions released under polarization condition, was coupled to a potentiostat (Reference 600™, Gamry) and consisted of a three-electrode cell with a saturated calomel electrode (SCE) and a Pt wire as a reference and counter electrode, respectively. For the measurements, the

samples were mounted in an epoxy resin and then mechanically polished using emery/sandpaper grit up to #4000, cleaned by sonication in an alcohol bath for 10 min, and dried by blowing compressed air. Then, the samples were immersed in SBF for 30 days at 37±1 °C, using an arrangement coupled with an ICP system. In this case, a pumping system allowed a continuous injection and extraction of the SBF, and the extracted liquid was guided directly to the ICP-AES chamber (Ultima 2C Horiba Jobin-Yvon). A steady influx of the SBF at room temperature was introduced directly into the ICP-AES analysis at the rate of 3 $mL \cdot min^{-1}$. The measurements were carried out first at OCP, followed by applied potential of constant value (1 V or 2 V), and then during a linear sweep voltammetry carried out at the rate of 0.25 $mV \cdot s^{-1}$. During all the electrochemical manipulation, the ICP measurements elapsed in-line. Finally, the C_M and v_M (dissolution rate) were calculated using a standard calibration method of AESEC (atomic emission spectroelectrochemistry) technique [67].

6 MAIN RESULTS

The main results obtained during the doctoral study are presented below; most of them were discussed in-depth in the respective publications.

6.1 Morphological and surface characterization

Porous samples were observed by an optical microscope (OM), which allowed to obtain reconstructions of the metal surfaces, as shown in Figure 6. In this case, the dark area corresponds to the pores of Ti-20Nb-11Ta-16Fe-1Mn, while the light area corresponds to the alloy. Porous samples have shapes and size distribution that varied from 1 μm to 400 μm. The pores' size is crucial to the osseointegration since it could determine the vascularization and the fixation of the prosthesis by the bone. Ryan et al. and Matassi et al. observed an increase in the osseointegration when porous materials presented a hierarchical pore size distribution, from mesoporosity to macro-porosity, i.e., values from 20 nm to 600 μm [33, 34]. Figure 7 shows FE-SEM analysis, also revealing different pore sizes, where some of them are interconnected with each other, and others are isolated. The porosity percentage showed in each figure was estimated from the Archimedes method. The samples before exposure would have a lower porosity amount than those which were observed after 91 days of exposure, where it is clear that porosity was influenced by time after being immersed, suggesting a tendency to decrease in the first month of exposure and then to increase until the third month.

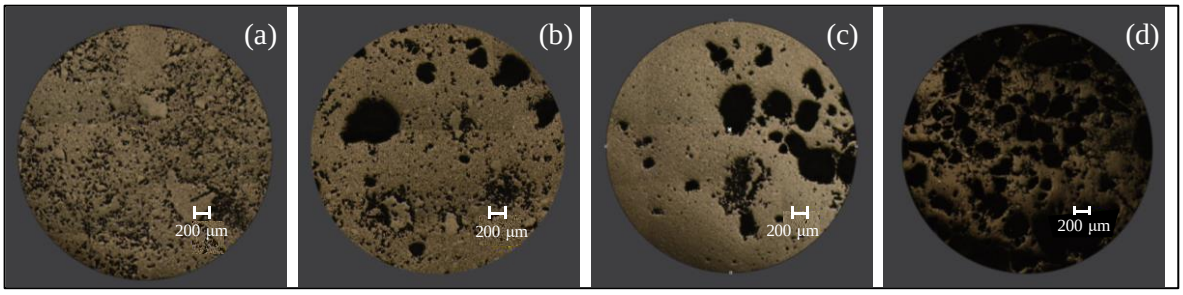

Figure 6. OM images of Ti-20Nb-11Ta-16Fe-1Mn with (a) 25%, (b) 31%, (c) 37% and (d) 46 % porosity prior to exposure.

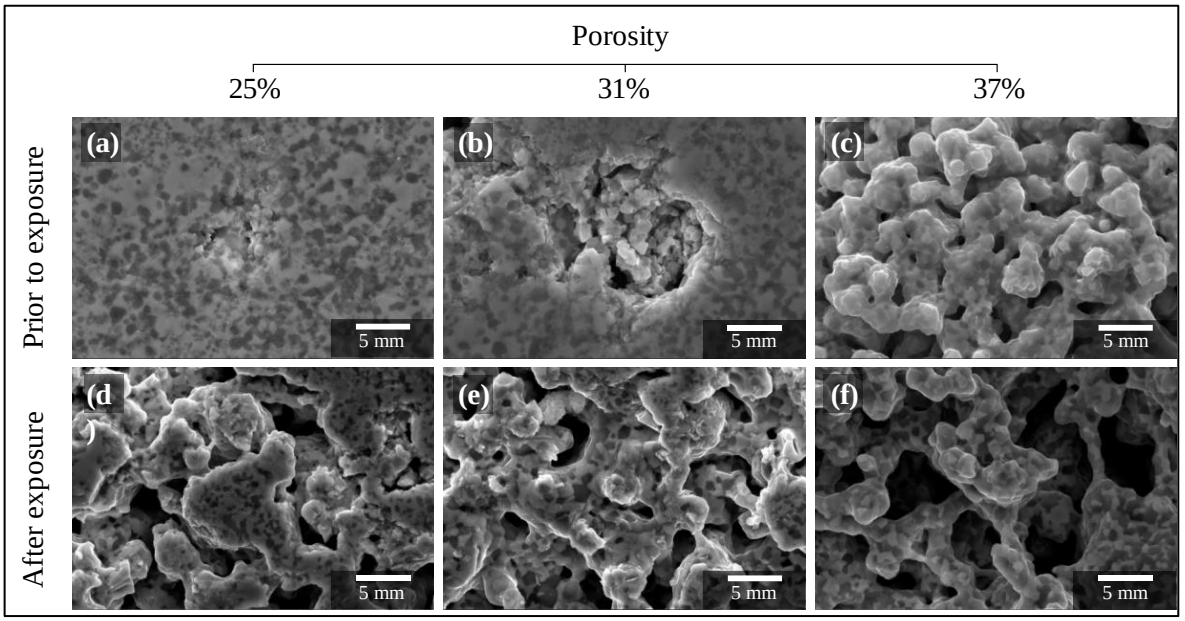

Figure 7. FE-SEM images of Ti-20Nb-11Ta-16Fe-1Mn before and after being exposed to simulated body fluid.

Figure 8 shows the variation of the pore volume of Ti-20Nb-11Ta-16Fe-1Mn that was obtained from adsorption/desorption isotherm. Although an increment in the pore volume <50 nm with an increase in the porosity percentage was revealed, the results showed that samples were mostly macroporous.

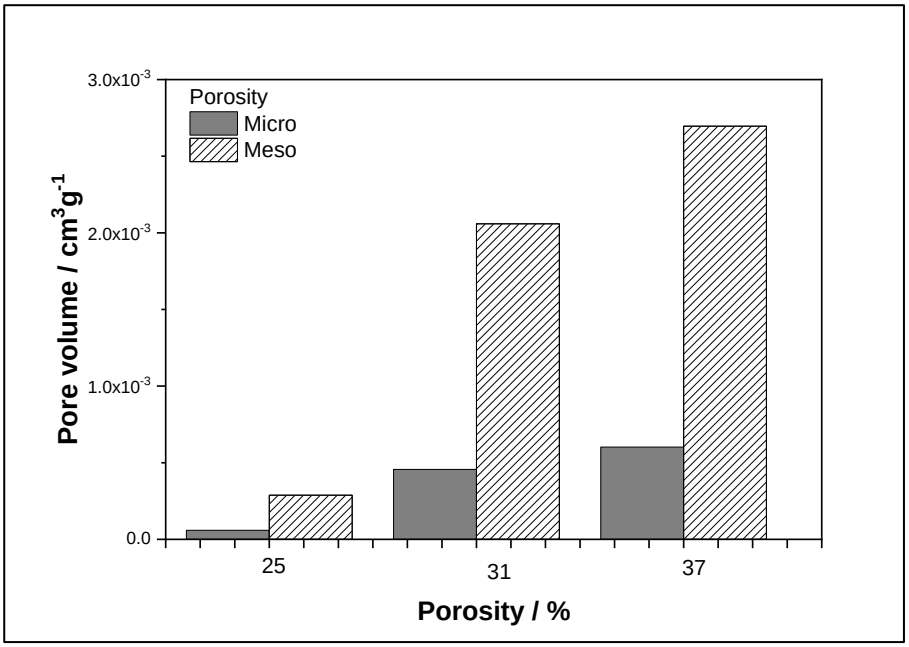

Figure 8. Estimation of the pore volume of Ti-20Nb-11Ta-16Fe-1Mn obtained from adsorption/desorption isotherm results.

Figure 9 (a) shows FE-SEM/EDS of Ti-20Nb-11Ta-16Fe-1Mn, which revealed a homogeneous distribution of the alloying elements. Additionally, in Figure 9 (b) the XRD pattern revealed that the alloy was mainly composed by β-phase plus TiNb and TiTa, TiFe (cubic, Fd3m), TiO_2 (cubic, Fm3m), $Nb_{0.3}Ti_{0.7}$ (orthorhombic, Cmcm), and FeNb. As is known, the β-phase decreases the elastic modulus and increases the ductility of the Ti-based alloy without compromising its mechanical strength [10]. On the other hand, intermetallic compounds such as $Nb_{0.3}Ti_{0.7}$ would provide hardness to the metal matrix and consequently reinforce the alloy because they are harder than the typical Ti alloys and compounds.

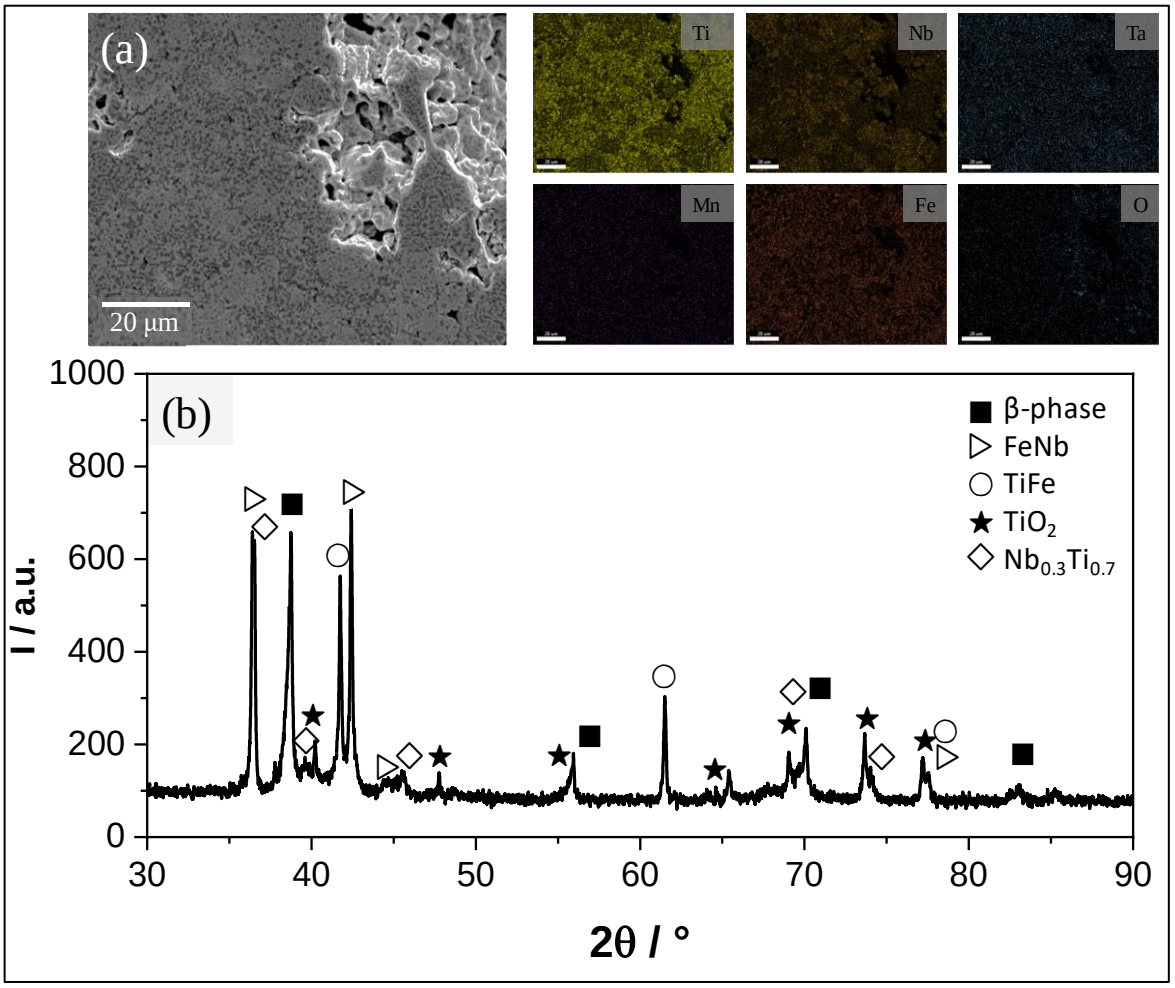

Figure 9. (a) EDS Mapping and (b) XRD pattern of a sample of Ti-20Nb-11Ta-16Fe-1Mn after sintering with 30% porosity

6.2 Mechanical properties

Elastic modulus and Poisson ratio (ν) were estimated by ultrasound technique. Table 3 summarizes the values of samples with different porosity percentages prior to exposure with their corresponding error%, showing that the bulk samples of Ti-20Nb-11Ta-16Fe-1Mn at%

exhibit high values between 50 and 84 GPa, in contrast with the porous samples, which varied between 5 and 12 GPa. However, the value for the bulk samples was even lower than the commercial alloy, which is around 110 GPa [10]. Furthermore, the E as well as the density of the alloy decrease as a function of porosity percentage. However, the ν remains relatively constant close to 0.36, and similar values were reported for bulk samples of CP-Ti and Ti-6Al-4V alloy [70,71]. Ti-6Al-4V samples show a quick drop of E with porosity addition, reaching 2.3 GPa for the piece with 42% porosity, and its density decreased by half compared to the bulk material. Therefore, the new alloy could have a better combination of mechanical properties compared to commercial alloy (Ti-6Al-4V).

Table 3. Elastic modulus properties obtained by ultrasound technique prior to exposure

Sample	ρ / kg·m^{-3}	E / GPa	error / %	ν / -	error /%
Ti-20Nb-11Ta-16Fe-1Mn at%					
0% AM	6905.6	84.3	48.4	0.34	29.5
0% SPS	6531.4	48.8	39.3	0.43	7.7
25% PM	5088.0	11.7	24.7	0.32	18.3
31% PM	4779.2	8.8	24.6	0.38	9.6
33% PM	4805.8	7.8	25.3	0.38	10.2
37% PM	4143.9	4.6	21.7	0.35	11.7
Ti-6Al-4V wt%					
0% wrought*	4349.4	114.0	19.3	0.32	14.4
31%	3029.2	5.9	15.2	0.31	12.3
42%	2428.1	2.3	13.1	0.3	11.5

*commercial alloy

Figure 10 shows the evolution of the coefficient of friction (COF) for a Ti-20Nb-11Ta-16Fe-1Mn at% sample with different porosity up to 100,000 cycles, where each curve is an independent measurement. For the bulk sample, the COF begins at 0.2, which increases to close to 0.7 before the 20000 cycles (Figure 10 (a)). For sample with 30% porosity the COF is around 0.2 with a more extended initial state than the bulk sample to then achieves a value like the bulk sample (Figure 10 (b)). However, the sample with 60% porosity maintains a low COF value near 0.2 during whole cycles performed (Figure 10 (c)).

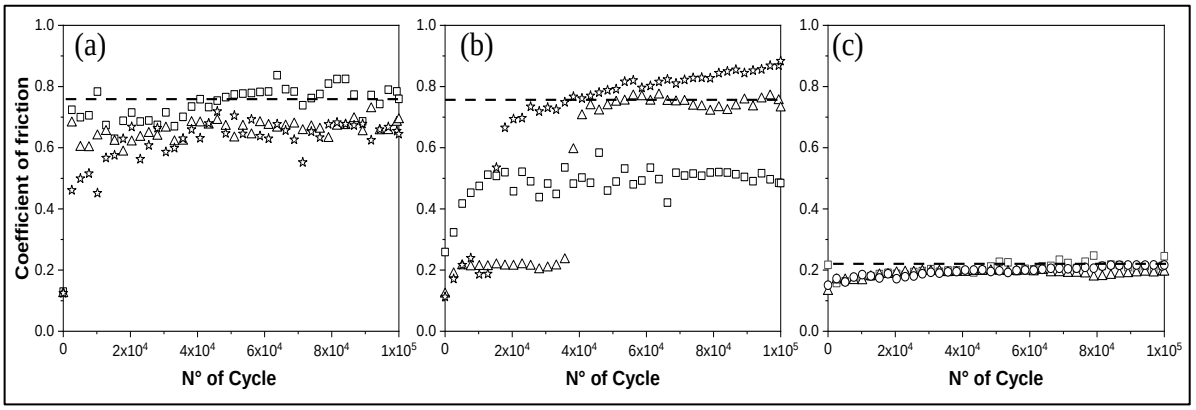

Figure 10. Evolution of COF during test: (a) bulk sample, (b) 30% porosity and (c) 60% porosity samples.

Figure 11 shows the wear results that are represented by the wear volume and the scratch profile as a function of porosity. As can be observed, the bulk sample has a higher wear volume than both porous samples, and the streak was deeper in the bulk sample than in the porous samples after 100,000 cycles.

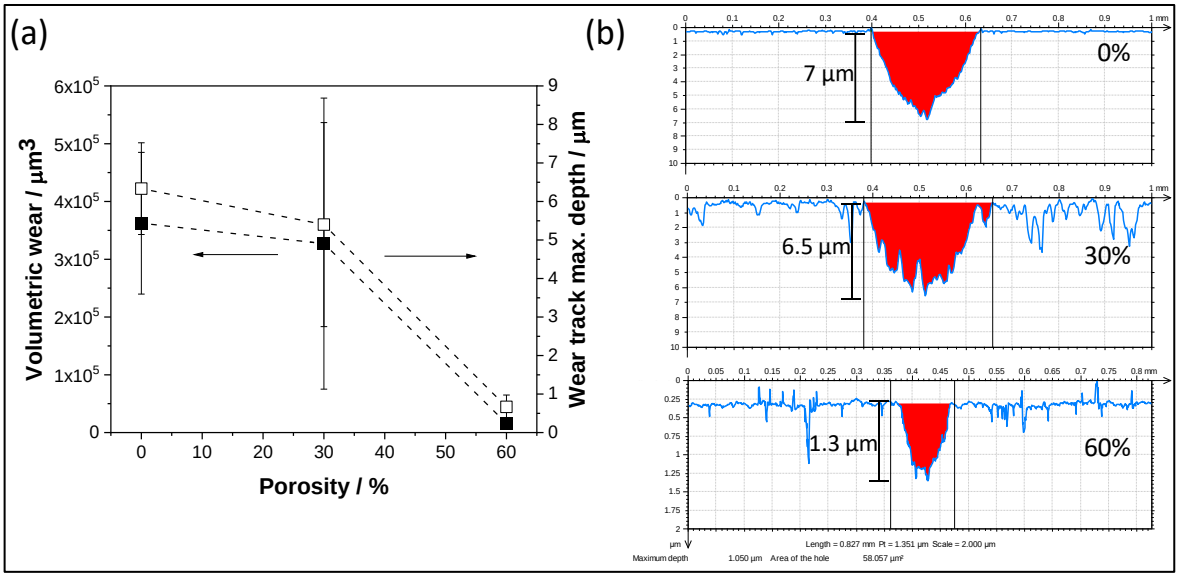

Figure 11. Images of wear tracks on the surface obtained by (a) optical profilometer for samples with different porosity and (b) the scratch profile after being tested.

6.3 Electrochemical characterization

Figure 12 (a) shows the LSV after 24 h of exposure of bulk Ti-6Al-4V and Ti-20Nb-11Ta-16Fe-1Mn at.% to a simulated body fluid (SBF) at 37 °C. The commercial alloy exhibits a higher current density compared with the novel alloy Ti-20Nb-11Ta-16Fe-1Mn at.%, and a shift of the potential (E_{OC}) toward the positive values. Ti-Al-V also shows a stable passivity

current, in contrast with the novel alloy, which did not achieve its passivity current in the potential range and sweep rate used. Figure 12 (b) shows the LSV response of Ti-30Nb-13Ta-2Mn at.% from 2 to 504 h (21 days) of samples with 40%. As is observed, the E_{OC} was shifted towards more negative values as time passed, and a slight increase in current is also evident through the exposure. Additionally, a wide range of passivity is observed in all samples near 250 mV. It should be mentioned that the porous sample demonstrated a lower current than bulk samples. However, the first was not normalized by the area.

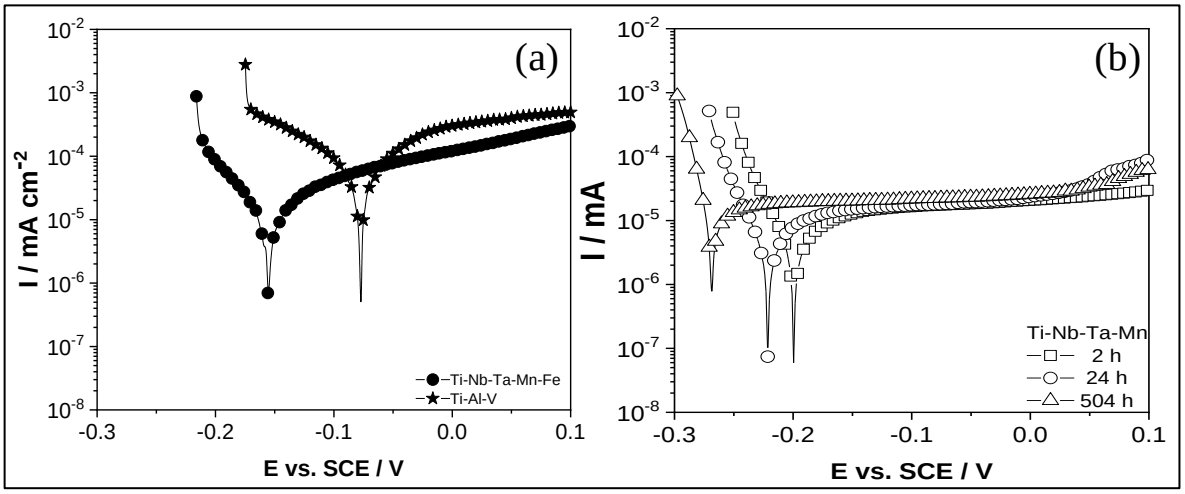

Figure 12. LSV of (a) bulk Ti-6Al-4V and Ti-20Nb-11Ta-16Fe-1Mn at.% samples after 24 h of exposure and (b) Ti-30Nb-13Ta-2Mn at.% samples with 40% porosity as a function of time exposed to SBF at 37°C.

Figure 13 shows the impedance response of Ti-30Nb-13Ta-2Mn at.% with 40% porosity between 1 and 21 days of exposure. As can be seen, the total impedance decreases slightly during the exposure, revealing three loops, one at the high frequency (HF), one at medium frequency (MF) and another at low frequency (LF).

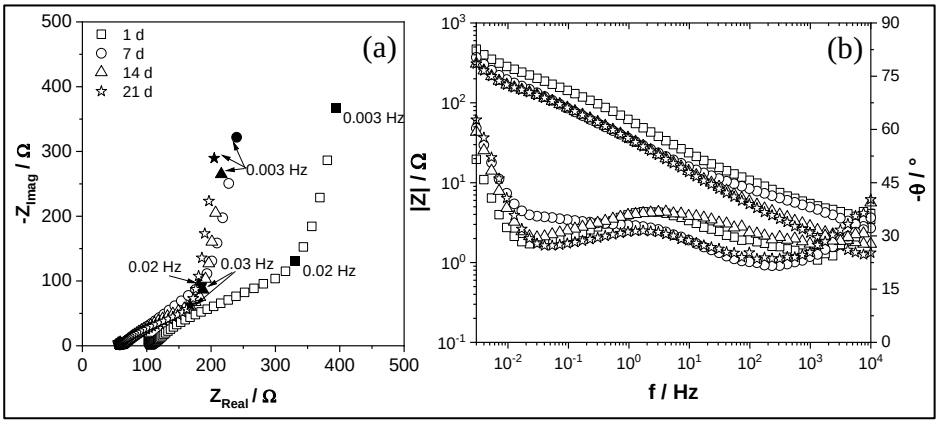

Figure 13. EIS of Ti-30Nb-13Ta-2Mn at.% alloys with 40% porosity as a function of exposure time. (a) Nyquist diagrams and (b) Bode plots.

On the other hand, Figure 14 shows the (a) Nyquist diagrams and (b) Bode plots of Ti-20Nb-11Ta-16Fe-1Mn at.% alloy with different porosity percentages after 42 days of exposure. In this case, the impedance response also exhibited three loops throughout the whole frequency range. Figure 14 (b) shows clearly the variation of phase angles, which were close to 30° and 70° at the HF and LF domains, which are lower than the 45° and 90° described by De Levie [62] for a completely cylindrical pore. This can also be attributed to the difference pore sizes, since it would be in the presence of material with hierarchical porosity, more similar to a material with a fractal structure, as was described by Itagaki et al. [60].

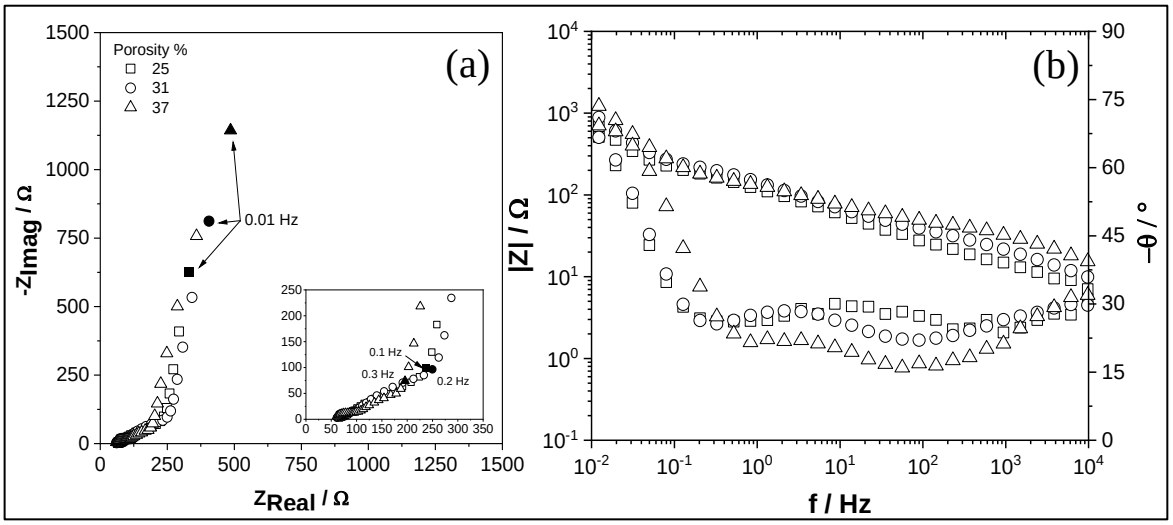

Figure 14. EIS collected as a function of porosity percentage after 42 days of exposure (a) Nyquist and (b) Bode plots.

7 PRINCIPAL CONCLUSION

The electrochemical results of porous Ti-based alloys showed higher variability in their response to shorter exposure times, which was attributed to the oxide passive film formation after being immersed in SBF at 37 °C. It was evidenced through EIS and potentiodynamic curves measurements, which contributed to monitoring the evolution of the oxide, as can be seen in articles I and II. The quantification of pore volumen evolution was carried out by adsorption/desorption isotherms, as well as FE-SEM images, which correspond to the specific goals one and two. Despite the sign of changes in the overall porosity of samples, no ions release was observed by ICP-AES, reveling that the oxide formed on the entire surface remained passive even after 91 days of exposure. This could be attributed to the fact that the oxides formed were composed of titanium mainly, as was published in I and III articles.

Regarding the mechanical properties, low elastic modulus values were reached, close to those of the human bone, between 3 and 11 GPa for porous samples obtained by powder metallurgy between 25% and 60% porosity. This showed that it is possible to achieve low stiffness even in the Ti-6Al-4V alloy, which is mainly composed of phase with HCP structure, by adding porosity. The E values were reported in produced articles I, III, and IV. Tribological properties also showed positive behavior concerning wear and friction in porous samples. This occurred since the pores worked as receptors and accumulators of wear residue, which avoided the three-body wear mechanisms, maintaining a low friction coefficient and a wear rate with a higher porosity within 100,000 test cycles. These results were better than those formulated in the hypothesis, since the higher the porosity of the Titanium alloys, the better their tribological performance, and therefore they would be candidates for bone joints, as was published in article IV achieving the specific objective three.

In summary, it can be concluded that porous Ti-based alloy electrochemically proved not to be influenced by porosity percentage, since the passivity was maintained even in confined spaces (such as smaller pores), and thus an increase in the corrosion rate did not occur. On the other hand, the porosity enhanced the biomechanical compatibility through elastic modulus, reaching values similar to the bone. Similar behavior occurred with the tribological properties, which saw an enhancing of COF and wear rate in the presence of porous samples due to the wear debris accumulated inside them, avoiding the three-body mechanism. Therefore the proposed hypothesis was accomplished partially.

Finally, the objectives of this thesis were fulfilled as evidenced by the published work allowing to verify the hypothesis and conclude that porous Ti-based alloys are concluded to be suitable candidates for bone replacement.

8 OUTLOOK

The present thesis was developed within the framework of novel Titanium alloy for orthopedic use. Therefore, deterioration analysis was performed after exposure to a simulated body fluid. Two methods of characterization were mainly carried out: mechanical and electrochemical characterization. Both showed that porous Ti-based materials had properties that met the orthopedic requirements, among them an elastic modulus close to the bone, high resistance to corrosion, and good tribological properties. However, some of them have to be explored in-depth, for instance:

- Control of the size and shape distribution for porous samples that can influence the mechanical and electrochemical properties. Currently, a viable way to produce this type of material is through additive manufacturing.
- Iron addition to the porous Ti-based alloy in different percentages, in order to explore their influence on mechanical and corrosion performance as a bone replacement candidate.
- Mathematical simulation of the electrochemical impedance response of porous material since currently researches have been done in the context of porous materials for use in batteries, but none has considered the randomness in a metal structure in order to predict the behavior of the material for biomedical applications.

  Analysis of the oxide formed on the metal surface, to understand its influence on osseointegration. As is well known, some oxides would promote osseointegration. However, there are not enough studies related to oxide features, which promote bone adhesion.

Some of these future prospects are expected to be developed during the postdoctoral program abroad.

9 ARTICLE I

Effect of porosity on mechanical and electrochemical properties of Ti-6Al-4V alloy

Carola Martínez[1,2], **Carolina Guerra[3*],** Daniela Silva[2], Mariela Cubillos[1], Francisco Briones[4], Lisa Muñoz[5], M. A. Páez[5], Claudio Aguilar[2] and Mamié Sancy[1,3,6*]

[1] Escuela de Construcción Civil, Facultad de Ingeniería, Pontificia Universidad Católica de Chile, Av. Vicuña Mackenna 4860, Macul, Santiago, Chile.
[2] Departamento de Ingeniería Metalúrgica y de Materiales, Universidad Técnica Federico Santa María, Av. España 1680, Valparaíso, Chile.
[3] Departamento de Ingeniería Mecánica y Metalúrgica, Escuela de Ingeniería, Pontificia Universidad Católica de Chile, Av. Vicuña Mackenna 4860, Macul, Santiago, Chile.
[4] Escuela de Ingeniería Mecánica, Facultad de Ingeniería, Pontificia Universidad Católica de Valparaíso, Los Carrera 01567, Casilla de Correo 4059, Quilpué, Chile.
[5] Departamento de Química de Materiales, Facultad de Química y Biología, Universidad de Santiago, Av. Libertador Bernardo O´Higgins 3363, Santiago, Chile.
[6] Centro de Investigación en Nanotecnología y Materiales Avanzados "CIEN-UC", Pontificia Universidad Católica de Chile, Av. Vicuña Mackenna 4860, Macul, Santiago, Chile.

[*]Corresponding author: **Carolina Guerra** and Mamié Sancy
e-mail: caguerra2@uc.cl, mamiesancy@gmail.com

Key-words: Ti-6Al-4V, porosity, mechanical, electrochemical, impedance, joint implants.

9.1 Introduction

The biomedical implant industry has experienced a rapid growth due to the fact that the average life expectancy of human beings has increased significantly [72], resulting in a greater prevalence of degenerative diseases, such as arthritis, arthrosis, and osteoporosis amongst others, which may lead to pain or loss of biological function [73]. In particular, primary total hip arthroplasty (THA) and primary total knee arthroplasties (TKA) have risen significantly [74]. Indeed, THA is expected to increase from 208.600 (in 2005) to 572,000 by 2030, and TKA from 450.000 to 3.48 million procedures [10].

Typical materials used for joint implants include 316L stainless steels, Co-Cr alloys, Co-Cr-Mo alloys [75], which have an elastic modulus (E) close to 200 GPa, being higher than the human bone that ranges from 2 to 30 GPa [76–78]. This difference can cause a stress shielding effect, requiring possibly a revision surgery. Nonetheless, these materials are still utilized for this application. In this context, a scientific and technological challenge has been imposed to improve their mechanical and surface properties in order to be more biocompatible and to maintain their bio-functionality [79]. On the other hand, commercially pure-Ti (CP-Ti) and Ti-based alloys have been also used for joint implants due to their relative low density, high specific strength, an E around to 110 GPa, favorable biocompatibility and corrosion resistance [10,79,80]. Specifically CP-Ti has shown high

resistance to corrosion in different biological media. The addition of alloying elements improve the mechanical properties, although perhaps can promote a local dissolution and lead to an undesirable toxic effect on the human body [80]. For the first generation of Ti-based alloys, Al, V, Ni and Co have been used as alloying elements [81–84], and the Ti-6Al-4V alloy is one of the most commonly used materials with joint implants due to its favorable mechanical properties and corrosion resistance [85]. Meanwhile, a second generation of alloys have been developed with elements that are non-toxic to the human body, such as Nb, Ta, Mo, Zr [35,79,80].

It has been reported that the mechanical properties of Ti-based alloys may be influenced by the microstructure, which are given by the fabrication method and/or heat treatment [86,87]. The microstructure of Ti-based alloys can be composed by a Ti-α phase corresponding to a hexagonal close packed phase (HCP), Ti-β phase to a body centered cubic phase (BCC), and Ti-α´phase to a martensitic microstructure [10]. Thus, mechanical properties such as the yield strength values (σ_y) can vary from 896 to 1034 MPa, the ultimate tensile strength (UTS) varying between 965 and 1103 MPa, and the E being between 86 to 116 GPa [35,88]. Furthermore, the E could can be also decrease with addition of porosity, that may occur via different fabrication methods [18]. In this context, Zhang et al. [89] investigated a Ti-Nb-Zr alloy with a 66 to 80 % porosity that was fabricated through 3D printing. The authors estimated that the E was around 3 GPa and with ultimate compressive strengths (UCS) close to 70 MPa. Weißmann et al [90] studied a porous Ti-6Al-4V alloy with a porosity between 40 and 60% that was obtained by selective laser melting (SLM), estimated with E values between 3 to 26 GPa and UCS between 103 to 403 MPa.

From a mechanical point of view, the addition of porosity can favor the biocompatibility. However, the corrosion resistance could also be affected [91,92]. For CP-Ti and Ti-based alloys an increase of corrosion current density (i_{corr}) and a shift of corrosion potential (E_{corr}) towards more negative values have been observed with the increase of porosity [59]. Alves et al. [28] estimated this effect for porous CP-Ti after being exposed to 0.9 wt. % NaCl at 37 ºC. Li et al. [93] also observed this response for porous Ti-Cu obtained by a powder metallury technique. Sri Maha Vishnu et al. [94] estimated an increase of i_{corr} for porous Ti-Nb also obtained by a powder metallury technique.

This work is focused on the Ti-6Al–4V alloy, the most commonly used in medical practice for this application, in order to better understand the influence of the porosity on the mechanical and electrochemical behavior. Thus, this alloy was studied as bulk (0% porosity) as well as a porous electrode (30-40% porosity) after being exposed to a simulated bio fluid solution at 37 ºC that was employed to mimic the conditions of the human body.

9.2 Experimental

9.2.1 Samples

The Ti-6Al-4V alloy utilized during the experiment consisted of commercial bulk and porous samples that were obtained via powder metallurgy (PM) technique using commercial Ti-6Al-4V powders (99.92%, 45-106 μm, AP&C), and mixed with $(NH_4)_2CO_3$ (99%, Loba Chemie) as a space-holder. The powders mix were pressed uniaxially at 400 MPa in a cylinder die with an inner diameter of 8 mm. After, the following heat treatment was applied, i) 1.5 h at 180 °C to remove the space-holder and ii) 3 h at 1250 °C for consolidation under Ar-atmosphere [63] to prevent the oxidation of samples. Thus, three samples were utilized in this work, a bulk sample with 0 % of porosity and porous samples with 31% and 42 % of porosity.

9.2.2 Surface cleaning treatment

Ti-6Al-4V samples were mechanically polished with 600–1200 grade SiC paper (Bulk samples) and 600–4000 grade SiC paper (porous samples). The polishing of the bulk samples was carried out in two stages using: i) polycrystalline diamond suspension with a size of 9, 6 and 2 μm and ii) colloidal silica suspension with a size of 0.05 μm as the abrasive agent for the final finish. After which, the samples were cleaned with alcohol in a sonicator bath for 10 min.

9.2.3 Structural and mechanical analysis

Samples after the final polishing treatment were etched with Kroll's reagent corresponding to (in mL): 3 HF (40%. Vimaroni), 6 HNO_3 (70%. Vimaroni) and 100 distilled H_2O, for 20 s to observe the revealed microstructure of each material using an optical microscope Olympus model BX60M. Additionally, the Vickers micro-hardness was determined according to the ASTM E-92 standard [95], and evaluated with a constant load of 200 Kg applied for 10 s ($HV_{0.2}$) at room temperature. The indentations measured were done using a Zwick/Roell indentec model ZHV.

9.2.4 Porosity analysis

The apparent porosity of the porous Ti-6Al-4V electrodes were estimated by the Archimedes method, according to the Standard Test ASTM C373-88 [64]. The specific surface area and pore size distribution were determined by the Brunauer–Emmett–Teller (BET) analysis from the N_2 adsorption/desorption isotherms (Micromeritics, 3 flex Physisorption).

9.2.5 Exposure

Samples were exposed to a simulated body fluid solution (SBF) consisting of (in g/L): 9.00 NaCl (99.79%, Winkler), 0.43 KCl (Q.A, Winkler), 0.20 $NaHCO_3$ (Q.A, Winkler), and 0.24 $CaCl_2$ (Q.A, Winkler), all in an incubator at 37±1 ^oC during 1 month [74]. A portion of the SBF was changed for a fresh solution every 7 days.

9.2.6 Surface analysis

The morphology and chemical composition of the bulk and porous electrodes were evaluated by a field emission-scanning electron microscope (FE-SEM, QUANTA FEG 250) equipped with an energy dispersive spectrometer (EDS). X-ray powder diffraction (XRD) patterns were obtained using a multipurpose powder diffractometer (STOE STADI MP), equipped with Cu $K_{\alpha 1}$-radiation source (λ =1.54056 Å, curved Germanium (111) monochromator of the Johann-type) and a microstrip detector (DECTRIS MYTHEN 1K). The crystallographic phases were identified by the search-match algorithm comparing the combined peaks with patterns provided by the X'pert HighScore database (Version: 2.1b (2.1.2)). The surface composition of the samples were also studied with X-ray photoelectron spectroscopy (XPS). XPS spectra were collected using an analysis chamber Phoibos 150 with a 1D-DLD detector monochromatic x-ray source: Focus 500 with an XR50M with Ag/Al Anode. X-ray photoelectron spectroscopy data were analyzed with software CasaXPS Version 2.3.22. The energy scale of the spectra was calibrated in relation to the binding energy (BE) of advantageous hydrocarbons (C-C/C-H) in the C1s signal at 285.4 eV. Curve fitting and decomposition were performed after removing the Shirley-type background. A mixed Gauss–Lorentz shape was used for the different components.

9.2.7 Electrochemical characterization

The working electrode consisted of bulk and porous Ti-6A-4V samples that were mounted into a rotating disc electrode kit (OrigaTrod, Origalys) with an exposed geometric area of 0.28 cm^2. Electrochemical measurements were carried out using a three-electrode cell with a platinum rod as the counter electrode and a saturated calomel electrode (SCE) as the reference electrode. A thermostatic water bath was kept at 37±1 °C and the rotation rate of the working electrode was set to 150 rpm. Electrochemical measurements were performed using a potentiostat/galvanostat (VSP, Biologic). Open circuit potential curves (OCP) were registered after a steady-state was reached. Then electrochemical impedance spectroscopy (EIS) data were collected over a frequency ranging from 25 kHz to 3 mHz with eight points per decade and using a 10 mV of peak-to-peak sinusoidal voltage at E = OCP. The impedance results were fitted by using a lab-developed software called SIMAD (LISE UPR 15 CNRS, France) using the CPE behavior for bulk electrodes, and the De Levie model for porous electrodes. Notice that the frequency range used for this adjusting was determined

by the Kramers-Kronig relation until the lowest χ^2 value was reached. After collecting impedance measurements at OCP condition, linear sweet voltammetry was carried out using a 0.1 mV s^{-1} as sweep rate and an overpotential range of ±10 mV from OCP.

9.3 Results and Discussion

9.3.1 Porosity effect on morphology and mechanical properties

BET analysis revealed that for porous samples the area related to micro- and meso-porosity were close to 0.15 m^2 g^{-1} and 0.20 m^2 g^{-1} prior to exposure, which increased to 0.21 m^2 g^{-1} and 0.24 m^2 g^{-1} after exposure. BET analysis showed that the primary porosity was macro-porosity [96], and the Archimedes method revealed that the porosity was close to 31% and 42%.

Figure 1 shows SEM micrographs that reveal the morphology of the bulk and porous samples. Both images show regions of different contrast, associated with differences in Vanadium content, as revealed by the EDS analyzes performed on the porous samples, and whose results are shown in Table S1 (see additional information). The lighter areas correspond to a Vanadium content markedly greater than that obtained in the dark areas, which appears more related to the general composition of the alloy. It is possible that the darkest areas of the porous sample in Fig.1a are associated with the bottom part of the pores formed by the spacer material used during its manufacture.

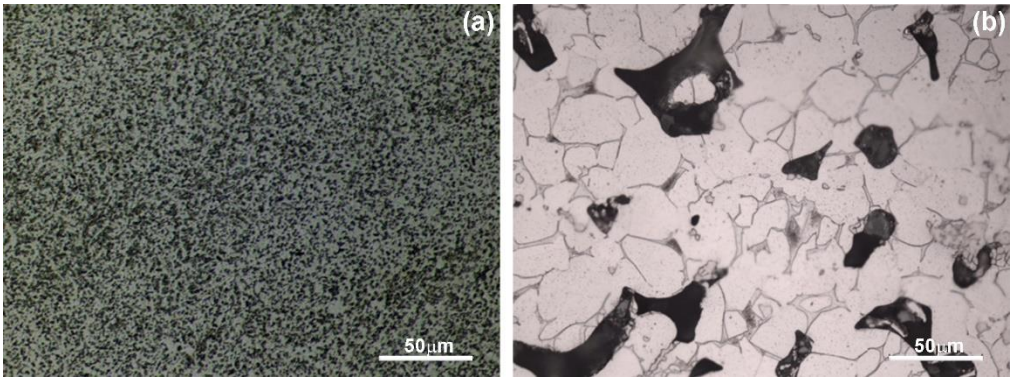

Figure 1: Micrographs of Ti-6Al-4V prior exposure. (a) Bulk and (b) porous samples with 31 % of porosity.

Ultrasonic measurements made on bulk and porous alloys show that the porosity, and the degree of this, significantly decreases Young's modulus (E). Thus, the value of E for the material bulk, which is 110 GPa, decreases to 5.6 ± 0.7 GPa and 3.2 ± 0.8 GPa, for samples with 31% and 42% porosity, respectively. The decrease in E results from the presence of two types of porosities, the first produced by the removal of space holder particles and the second, produced by sintering the pores. On the other hand, there was a slight increase in the average microhardness, from 488 ± 16 HV0.2 for the bulk sample, to 535 ± 55 HV0.2 for

the porous sample. However, this difference can be neglected due to the large standard deviation calculated from the measurements made with the porous sample, which is possibly associated with the presence of pores below the surface. Therefore, the introduction of porosity is an opportunity to decrease the elastic modulus, which makes it very close to the corresponding human trabecular bone [43,44]. Moreover, the effective surface area increases, which would favor osseointegration.

9.3.2 Microstructural properties of Ti-6Al-4V

Figure 2 shows the XRD patterns of bulk and porous Ti-6Al-4V samples. Prior to exposure, both samples revealed the presence of peaks associated with Ti-α and Ti-β phases, that it is in accordance with the phase diagram for a Ti-6Al with 4% V [97] and darker and lighter regions analyzed by SEM-EDS.

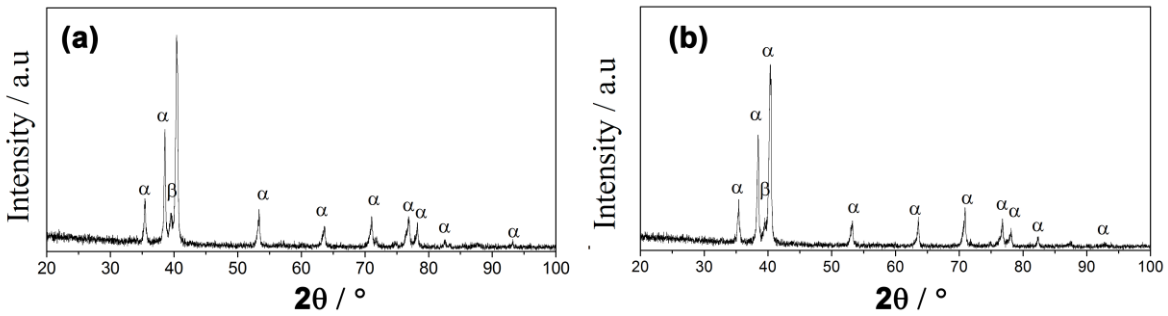

Figure 2: XRD patterns of Ti-6Al-4V electrodes prior and after exposure. (a) Bulk and (b) porous samples.

9.3.3 Surface analysis post-exposure to the electrolyte

Figure 3 shows the XPS spectra of the bulk sample, before and after 21 days of exposure. Figure 3(a) shows the complete spectra of the bulk sample, revealing the presence of Ti, Al, V and O, as well as the presence of other species from the contact of the sample with the electrolyte (Ca, N and C). It should also be noted that different C signals were detected, such as C-N (~286.0 eV), which may be associated with ammonium carbonate (NH_4CO_3) used as a space support holder; Si - C (~283.9 eV), which can be attributed to the SiC paper used during the polishing treatment; C-O (~287.7 eV) and C-OH (~288.9 eV) that can be related to the presence of the NH_4CO_3 and/or $NaHCO_3$ species present in the electrolyte [46].

Figure 3(b) shows that before exposure to the electrolyte, it is possible to identify two vanadium signals: at ~511.8 eV for V and at ~515.9 eV for V_2O_3. These signals were slightly shifted after exposure, close to ~513.1 eV and that of V_2O_3 to ~516.7 eV [47]. In addition, Figure 3(b) shows the high resolution deconvolution of Ti2p signals related to the following species: Ti^{3+} (~461.5 eV) and Ti^{4+} (~459.1 and ~464.7 eV) before exposure, and Ti^{2+} (~453.9

eV), Ti^{3+} (~454.6 and ~459.1 eV) and Ti^{4+} (~459.3 and ~464.7 eV) after electrolyte exposure. It is important to consider that changes in the chemical composition of the oxide film could cause changes in the conditions of the passive film [48]. On the other hand, Figure 3(b) shows the deconvolved Al2p signal before and after exposure to electrolyte, which can be associated with Al_2O_3 (~ 74.7 and ~ 74.9 eV) before electrolyte exposure, and with Al metallic (~72.09 and ~73.1 eV), Al_2O_3 (~ 74.4 and ~ 74.9 eV) and $Al(OH)_3$ (~75.6 and ~76.1 eV) after electrolyte exposure. This indicates that Al2O3 hydrates during its contact with the electrolyte to form $Al(OH)_3$ [48]. Figure 3(b) also shows the O signals, prior to exposure, the deconvolution of the O1 spectrum produced the presence of four sub-peaks: Al_2O (~529.2 eV), Ti-O link (~530.6 eV), OH- and OH- link of water (~531.1 eV and 532.7 eV). After exposure, the O1 spectrum shows four sub-peaks again: the Ti-O link (~530.6 eV) can be associated with TiO_2; The OH- (~531.2 eV) groups can be attributed to the OH bond of the hydroxyl group, the Ca-O signal at ~532.4 eV may be related to the calcium oxide formed due to the presence of calcium and OH- water in the electrolyte (~533.7 eV) [49]. It should be mentioned that the XPS spectra of the surface oxides in the bulk sample after 21 exposure, and in the porous sample after 14 days of exposure, reveal a similar chemical composition (see Figure S2 in the supplementary material).

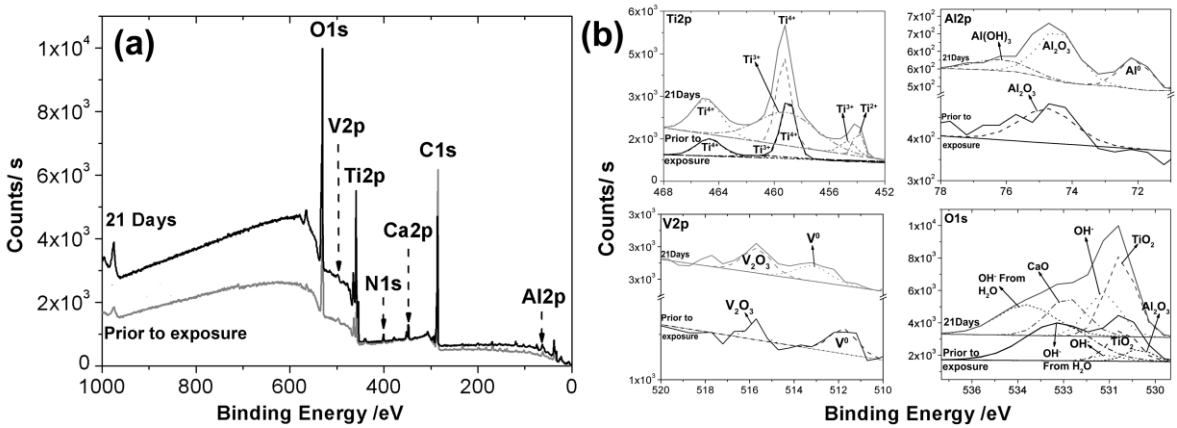

Figure 3: XPS spectra of bulk Ti-6Al-4V sample after 21 days of exposure. (a) Complete scan and (b) high resolution of alloying elements and oxygen.

9.3.4 Electrochemical characterization

9.3.4.1 Bulk electrode

Figure 4(a) shows the Nyquist plots of bulk sample after exposure, revealing a capacitive behavior characterized by two time-constants in the high frequency (HF) and low frequency (LF) ranges. The impedance modulus was not influenced significantly during exposure, but only slightly in the LF range with values being close to $2x10^4\,\Omega{\cdot}cm^2$ [59,98]. Tamilselvi et al also reported two time-constants for this alloy after exposure to similar conditions, which were attributed to the formation of a bi-layer, an inner barrier layer followed by a porous

outer layer [98]. Alves et al [59] studied commercial pure Ti (CP-Ti) as well as Ti-6Al-4V exposed to SBF and observed a one-time constant at 25 °C, but two time-constants at 37 °C. Nabavi and Aliofkhazraei [99] also studied this impedance response for a Ti-6Al-4V in similar conditions that was also ascribed to the oxide formed by the outer porous and inner dense barrier layers.

In order to better understand the impedance response in the HF domain, the impedance data was corrected by the electrolyte resistance (R_e), as shown in Figure 4(b,c) [100,101]. Notice the R_e was not influenced significantly over time, as can be observed in Table 1. However, a strong effect was evidenced on the corrected Bode plots in the HF range, increasing the phase values from 57° to 72°, revealing a constant phase element (CPE) behavior [100]. This phenomenon may arise from a frequency dispersion due to the electrode geometry effect that favor a non-uniform primary current distribution at the electrode periphery [102–104], and/or a dispersion of time constants along the electrode surface or in the direction normal to the electrode surface [105].

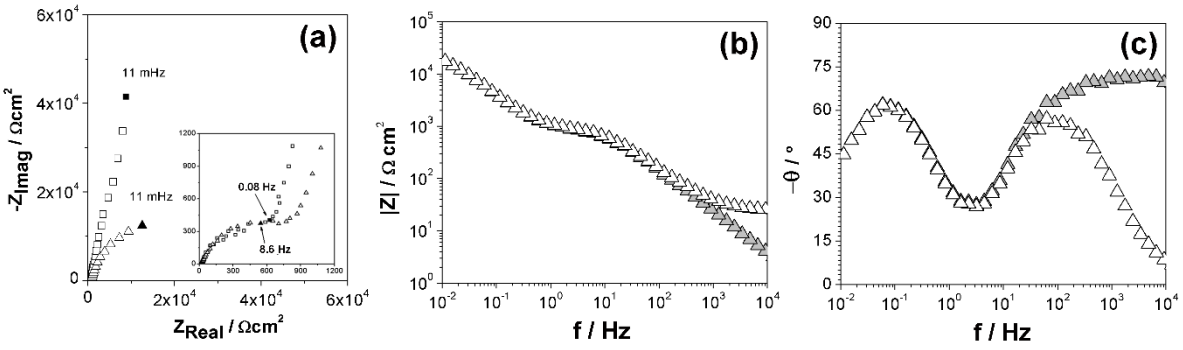

Figure 4: Impedance response of bulk Ti-6Al-4V electrode after exposure to sterile SBF at 37 °C. (a) Nyquist plots (☐) 1 day and (△) 21 days. (b,c) (△) non- and (▲) corrected-Bode plots by the electrolyte resistance after 21 days.

Thus, CPE parameters were estimated in the LF and HF domains by a graphical method as well as a fitting (see Table 1). The alpha (α) parameter was around 0.81 and 0.87 in LF and HF ranges which did not show a clear trend during exposure. As was mentioned above, the time-constants might be associated with the bi-layered oxide film. Nevertheless, the time-constant could also be attributed to the oxygen (O_2) reduction reaction that occurs at the electrolyte/oxide interface and represented by a double layer capacitance (C_{dl}) in parallel to the charge transfer resistance (R_{ct}), and to the oxide layer formed on the surface. In fact, the C_{dl} in the LF range was estimated by the Brug formula [106], resulting close to 148 μF/cm^2 after exposure, values that are larger to the typical C_{dl} values [100], as shown Table 1. This could be influenced by the roughness of surface and/or the electric properties of the oxide film. Advancing the analysis, impedance data was also collected by applying anodic overpotentials, as shown in Figure S3 of the supplementary material. These impedance results, in the entire frequency range, showed a response similar to those obtained at the open

circuit potential, revealing that at the OCP, and at low anodic overpotentials, the impedance corresponds mainly to the response of the Ti-Al-V substrate, covered with oxide.
It should be mentioned that when the frequency tends towards infinity, the impedance corresponds to that of a pure capacitor, therefore, the capacity of the oxide layer can be estimated from the complex capacitance graphs (also called Cole plots), as proposed by Benoit et al. [60].

$$C_{Imag} = \frac{-Z_{Real}}{2\pi f*(|Z|)^2} \quad (1)$$

$$C_{Real} = \frac{Z_{Imag}}{2\pi f*(|Z|)^2} \quad (2)$$

In this case, Z_{Real} is the real part of the impedance, and |Z| the modulus of the impedance that may be corrected by the electrolyte resistance (R_e). Figure 5(a) shows the Cole-Cole plots that reveal a straight line crossing the origin for the frequency range corresponding to CPE behavior (see the insert). the capacitance of the oxide layer was obtained by extrapolation of the high-frequency data, giving a value close to 3.2 µF/cm^2. This value is relatively stable over time, as shown in Figure 5(b).

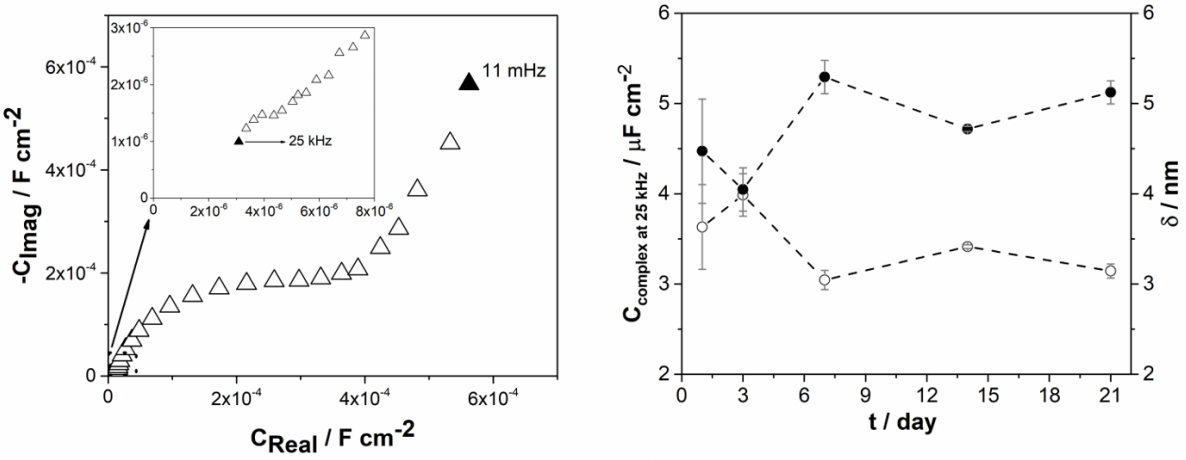

Figure 5: (a) Cole-Cole plot of bulk Ti-6Al-4V electrode after 21 days of exposure to sterile SBF at 37 °C and (b) summary of complex capacitance at 25 kHz and thickness estimation as a function time of exposure. (○) Complex capacitance at 25 kHz and (●) thickness of oxide layer.

Additionally, the thickness was estimated from the complex capacitance in this frequency range, utilizing the Eq. (1), as was proposed by Hirschorn et al. [107]:

$$C_{HF} = \frac{\varepsilon_0 \cdot \varepsilon}{\delta} \quad (3)$$

where C_{HF} represents the complex capacitance in the HF range, δ corresponds to the thickness of the oxide in cm, ε_0 is the vacuum permittivity equal to 8.85x10^{-14} F·cm^{-1}, and ε represents the dielectric constant. For Ti-based alloys this has been a controversial issue

throughout literature. An example being Hilario et al. [108] reporting that ε can vary between 18.2 to 173, whereas Barranco V. et al.[109] and Navarro Laboulais et al. [110] used as a ε value equal to 45. In this study an ε equal to 18.2 was used, showing a slight increase in the thickness of the oxide layer with exposure time, from 4.2 to 5 nm, as shown in Figure 5(b). These results are in agreement with the values obtained when CP-Ti is oxidized at room temperature (δ = 2.2 nm) [111] and after anodizing at 5 V (δ = 8 nm) [112].
Since the corrected Bode plots revealed a clear plateau in HF range (see Figure 4) that can correspond to a CPE behavior, the power-law model was used for describing the impedance contribution of the oxide film, given by the following formula Eq. (4).

$$Z_{oxide} = g\frac{\delta\rho_{\delta}^{(1-a)}}{\left(\rho_0^{-1}+j\omega\varepsilon\varepsilon_0\right)^{(a)}} \quad (4)$$

where g is an expression evaluated numerically

$$g = 1 + 2.88(1-\alpha)^{2.375} \quad (5)$$

α is the parameter CPE. ρ_0 and ρ_δ are the boundary values of resistivity at the metal/oxide interface and at the oxide/electrolyte interface. In Eq. 4, the parameters δ and ρ_δ appear as a product that was obtained by regression, which allow estimate a solution for the resistivity profile given in Eq. (7). A normalized resistivity ρ/ρ_δ versus the dimensionless distance γ/δ is presented in Figure S4 in the supplementary material. The normalized resistivity showed a decrease towards the oxide/electrolyte interface, which falls more drastically after 1 day than 21 days of exposure. This behavior can be related to the chemical composition observed by the XPS spectra.

$$\frac{\rho}{\rho_\delta} = \left(\frac{\rho_\delta}{\rho_0} + \left(1-\frac{\rho_\delta}{\rho_0}\right)\xi\right)^{-1} \quad (6)$$

Table 1: Impedance fit parameters of bulk Ti-6Al-4V electrodes after exposure to SBF.

t days	R_e Ω·cm^2	$-\alpha_{HF}$	$-\alpha_{LF}$	Q_{LF}x10^{-5} Fcm^{-2}s$^{-(1-\alpha)}$	C_{dl} µFcm^{-2}
1	22.3 ± 0.2	0.74 ± 0.02	0.86 ± 0.01	32.6 ± 9.0	161 ± 43
3	17.8 ± 3.3	0.73 ± 0.01	0.88 ± 0.01	26.0 ± 8.7	115 ± 47
7	20.2 ± 11.1	0.69 ± 0.06	0.86 ± 0.03	26.5 ± 5.1	134 ± 51
14	24.6 ± 3.4	0.71 ± 0.05	0.84 ± 0.003	34.1 ± 4.4	153 ± 1
21	23.9 ± 11.0	0.75 ± 0.02	0.92 ± 0.12	20.9 ± 6.3	167 ± 50

Note: For fitting, $\chi 2$ values varied from 3.3; 1.2; 2.2, 2.8 and 2.0 as a function of time.

Figure 6(a) shows an equivalent circuit proposed for a bulk Ti-6Al-4V after exposure to SBF. In this case, the time-constant in the HF domain is related to the Ti-oxide film, and the time-constant in the LF range is associated with the O_2 reduction reaction at the interface.

Additionally, Figure 6(b) shows the fitting results obtained by the adjustment to the experimental data, with a $\chi^2 = 1.5$. It should be noted that the accuracy of the fitting is comparable to the graphic method, as shown in Table 1.

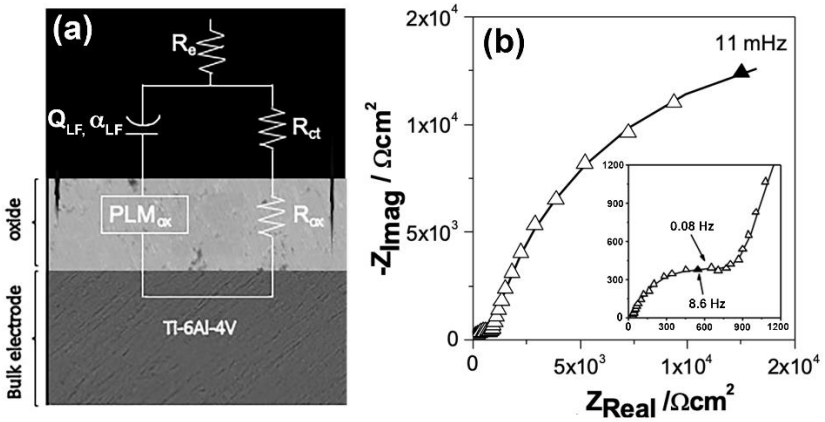

Figure 6: (a) A representative equivalent circuit of bulk Ti-6Al-4V. (b) a comparison of (△) experimental and (-) fitting adjusting of impedance data of after 21 days of exposure to sterile SBF at 37 °C.

9.3.4.2 Porous electrodes

Figure 7 shows the impedance response for a sample with a 31% of porosity as a function of exposure time, and where the effective area was not considered. It should be noted that the kind of response was completely different to that observed by the bulk electrode, but both were not influenced significantly during SBF exposure. In general, the impedance response showed a minor influence in the LF range for larger porosity, as can be seen in Figure S5 of the supplemental material. Figure 7(a) reveals a straight line in the HF and LF ranges with slopes lower than 45º and 90º against a real axis (see the insert). The slope deviation in the LF range is also clearly observed in the Bode plots (see Figure 7(b)), reaching a phase angle close to 80°. However, the deviation in the HF range is uniquely evidenced when the R_e correction was done, as shown in Figure 7(c), showing a phase angle value around 30°. This kind of response has been related to a typical porous electrode well described by the De Levie theory [63,108].

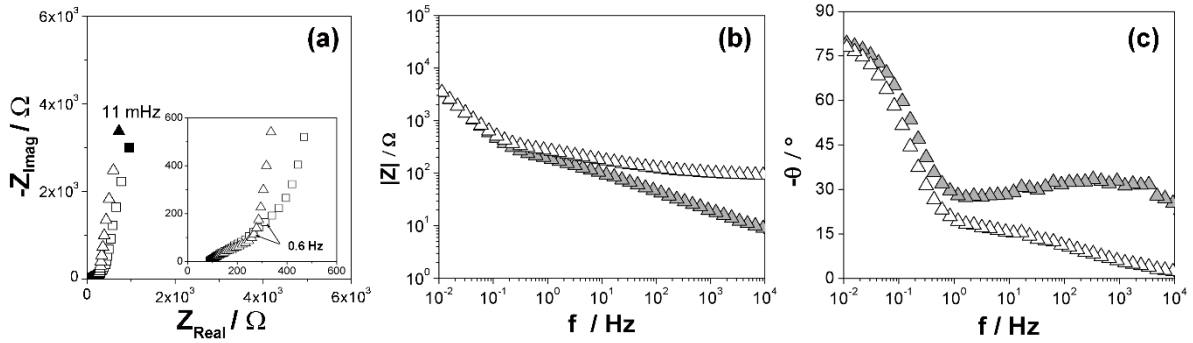

Figure 7: Impedance response of Ti-6Al-4V with 31% porosity after exposure to sterile SBF at 37 °C. (a) Nyquist diagram after (□) 1 day and (△) 21 days and (b,c) Bode plots (△) non- and (▲) corrected- by the electrolyte resistance after 21 days.

A transmission line model has been proposed to interpret the physical and chemical phenomena by De Levie [62,100]. In this case, a parallel schema of identical cylindrical pores was considered with a straight line of 45º in the HF range and 90º in the LF range. However, the impedance data of porous Ti-6Al-4V samples revealed a deviation from those values, with phase angle values (-θ) close to 80º in the LF domain for both samples, and around 32º in HF range for 31% porosity, that decreased from 33º to 26º in HF domain for 42% porosity, as can be observed in Table 2. This deviation was previously described by Song, who proposed a pore size and shape distribution effect in the transmission line model. Moreover, Itagaki [60] suggested that the impedance response of porous electrodes can be dominated by the macro-pore, meso-pore, and micro-pore, as well as by the interfacial impedance. In the present case, the lower θ values in the HF region for porous samples with 42% porosity could indicate a major penetration of the electrolyte, even reaching the meso- and micro-pores.

Table 2: Impedance parameters of porous Ti-6Al-4V estimated from graphical method after being exposed to SBF at 37 ºC

t (days)	Porosity (%)	R_{pore} (Ω)	$\|\theta_{HF}\|$ (º)	$\|\theta_{LF}\|$ (º)	$-\alpha_{LF}$	$Q_{LF} x10^{-3}$ ($F\ s^{-(1-\alpha)}$)	$Q_{LF,\ porous}/Q_{LF,\ bulk}$ (cm^2)
1	31	223 ± 2	29 ± 0.4	80 ± 0.7	0.90 ± 0.01	3.6 ± 0.1	11.2 ± 3.5
3		175 ± 10	30 ± 4.3	80 ± 4.2	0.91 ± 0.02	3.5 ± 0.1	13.4 ± 5.0
7		174 ± 43	26 ± 0.6	79 ± 4.8	0.90 ± 0.03	3.9 ± 0.8	15.0 ± 6.1
14		184 ± 11	30 ± 5.2	82 ± 1.7	0.91 ± 0.01	3.3 ± 0.04	9.7 ± 1.3
21		186 ± 25	27 ± 0.7	81 ± 2.3	0.91 ± 0.02	3.4 ± 0.2	8.3 ± 1.6
1	42	183 ± 32	33 ± 1.3	80 ± 2.3	0.88 ± 0.02	2.9 ± 0.1	8.9 ± 2.8
3		136 ± 22	30 ± 2.4	81 ± 0.6	0.90 ± 0.01	2.6 ± 0.1	10.3 ± 3.7
7		142 ± 5	32 ± 1.8	80 ± 0.4	0.90 ± 0.00	2.9 ± 0.2	10.9 ± 2.9
14		135 ± 21	32 ± 0.1	81 ± 1.0	0.89 ± 0.04	2.8 ± 0.3	8.4 ± 1.9
21		134 ± 14	26	81	0.87 ± 0.04	2.9 ± 0.5	7.1 ± 2.2

Table 2 shows the $Q_{LF,porous}/Q_{LF,bulk}$ ratio that was utilized for estimating the electro-active area for porous samples, determining that for porous samples the electro-active surface area was close to 10 cm^2 for sample with 31% porosity, which decreased slightly for sample with 42% porosity. This indicate that the porosity has not an influence on the electrochemical reaction mechanism, only resulting from a size-effect. In this work, the transmission line model proposed by De Levie was used, despite pore size and shape distribution influencing the impedance response. Table 2 also shows the contribution of the pore resistance (R_{pore}) that was estimated from the extrapolation of the slope in the LF range to the real axis [63], and was not influenced by exposure time. Thus, an equivalent circuit is proposed for a porous

Ti-6Al-4V after exposure to SBF based on the transmission line model previously discussed [62,100], as shown in Figure 8(a). Moreover, Figure 8(b) shows the fitting obtained by the adjustment to the experimental data. It should be mentioned that in this circumstance, the average χ^2 was close to 5.3, which can be associated with the shape and size distribution of pores.

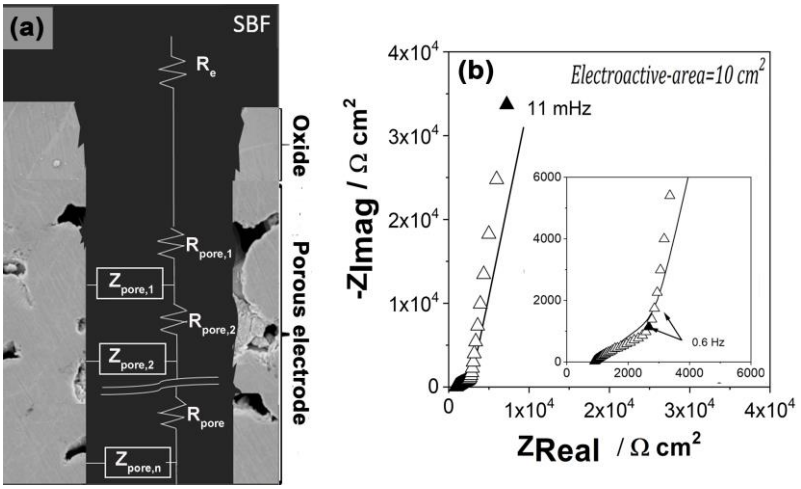

Figure 8: (a) Equivalent circuit proposed for a porous Ti-6Al-4V electrode after exposure to SBF at 37 °C and (b) Nyquist plot for a sample with 31% porosity after 7 days exposure, (△) experimental data and (-) fitting data.

Figure 9 shows the linear sweep voltammetry after 1 day of exposure and the variation of the anodic current (I_a) as a function of the exposure time for bulk and porous material. It should be mentioned that both samples revealed that the E_{corr} was shifted towards more positive values and I_a was not modified during the exposure, as shown Figure S5 in material supplementary. Figure 9(a) shows that the passive range was close to 100 mV for the bulk sample, which increased around 300 mV for the porous electrode. Additionally, the passivity was broken down near 35 mV vs. SCE for bulk sample and close to 200 mV vs. SCE for porous electrode. An electro-active area close to 10 cm^2 for porous sample was also estimated from the linear sweep voltammetry by using the $I_{a,porous}$ /$I_{a,bulk}$ at $E=E_{corr}+8mV$ ratio after 1 day that is in accordance with the impedance analysis. Those results suggest the formation of a passive oxide film that can provide protection against a corrosion process [28,59,92] even for the porous samples.

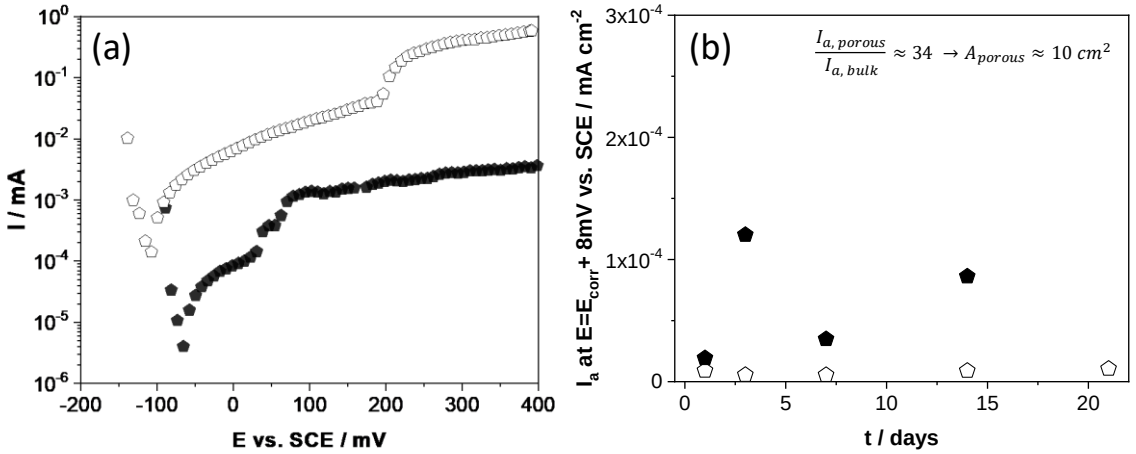

Figure 9: (a) Linear sweep voltammetry and (b) variation of I_a at $E=E_{ocp}+8mV$ as a function of exposure time in SBF at 37 °C. (⬟) Bulk and (⬠) 31% of porosity electrodes.

9.4 Conclusions

The addition of porosity to the Ti-6Al-4V alloy decreased the elastic modulus, from 110 GPa for a bulk sample to around 5 GPa for a porous sample. Before exposure, XRD patterns revealed the presence of α-phase and β-phase. After exposure, XPS spectra showed that an oxide layer was formed on surface that was composed mainly by TiO, Ti_2O_3, TiO_2, $Al(OH)_3$ and CaO. The addition of porosity to the changed the electrochemical response of the Ti-6Al-4V alloy. Impedance analysis of bulk sample revealed a CPE behavior in the HF domain, which is associated with the presence of a passive oxide film and also, in LF range, related to the oxygen reduction reaction, taking place at the electrolyte/oxide interface. For porous electrodes, the impedance response showed a De Levie behavior that was not significantly influenced by exposure time and added porosity. The electroactive area of porous samples was estimated close to 10 cm^2 by impedance analysis and linear sweep voltammetry, the slight variation of the anodic current was attributed to the modification of area.

10 ARTICLE II

Evolution of oxide film on the internal porosity of Ti-30Nb-13Ta-2Mn alloy foam

Carolina Guerra[1], Mamié Sancy[2,3*], Magdalena Walczak[1,3], Daniela Silva[4], Carola Martínez[5], Bernard Tribollet[6] and Claudio Aguilar[4]

[1]*Departamento de Ingeniería Mecánica y Metalúrgica, Escuela de Ingeniería, Pontificia Universidad Católica de Chile, Av. Vicuña Mackenna 4860, Macul, Santiago, Chile.*
[2]*Escuela de Construcción Civil, Facultad de Ingeniería, Pontificia Universidad Católica de Chile, Av. Vicuña Mackenna 4860, Macul, Santiago, Chile.*
[3]*Centro de Investigación en Nanotecnología y Materiales Avanzados "CIEN-UC", Pontificia Universidad Católica de Chile, Av. Vicuña Mackenna 4860, Macul, Santiago, Chile*
[4]*Departamento de Ingeniería Metalúrgica y de Materiales, Universidad Técnica Federico Santa María, Av. España 1680, Valparaíso, Chile.*
[5] *Instituto de Química, Pontificia Universidad Católica de Valparaíso, Av. Universidad 330, Valparaíso, Chile.*
[6]*LISE, Sorbonne Universités, UPMC Univ Paris 06, CNRS, 4 place Jussieu, F-75005 Paris, France*

*Corresponding author. Email: mamiesancy@uc.cl (Mamié Sancy)

10.1 Introduction

The interests of biomedical industry in light-alloys foams has been motivated by their potential application in the ever greater prevalence of degenerative diseases, such as arthritis, arthrosis, and osteoporosis among others. The parts of human body that are mostly affected are the hip, knee, shoulder, and ankle [10], requiring replacement of the degeneratied part in order to avoid pain and restore the biological function. The number of the related surgical intervetions is at rise with the estimation of 174% growth for the primary total hip arthroplasty (THA), from 208,600 in 2005 to 572,000 by 2030, and staggering 673% for the primary total knee arthroplasty (TKA), from 450,000 in 2005 to 3.48 million procedures by 2030 [75]. At the same time, the increasing life expectancy requires that the impants may be implemented with minimum risk and maintain their reliability over a longer time. In particular, the physical and mechanical properties of the implant would ideally be in agreement with the native bone tissue, not only in terms of mechanical strength or flexibility but also biocompatibility, allowing for osteointegration and sustained bio-functionality [79]. Further, it should be considered that any product of materials degradation may cause inflammation, allergic reactions possibly compromising the normal function of the implant or even be released to the blood flow [80].

The alloys that are conventionally used for joint implants include 316L stainless steels (316LSS), Co-Cr alloys and Ti-based alloys. Although the first two options have been preferred for their widely tested biocompatibility (and also the economic aspect), their mechanical properties are far from compatible with elastic modulus of about 200 GPa as

compared with 2 to 30 GPa of the hard bone tissue. Whereas, Ti-based alloys have elastic modulus closer to that of human bone and additionally display low density, high specific strength, biocompatibility and good corrosion resistance [10,79,115]. The first generation of Ti-alloys featured Al, V, Ni and Co as alloying elements that improved significantly the mechanical properties but produced toxic effect upon the event of (tribo)corrosion. Second generation alloys have been developed non-toxic alloying elements, such as Nb, Mo, and/or Zr [79–84].

Independent of the type alloy, a further opportunity for improving the short- and long-term bio-functional performance of an implant is by introduction of porosity. The presence of pores reduces the elastic modulus and, in case of interconnected porosity, allows for a stable long-term fixation by increasing the effective surface area at which osteointegration can take place. Pore size, pore shape and porosity are crucial to the process of osteogenesis [11,84]. However, the increase of the porosity in the metallic alloy implies the increase of the active surface area to be in effective contact with the surrounding body fluid, which in case of release and build-up of corrosion product increases the risk of aseptic failure as compared with a bulk alloy. Although total joint replacements for osteoarthritis and rheumatoid arthritis are effective interventions, release of corrosion products and wear debris remain the major factor limiting their time of service with signs and symptoms often not being clinically apparent until late stages of tissue destruction.

Up to now, electrochemical studies on porous Ti-based alloys focused on identifying the relation between porosity and corrosion performance. Alves et al. [28] observed that a variety of Ti-alloy concepts fabricated by the powder metallurgy technique increase in corrosion current (I_{corr}) is associated with higher porosity. Fangxia Xie et al. [26,116] studied Ti-xMo porous alloys (x taking values of 4, 6, or 8 wt.%) obtained by selective laser sintering observing that lower porosity correlates with a shift of corrosion potential (E_{corr}) in the anodic direction and reduction in I_{corr}, which was interpreted as increased corrosion resistance. As compared with their bulk counterparts, porous materials were shown to be generally more susceptible to electrochemical degradation, explained by a larger effective surface area determined by the size and morphology of the interconnected pores. Although bulk alloys provide better corrosion performance, the requirement of elastic modulus and technological implications of producing bulk alloys, porous alloys remain attractive for biomedical applications.

The main goal of the present work is to extend the understanding of the electrochemical behavior of a Ti-based alloy with a porosity grade close to 40% after being exposed to a simulated blood plasma fluid. Electrochemical measurements and surface analytical techniques are employed along with microstructural characterization at two levels of pore hierarchy, i.e. macro- and micropores.

10.2 Experimental

10.2.1 Samples

Alloy foams of Ti-30Nb-13Ta-2Mn at.% were fabricated through the powder metallurgy technique with space holder, using elemental powders of Ti (99.5%, <45 μm, NOAH Technologies), Nb (99.9%, <44 μm, NOAH Technologies), Ta (99.9%, <44 μm, NOAH Technologies) and Mn (99.9%, <44 μm, NOAH Technologies). The powders were mechanically alloyed in a RETSCH PM400 ball mill for the effective duration of 50 h, under protective Ar atmosphere and ball to powder weight ratio of 10:1. The alloy powder was then mixed with the desired volume fraction of $(NH_4)_2CO_3$ 50 wt.% serving as space holder. Rod test samples with 8 mm of diameter were produced by uniaxial pressing to 400 MPa and thermal treatment of the resulting cylinders for 3 h at 1250 ºC under protective Ar-atmosphere. The foam sample surfaces were mechanically polished with SiC paper ranging from 320 to 2000 grits followed by diamond paste (3 and 1 μm) on a polishing cloth to obtain a mirror surface. Later, each polished sample was rinsed with acetone and was put in an ultrasonic cleaner for 10 min. Finally, it was rinsed with distilled water and dried in air at room temperature.

10.2.2 Microstructural and mechanical characterization

The morphology of microstructure was evaluated by a field emission-scanning electron microscope (FE-SEM, QUANTA FEG 250) equipped with energy dispersive spectrometer. To determine the macroporosity of the foams the Archimedes principle was employed according to the Standard Test Method ASTM C373-88. The active area associated with the microporosity of the foams was determined using Brunauer–Emmett–Teller (BET) equation (BET, 3-FLEX). The crystalline phases were evaluated prior and after exposure to simulated body fluid (SBF) by means of X-Ray powder diffraction (XRD) using a multipurpose powder diffractometer STOE STADI MP equipped with a DECTRIS MYTHEN 1K detector and operated with Cu $K_{\alpha 1}$-source (λ = 1.54056 Å). Mechanical strength of the foams in the elastic range of deformation was estimated employing the Gibson–Ashby model [18], which relates elastic modulus (E) and relative density (ρ) of a porous metal by Eq. (1)

$$E = CE_s\left(\frac{\rho}{\rho_s}\right)^2 \quad (1)$$

where C, E_s and ρ_s are a phenomenological constant, elastic modulus of the bulk alloy (non-porous), and density of the bulk alloy, respectively.

10.2.3 Exposure and electrochemical characterization

For the electrochemical measurements, a three-electrode cell was used with a graphite rod as counter and saturated calomel electrode (SCE) as reference electrode. A rod of Ti-30Nb-

13Ta-2Mn at.% alloy foam of 0.28 cm^2 cross-sectional exposed geometrical area was used as working electrode and was mounted in a rotating disc electrode kit (OrigaTrod, Origalys). The electrolyte was a SBF corresponding to a Ringer's solution with chemical composition in g/L: 9.00 NaCl, 0.43 KCl, 0.20 $NaHCO_3$, and 0.24 $CaCl_2$. The test cell was maintained at a constant temperature of 37 ± 1 °C for the duration, which was either 2, 24, 72, 168, 336 or 504 hours. Electrochemical measurements were carried out using potentiostat/galvanostat (VSP, Biologic). Anodic and cathodic polarization curves were obtained at a scan rate of 0.1 $mV \cdot s^{-1}$ starting from E = OCP–50 mV to 0 V vs SCE. The electrochemical impedance measurements were obtained at OCP and collected over a frequency range of 3 mHz to 20 kHz with eight points per decade using 10 mV peak-to-peak sinusoidal voltage for the experiments. The impedance diagrams were analyzed by regression procedure based on a simplex strategy with a home-developed software (Simad).

10.3 Results and discussion

10.3.1 Morphological and mechanical characterization

The SEM micrographs in Figure 1 display a random structure of the alloy foam's porosity with observable distribution of pore sizes and irregular shape of individual pores. Prior exposure to SBF, the predominant pore size observed visually is below 10 μm with scare presence of larger pores (> 50 μm); however, all of the porosity seems to be interconnected. The smaller pores especially well visible in Fig. 1B are typical to sintered metal, whereas the larger pores correspond to the size of carbonate space-holder vaporized in the process (see Figure 1A and 1B). After exposure, characteristics of the porosity are visibly changed in that the smaller pores become smaller and the number of the larger pores increases. The apparent decrease of the smaller pores might be attributed to the deposition of corrosion products, which is supported by the little modification of micropores' appearance observed at longer time of exposure (see Figure 1C to 1F).

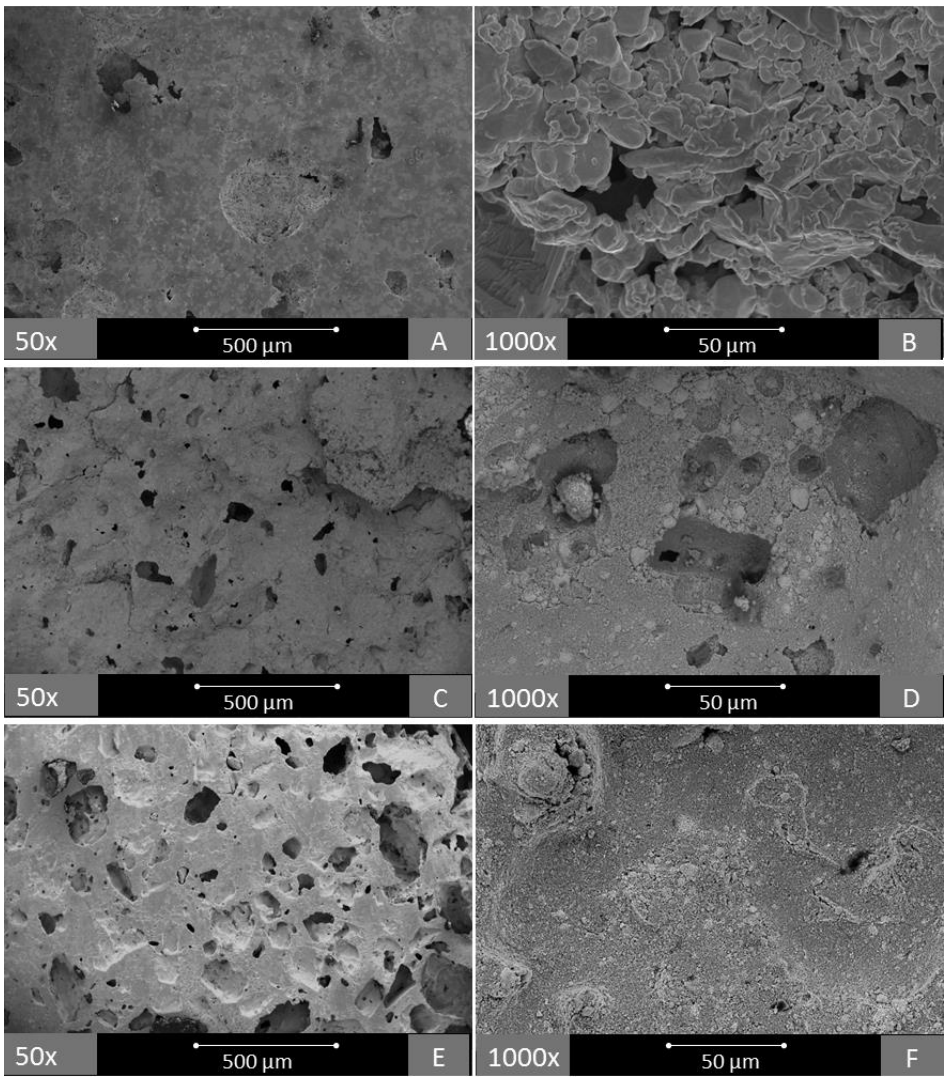

Figure 1: SEM micrographs of Ti-30Nb-13Ta-2Mn foams prior and after exposure to SBF solution at 37 ºC: (A) and (B) correspond to the initial microstructure, (C) and (D) after 72 hours of exposure, (E) and (F) after 504 hours of exposure.

The change of porosity with time of exposure is also observed quantitatively in the values obtained by the Archimedes method and shown in Fig. 2. In the initial stage of exposure (below 200 h), porosity first decreases and then increases indicating also a possible build-up of corrosion products at the interior of the pores. However, the accumulated amount is not constant in time and an occasional increase in porosity may be observed when a thinner layer is present, or a possible corrosion products dissolution reaction take place. For the longer exposure times, a slight decrease of the porosity was observed which could indicate a passive film formation on the metallic foam that is in agreement with the SEM micrographs shown in Fig. 1.

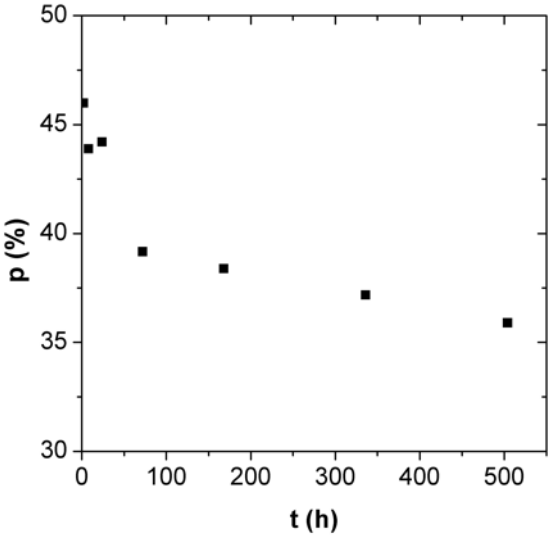

Figure 2: Porosity of Ti-30Nb-13Ta-2Mn foam in function of time of exposure to SBF solution at 37 ºC as determined by the Archimedes principle.

The active area and distribution of pore size with pore volume as estimated by the BET equation is shown in Fig. 3. The shape of the isotherm is indicative to macroporous materials [96], i.e. pore sizes > 50 nm, according to IUPAC classification. Although the method is not suitable for quantifying the larger pores observed in the SEM micrographs, it is the smaller pores that make most of the effective surface area at which electrochemical reactions take place. Considering the low adsorption behavior of the N_2 in the specific surface area of the foam, the active area determined by the BET equation was 0.57 m^2/g, which is attributed to the microporosity of the alloy. From this data, the active area participating in electrochemical reactions was estimated for the foam mass of 0.85 g considering that 3/5 of the cylinder's height was immersed. The resulting 3000 cm^2 was then used for analysis of electrochemical data. This value is assumed to be valid for all times of exposure, although minor deviation is possible due to corrosion of the metallic surface and/or formation of corrosion products. On the other hand, the existence of pores larger than 50 nm is not excluded (Fig. 3B), which is consistent with the SEM micrographs shown in Fig. 1.

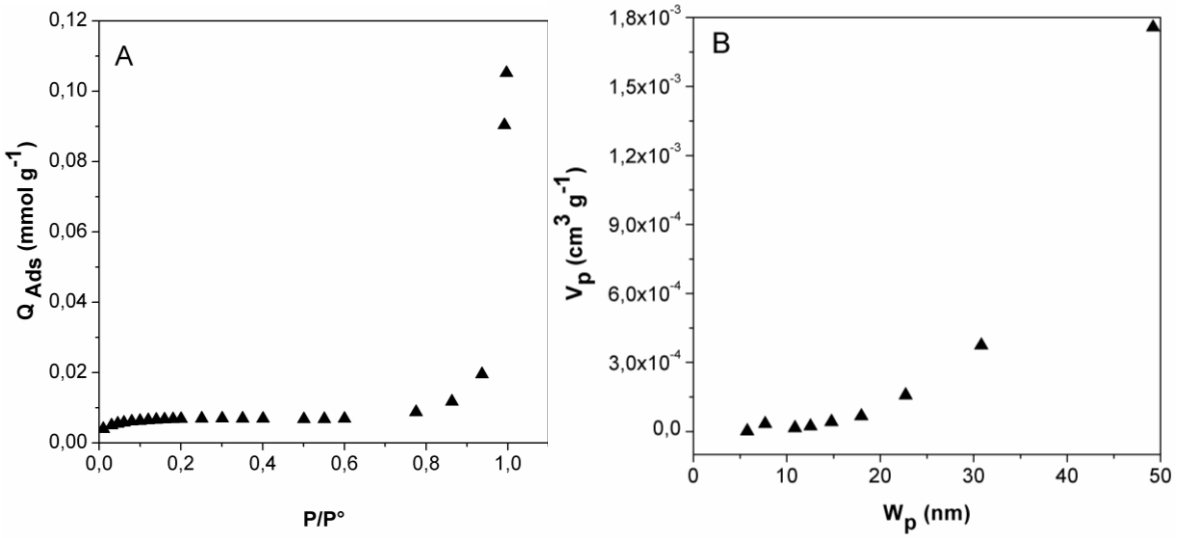

Figure 3: BET adsorption isotherm (A) and calculated pore volume (B) of Ti-30Nb-13Ta-2Mn foam after exposure to SBF for 72 hours.

Mechanical properties of the alloy foams were quantified to verify compatibility with natural bone tissue. The elastic modulus estimated by Eq. (1) for C= 1 [14,117] , E_s = 147.98 GPa and ρ_s = 12.1 g/cm^3, yielded 12.95 ± 1 GPa, which is consistent with 15 GPa reported for foams of similar composition and porosity [14], the difference being attributed to the bimodal structure specific to the material used in this study. However, the difference is irrelevant considering elastic moduli reported for femur human bone are in the range between 8.69 and 18 GPa [77], and proving the Ti-30Nb-13Ta-2Mn foam mechanically suitable for biomedical applications [118].

10.3.2 Electrochemical results

The effective surface area, i.e. the active area used for interpretation of the electrochemical data was estimated from the BET surface area as described previously. Figure 4A shows a Nyquist diagrams obtained from electrochemical impedance spectrum of the alloy foam recorded after the longest exposure time at E = OCP. The shape of the curve represent a typical impedance response of a porous electrode consisting of a metal in passive state [119]. The interfacial impedance can be associated with the impedance of an oxide layer which, in turn, can be represented approximately by a constant phase element (CPE) behavior [100]. In case of a porous electrode, the simplest approach is to employ the de Levie model, developed for the simplified geometry of cylindrical pores of equal length. The impedance of which may be described by (Eq. 2):

$$Z_{pore} = (R_0 Z_0)^{1/2} \coth\left(\ell \sqrt{\frac{R_0}{Z_0}}\right) \quad (2)$$

where R_0 (in Ω cm^{-1}) and Z_0 (in Ω cm) are the electrolyte's resistance and the interfacial impedance for a one-unit length pore, respectively [62,100,108,120]. However, by applying this formula with $Z_0 = \frac{1}{Q(j\omega)^{\alpha}}$, where Q and α are CPE parameters, it is not possible to regress with confidence over the entire frequency range. In fact, it is only suitable for describing the high frequency range (HF), in which the pore's impedance reduces to Eq. 3:

$$Z_{pore} = (R_0 Z_0)^{1/2} \quad (3)$$

A good quality of adjustment was obtained for the experimental data in the frequency range between 13 kHz and 0.13 Hz (see Fig. 4A) (and fit parameters of R_e = 56.8 Ω, Q/R_0 = 1.8 10^{-4} $F/\Omega s^{(1-\alpha)}$, α= 0.7 and χ^2= 0.7, where χ^2 is a goodness of fit test. Although the fit is of satisfying quality, it should be kept in mind that the model describes an average geometry, which is not the case of the material studied here.

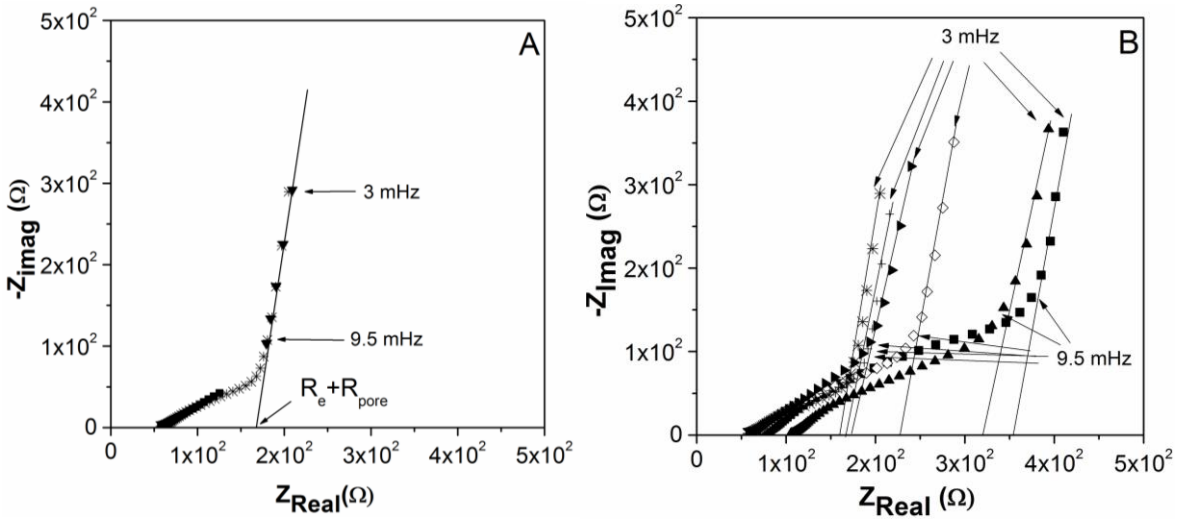

Figure 4: Nyquist diagrams of Ti-30Nb-13Ta-2Mn after being exposed in SBF solution at 37 ºC. (A) correspond after 504 hours of exposure, (■) Fitting in high frequency range, (▼) fitting in very low frequency range and (✳) experimental data. (B) correspond after (■) 2, (▲) 24, (◇) 72, (▶) 168, (✚) 336 and (✳) 504 hours of exposure time.

The complexity of the porosity and its effect on the electrochemical response can be observed on the corrected Bode plot, as shown Fig. 5, where the phase shift does not follow a monotonic tendency over the entire range of frequency. The effect of the porosity on the impedance response may be also seen in Figure. S1 of the Supplementary Material, in which a comparison of impedance response is provided between the same alloy produced with and without space holder and thus containing bimodal and microporosity, respectively. For this reason, a different model is employed for fitting the very low frequency (VLF) range. In this case the impedance is described by Eq. 4 according to Lasia [120]:

$$Z_{pore} = R_{pore} + \frac{1}{Q(j\omega)^{\alpha}} \quad (4)$$

The five points measured in VLF range (between 3 mHz and 9.5 mHz) are well fitted by the previous formula. The fitted parameters are: R_{pore} = 106.1 Ω, Q = 0.1211 F/s$^{(1-\alpha)}$, α = 0.90, χ^2= 1.09. Fit parameters obtained for the all the exposure time are summarized in Tab. 1.

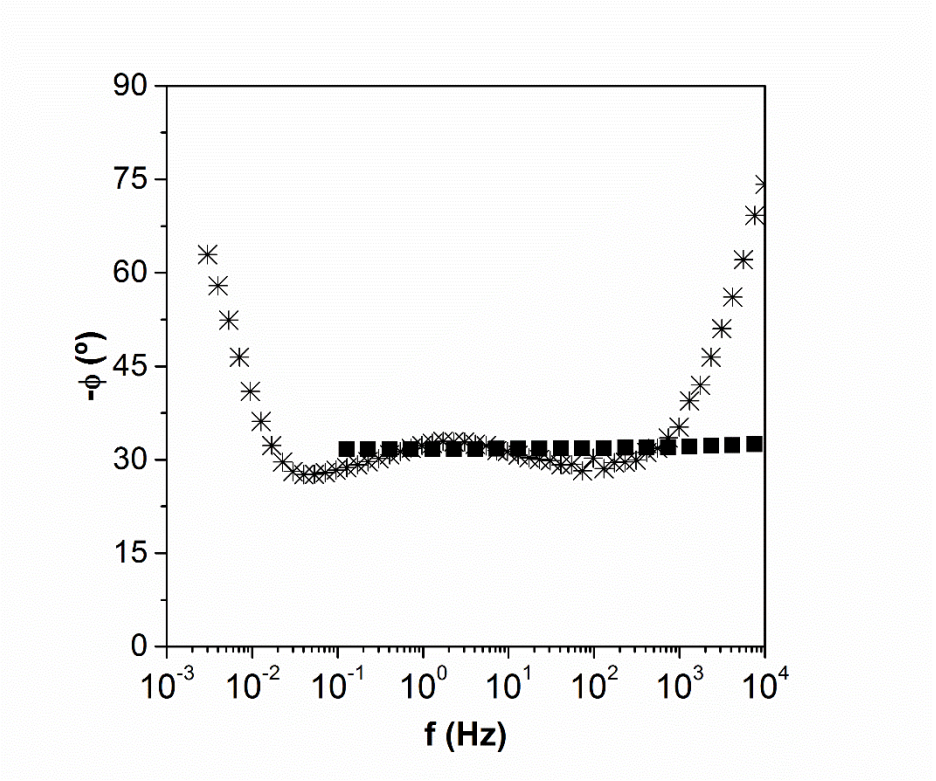

Figure 5: Phase of the corrected Bode plot of Ti-30Nb-13Ta-2Mn after 504 hours in SBF solution at 37 ºC. (■) Fitting in high frequency range and (✳) experimental data.

The fact that the α values obtained in the HF and VLF ranges are different indicates that the de Levie model is not applicable directly. This is again explained by the irregular pore geometry, which unlike the de Levie model assuming cylindrical pore shape, is too complex to be described by a simple analytical function. However, it is possible to consider that in the VLF range the impedance of the pore is the impedance of a plane electrode with a surface corresponding to the value estimated from BET surface area. Note that Q and α values were obtained as was described in [100] and the values are in agreement with a passive oxide layer with a thickness of few nanometers, as shown Table 1. Further, the resistance of pores, R_{pore}, may be expressed by:

$$R_{pore} = \frac{\rho_s \ell}{3n\pi r^2} \quad (5)$$

where *n* is the number of pores. As shown Table 1, R_{pore} decreased with time of exposure. If the pore geometry is not changing with time of exposure, then the resistivity in the pores ρ_s is also decreasing with time, which is agreement with an increase of ion concentration inside the pores due to the metal corrosion.

Table 1: Impedance fit parameters of Ti-30Nb-13Ta-2Mn alloy after exposure to SBF solution.

t / h	R_{pore} / Ω	Q / F/($cm^2 s^{1-\alpha}$)	α
2	182.0	$1.1 \cdot 10^{-5}$	0.93
24	151.5	$6.6 \cdot 10^{-6}$	0.85
72	155.0	$2.9 \cdot 10^{-5}$	0.86
168	110.5	$2.9 \cdot 10^{-5}$	0.85
336	112.0	$4.0 \cdot 10^{-5}$	0.88
504	106.1	$4.1 \cdot 10^{-5}$	0.90

On the other hand, polarization curves recorded after impedance spectroscopy (Fig. 6) corroborate the passive behavior of metal after all the times of exposure; although a shift of the corrosion potential (E_{corr}) in the cathodic direction is observed, as well as a slight increase of the anodic current density for shorter time of exposure and its decrease for the longer exposure times (see insert in Fig.6). Considering the results of EIS analysis, the modulation of anodic current indicates an ongoing competition between formation and dissolution of corrosion products along the time of exposure. It should be noted that the polarization test might have an effect on the response of the sample, as shown Figure. S2 of the Supplementary Material, which shows that the impedance response was modified that might be attributed to evolution of the corrosion process and passive oxide film. This is consistent with the low-crystallinity products and justifies the necessity of testing parallel samples rather than returning to expose samples that were already tested.

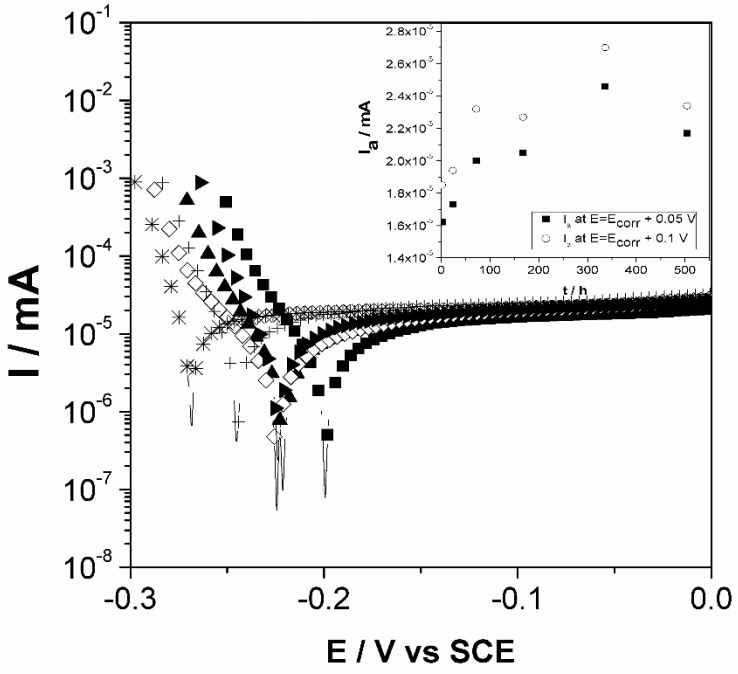

Figure 6: Polarization curves of Ti-30Nb-13Ta-2Mn as a function of exposure time in SBF solution at 37 ºC. The insert shows associated anodic corrosion currents obtained from at E = 0.05 V and E = 0.1 V vs SCE. (■) 2, (▲) 24, (◇) 72, (▶) 168, (✚) 336 and (✳) 504 hours

10.3.3 XRD analysis

Figure 7 compares XRD patterns recorded prior and after exposure to SBF. In the initial microstructure (t = 0 h) reflections of Ti-based solid solutions are identified corresponding to crystal structures typical to β-phase (Im-3m) and α-phase (P63mm/c). In addition, reflections corresponding to three distinctive titanium oxides are found: TiO, TiO_2 and Ti_2O_3, with crystal structure of Fm-3m, Pbca and R-3c, respectively. These titanium oxides are typical to high temperature exposure during the sintering process. Although sintering was conducted in Ar atmosphere, exposure of the metallic precursors to oxygen prior mechanical alloying and oxygen impurity of the protective gas is sufficient for the oxide formation due to high reactivity of Ti. There are no Nb or Ta oxides observed in the diffraction pattern indicating the formation of solid solution with the Ti matrix. After 336 h of exposure the peaks corresponding to high temperature oxide are not observed; whereas in addition to the Ti-alloy phases and additional peaks are found corresponding to titanium carbide (TiC) with cubic crystal structure cF8 (Fm3m). Further, a decrease in the intensity of the α–phase reflections is observed, which is explained by its relatively higher susceptibility to corrosion as compared with the β–phase [116] and sustained by the emergence of TiC as corrosion product due to presence of carbon in the SBF solution. Finally, there are no crystalline phases of oxides or hydroxides after exposure indicating that these corrosion products, evidenced by the electrochemical analysis, are either present in

very small fraction of volume or the remain amorphous. This last observation is consistent with the effect of polarization testing on the impedance response (Figure. S2).

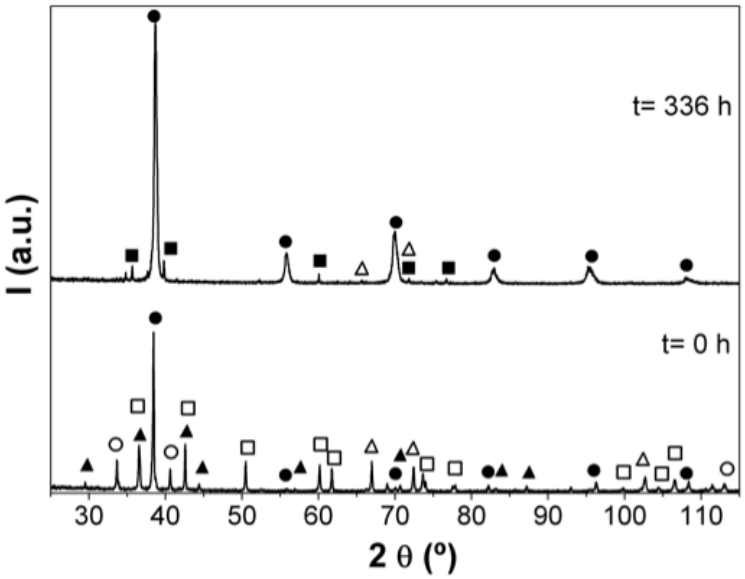

Figure 7: XRD patterns of Ti-30Nb-13Ta-2Mn prior and after 336 hours of exposure to SBF solution at 37 ºC. (●) β-solution solid; (△) α-solution solid; (■) TiC; (▲) TiO_2; (□) TiO; (○) Ti_2O_3.

10.4 Conclusion

In this study, electrochemical evaluation of porous Ti-30Nb-13Ta-2Mn in long term exposure to simulated body fluid was conducted in the context of microstructure evolution in the process. The as-sinterized random pore structure of the alloy foam, consisting of interconnected pores of irregular shape and two pore size distributions corresponding to macro- and micropores, was found to be affected distinctively at the two levels of hierarchy. Whereas the macropores increased in number and size incrementing porosity in time, the micropores were stabilized in the first hours of exposure. The electrochemical response was found to be mostly determined by the competitive processes of formation and dissolution of corrosion products at the pores' walls as demonstrated by EIS. The analysis revealed the complexity of the porous electrodes that questions the possibility of direct correlation between porosity and corrosion performance due inhomogeneity of the passive film at the inner surface that is determined not only by the pore volume.

11 ARTICLE III

Effect of added porosity on a novel porous Ti-Nb-Ta-Fe-Mn alloy exposed to simulated body fluid

Carolina Guerra[1]*, Mamié Sancy[1,2,3,]*, Magdalena Walczak[1,3], Carola Martínez[2,4], Armelle Ringuedé[5], Michel Cassir[5], Junsoo Han[5], Kevin Ogle[5], Hercílio Gomes de Melo[6], Vicente Salinas[7] and Claudio Aguilar[4]

[1]Departamento de Ingeniería Mecánica y Metalúrgica, Escuela de Ingeniería, Pontificia Universidad Católica de Chile, Av. Vicuña Mackenna 4860, Macul, Santiago, Chile
[2]Escuela de Construcción Civil, Facultad de Ingeniería, Pontificia Universidad Católica de Chile, Av. Vicuña Mackenna 4860, Macul, Santiago, Chile.
[3]Centro de Investigación en Nanotecnología y Materiales Avanzados "CIEN-UC", Pontificia Universidad Católica de Chile, Av. Vicuña Mackenna 4860, Macul, Santiago, Chile
[4]Departamento de Ingeniería Metalúrgica y de Materiales, Universidad Técnica Federico Santa María, Av. España 1680, Valparaíso, Chile.
[5]Chimie ParisTech, PSL University, CNRS, Institut de Recherche de Chimie de Paris, 75005 Paris, France
[6]Departamento de Eng. Metalúrgica e de Materiais, Escola Politécnica da Universidade de São Paulo, Av. Prof. Mello Moraes, 2463, São Paulo, Brasil.
[7]Instituto de Ciencias Químicas Aplicadas (ICQA), Facultad de Ingeniería, Universidad Autónoma de Chile, Av. Pedro de Valdivia 425, Santiago, Chile.

* Corresponding author: **Carolina Guerra** and Mamié Sancy
e-mail: caguerra2@uc.cl / mamiesancy@gmail.com
Phone number: + 562 2354 7084

Graphical abstract

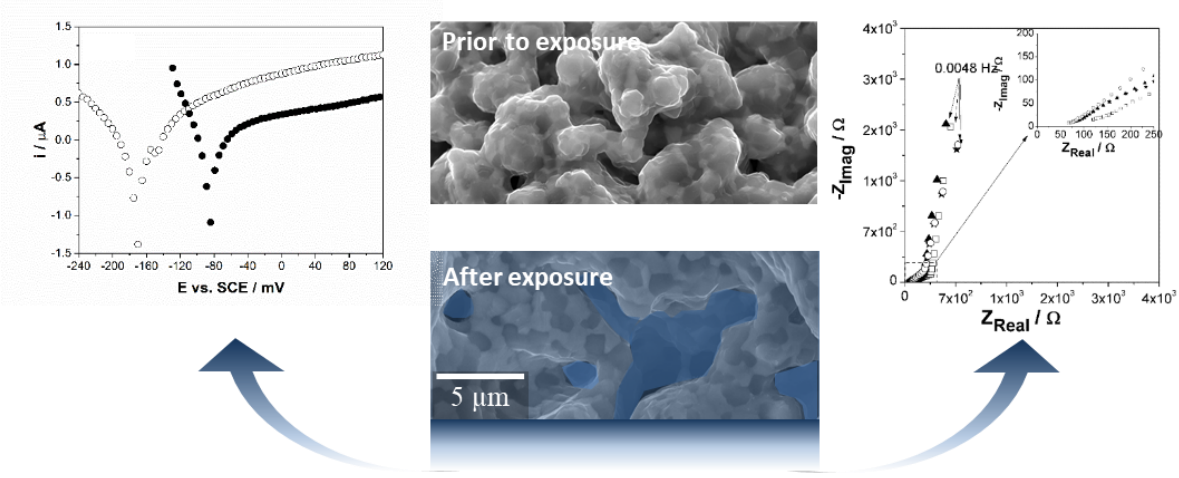

Keywords: Ti-based alloys, porous electrode, electrochemical, joint implants

11.1 Introduction

Titanium and its alloys have been proposed as suitable materials for bone replacement due to their mechanical properties, adequate biocompatibility, and high corrosion resistance [10]. However, these materials can fail indirectly through stress shielding, which has been related to aseptic loosening and the corresponding mechanical failure in approximately 12% of the cases [2]. The root cause of such a failure is the mismatch of elastic modulus of the implanted material and the native bone. In this context, porous alloys are a promising alternative for mitigating the differences in mechanical properties because adding porosity allows tuning elastic modulus towards that of bone [10,121–123]. Additionally, osseointegration might be improved due to the interconnected porosity, which provides the necessary conditions to allow bone ingrowth around the prosthesis due to cell migration and proliferation [6-7]. In this context, the oxide formation also could improve the adhesion of the cells to the titanium alloys as has been reported for TiO_2 and Ta_2O_5 [126–128].

There are different manufacturing routes used to achieve interconnected porosity, as injection molding [129], additive manufacturing [130], and the powder metallurgy technique, which allow tailoring different porosity grades and pore size distributions [85,131]. However, the introduction of porosity implies increased exposed area to the medium, which might affect corrosion resistance [132], with consequent release of metallic ions in the bloodstream.

Commercial pure Ti (CP-Ti) and Ti-based alloys are widely used for orthopedic replacement, and recently attention has turned to understand the porosity effects on their electrochemical responses when exposed to simulated body fluids (SBF). For instance, Xie et al. studied Ti-x%Mo (x=4, 6, 8 and 10 wt.%) alloys [25–27] and found a passive behavior independent from the molybdenum content. Higher corrosion resistance was associated with lower porosity grade that was related to a decrease in the volume of open and interconnected pores [25–27]. On the other hand, Alves et al. [28] reported that increased porosity slightly increased the corrosion current density (i_{corr}) and changed the corrosion potential (E_{corr}) of porous CP-Ti obtained through powder metallurgy. This was attributed to the lack of passivation inside the pores due to the difficulty of oxygen diffusion through them. Table 1 summarizes the values of i_{corr} and E_{corr} of porous CP-Ti and Ti-based alloys previously reported by different authors, where the units were adjusted in order to compare them. In addition, fabrication methods of the porous materials, such as powder metallurgy technique (PM) with and without space holder, plasma spraying (PS), selective laser sintering (SLS), spark plasma sintering (SPS), and 3D printing (3DPTM), as well as the percentage of porosity were also included. A general tendency can be observed that with increased porosity, E_{corr} may be shifted towards more negative values accompanied by an increase in i_{corr}. It should be noted that i_{corr} values reported in literature lack information on the effective area participating in the electrochemical reaction. In fact, while some works considered 1 cm^2 as area [25–27], other estimated the geometrical area [17], and rarely an attempt is made

to estimate the real area using, for instance, geometrical relations and pore numbers [28]. On the contrary, the increase of i_{corr} might also be attributed to the exposure of new areas within the porous material, which might lead to an overestimation of reported i_{corr} values [25–27,93,121]

Table 1. Summary of literature data on electrochemical response of porous Ti-based alloys relevant for biomedical applications.

Alloy / wt.%	Fabrication method	Open porosity / %	Solution at 37 °C	Electrochemical testing ∗		Ref
				E_{corr} / mV_{SCE}	I_{corr} / $\mu A \cdot cm^{-2}$	
CP-Ti	PM space holder (urea)	0.4 22 37	0.9 wt.% NaCl	20 -100	0.3 10	[28]
CP-Ti	PS	52.3	0.9 wt.% NaCl	-155.3	4.44	[133]
CP-Ti	Anodizing	Not reported	SBF	-95 174 285	1.64 0.49 3.151	[134]
Ti–4Mo	SLS	20 38 54	0.9 wt.% NaCl	-334±8 -370±12 -405±15	0.58±0.01 1.25±0.02 2.10±0.04	[25]
Ti–4Mo Ti–6Mo Ti–8Mo	SLS	55 58 65	0.9 wt.% NaCl	-400±20 -484±17 -542±25	2.10±0.08 2.76±0.04 3.25±0.14	[26]
Ti–4Mo Ti–6Mo Ti–8Mo	SLS	24 27 32	0.9 wt.% NaCl	-332±13 -293±28 -356±14	0.58±0.02 0.72±0.03 1.19±0.01	[26]
Ti–10Mo	SLS	28 42 54 63	0.9 wt.% NaCl	−353±8 −382±15 −460±10 −484±16	0.30±0.06 0.82±0.08 1.19±0.05 3.63±0.12	[27]
Ti-10Cu	PM space-holder	24.6 39.6 52.7	0.9 wt.% NaCl	-328±23 -375±28 -430±32	0.117±0.005 0.213±0.007 0.532±0.006	[93]
Ti-1Ag Ti-3Ag Ti-5Ag	PM		0.9 wt.% NaCl	-99 -141 -218	0.268 0.597 3.751	[135]

Ti-16Nb	PM Space-holder	4.23 41.97 60.83	SBF	-424 -407 -405	0.275 0.351 2.21	[136]
Ti-24Nb Ti-35Nb Ti-42Nb	PM	25.7 35.6 39.0	SBF	-411.7 -441.3 -440.2	1.09 4.09 4.56	[94]
Ti–8 graphite	PM	26.8±0.3 19.5±0.4 15.7±0.5 13.6±0.5	SB∗∗	−57±22 −17±51 −5±53 −4±22	29.3±3.1 16.6±2.5 10.0±1.9 6.7±1.7	[121]
Ti–8 graphite	PM	26.8±0.3 19.5±0.4 15.7±0.5 13.6±0.5	SBF∗∗	−76±24 −34±27 −36±7 −14±10	18.9±4.1 7.1±2.7 3.0±1.3 2.6±0.8	[121]
45Ti-10Zr-31Cu-10Pd-4Sn∗∗∗	SPS	50 60	SBF		0.02 0.07	[17]
Ti-5Ag Ti-5Ag-5Sn	3DPTM	1.50±0.73 <0.8	0.9 wt.% NaCl	−210±35 −500±37	0.78±0.02 5.3±1.7	[135]
Ti-5Ag Ti-5Ag-5Sn	3DPTM	6.30±3.30 <0.8	0.9 wt.% NaCl	−230±31 −530±49	0.89±0.05 4.6±1.9	[135]

∗ *as reported by the authors.* ∗∗ *at* 25 °C. ∗∗∗ *at. %*

Electrochemical impedance spectroscopy (EIS) has been used for studying porous Ti-electrodes [60,61,94,137,138]. However, most of the authors describe the impedance response of these electrodes by a constant phase element (CPE) that can be related to the passive oxide film [26,28,94,125,139]. Despite the complex structure of real porous electrodes, the good adjustments of experimental data obtained using electrical equivalent circuits and CPE have established the method as a standard approach. On the other hand, several works have employed the theory of De Levie, an impedance model derived as a simplified transmission line model (TLM) assuming a simple pore structure of cylindrical pores, to interpret their impedance response [60,63,108]. An alternative model has been proposed by Itagaki et al. [60] considering pores with a fractal structure. These more realistic physical models may better represent the EIS responses of porous Ti-electrodes allowing a better interpretation of the effects of porosity on the overall electrochemical response.

The aim of this work was to understand the effect of added porosity on the evolution of microstructure and the electrochemical response of a novel porous Ti-Nb-Ta-Fe-Mn alloy

exposed to SBF. In this context, a multi-technique approach was used to verify the likelihood of corrosion being triggered inside the porosity.

11.2 Experimental procedure

11.2.1 Samples preparation

Foam Ti-20Nb-11Ta-16Fe-1Mn at.% alloys were fabricated through a powder metallurgy (PM) technique applying a space holder method [63]. Metal powders (99.5%, <45 μm, NOAH Technologies) were mechanically alloyed in a RETSCH PM400 ball mill for the effective duration of 50 h (an on/off cycle of 15/15 min was used), under protective Ar atmosphere and with a ball to powder weight ratio of 10:1. Subsequently, the milled powder was mixed with $(NH_4)_2CO_3$ (99%, Loba Chemie) as a space-holder. A certain quantity of space-holder was added to obtain a porosity range between 0 and 40 %. Finally, the test cylinders were produced by uniaxial pressing at 400 MPa in a cylinder die with an inner diameter of 8 mm. The thermal cycle to remove space-holder and sintering was 1.5 h at 180 °C and 3 h at 1250 °C in a protective Ar-atmosphere, respectively. It should be noted that the sample prepared without a space holder has an inherent porosity characteristic to powder metallurgy processing. This explains the discrepancy between the used amount of space-holder and the apparent porosity resulting after sintering.

Bulk sample was obtained from a porous Ti-20Nb-11Ta-16Fe-1Mn at.% by using arc melting technique in Ar-atmosphere, by using an electrode tip of tungsten, in a water cooler copper base plate. Later, the ingot was treated at 900 °C for 72 hours under high vacuum. The apparent porosity achieved was around 3.5%.

The oxide layer formed during sintering was removed from the external surface by mechanical polishing using SiC sandpaper with successive grit sizes: #600, 800, 1200, 2400 and 4000. Then, the Ti-based alloys were cleaned with alcohol in a sonicated bath for 10 min.

11.2.2 Characterization

11.2.2.1 Porosity analysis

Macroporosity of the samples was estimated by the Archimedes method, according to the Standard Test ASTM C373-88 [64]. The specific surface area and pore size distribution were determined by the Brunauer–Emmett–Teller (BET) analysis from the N_2 adsorption/desorption isotherms (Micromeritics, 3 flex Physisorption). Additionally, the microstructure morphology and chemical composition were evaluated by a field emission-scanning electron microscope (FE-SEM, QUANTA FEG 250) equipped with energy dispersive spectrometer (EDS).

11.2.2.2 Estimation of elastic modulus

Elastic modulus was estimated using the transmission technique. For this, an electrical pulse, produced by an Agilent-33250A function generator and then amplified with a high frequency amplifier NF-HSA4011, to excite the Olympus V110 ultrasonic transducer, inducing a mechanical wave in the sample. The wave is received by a transducer of the same model on the opposite side of the sample. The emitted and received waves are acquired with the Tectronix TDS-2012B oscilloscope with 1 ns of precision. With the acquired signals, the longitudinal and transversal wave speed ($v_L$and v_T) can be estimated using the length and diameter traveled by the pulse, employing a Mitutoyo micrometer with a 0.001 mm of accuracy, and the time delay that the wave takes to reach the other side. Then the E and Poisson modulus (ν) is calculated according to the ASTM International D2845-8 [65,66] standard in agreement with Eq.1 and Eq.2

$$\nu = \frac{1-2\left(\frac{v_T}{v_L}\right)^2}{2-2\left(\frac{v_T}{v_L}\right)^2} \quad (1)$$

$$E = 2\rho v_T^2 (1-\nu) \quad (2)$$

11.2.2.3 XPS analysis

X-ray photoelectron spectroscopy (XPS) spectra were recorded using a ThermoVg K-alpha$^+$ photoelectron spectrometer with Al K_α X-ray radiation (hν = 1486 eV). The analysis chamber was operated at 10^{-6} Pa and C 1s at 284.15 eV was used as calibration reference. A complete survey scan and high-resolution scans of the Ta4f, Nb3d, Ti2p, O1s, Mn2p, and Fe2p signals were recorded. For depth profile characterization sputtering cycle were imposed consisting of 15 s Ar ions flux exposure at 3 keV. Prior to signal analysis, the spectra were processed to remove the background contribution caused by inelastically scattered electrons using the Shirley procedure. Curve fitting and peak decomposition were carried out using mixed Gauss–Lorentz shape function for each component.

11.2.3 Electrochemical characterization

11.2.3.1 Exposure

Samples were exposed to SBF (simulated body fluid) using an incubator operated at 37±1 ^oC. The SBF consisted of a solution containing (g/L): 9.00 NaCl (99.79%, Winkler), 0.43 KCl (Q.A, Winkler), 0.20 $NaHCO_3$ (Q.A, Winkler), and 0.24 $CaCl_2$ (Q.A, Winkler). The duration of exposure was selected to match the critical time for the evolution of post-operatory complications [74]. The exposure was conducted in static conditions and the SBF was refreshed every 7 days.

11.2.3.2 Electrochemical measurements and fitting method

Electrochemical measurements were carried out using a three-electrode cell with a platinum rod as the counter electrode (CE) and a saturated calomel electrode (SCE) as the reference electrode (RE). The working electrode (WE) consisted of the Ti-Nb-Ta-Fe-Mn alloy mounted in a rotating disc electrode kit (OrigaTrod, Origalys) with an exposed geometric area of 0.28 cm^2. During the measurements, a thermostatic water bath was kept at 37±1 °C and the rotation rate was set to 150 rpm. It should be noted that the sample holder was immersed in the SBF to the depth of about 2 mm, as shown in Figure 1(a), and held in this position for the entire duration of exposure, including electrochemical characterization. Electrochemical measurements were carried out each 7 days until completing the 91 days of exposure, using a potentiostat/galvanostat (VSP, Biologic). Open circuit potential (OCP) curves were registered and electrochemical impedance spectroscopy (EIS) data were collected after OCP values were stable. Impedance data were acquired over a frequency range from 25 kHz to 3 mHz with seven points per decade and using a 10 mV peak-to-peak sinusoidal voltage at E = OCP. The impedance results were fitted by using both a home-developed software called SIMAD (LISE UPR 15 CNRS, France) using the De Levie model for porous electrode response, and a new model for fractal porous electrode developed by Itagaki et al. [60] (see section 4.2 Electrochemical response). This consisted of fitting the impedance experimental data, rewriting the model (equivalent circuit) proposed in the software, using the frequency range suggested by the Kramers-Kronig relation, and repeating the adjustment every 1200 iterations until reaching the lowest χ^2 value. Finally, polarization curves were performed after 1 and 91 days, starting from $E_1=E_{OCP}$-100 mV vs. SCE to $E_2=E_{OCP}$+300 mV vs. SCE at a scan rate of 0.1 mV s^{-1}.

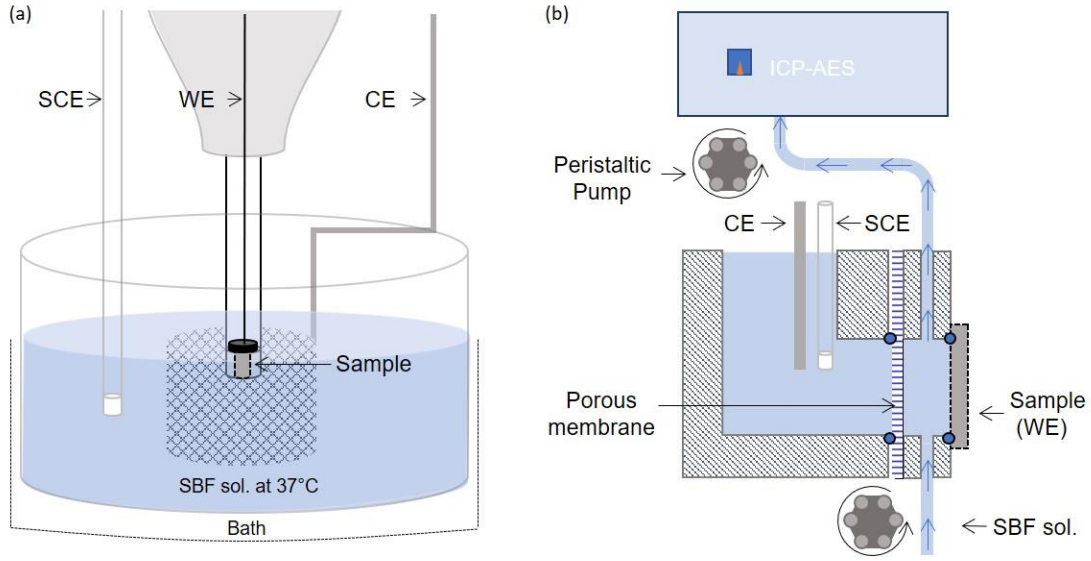

Figure 1. Schematic representation of the exposure set-up for (a) electrochemical characterization measurements and (b) quantitative analysis of ion release by ICP-AES method.

11.2.3.3 Quantitative analysis of metal ion release

In order to quantify the amount of released ions, two methods were used: droplet measurements and electrochemical flow cell.

The droplet measurement was carried out for the sample with 33% porosity and exposed for 30 days without renewing the SBF to allow for accumulation of the released ions. About 150 mL of the SBF solution was sampled from the exposure system and stirred for 20 min. The solution was subsequently transported via a capillary toward the inductively coupled plasma (ICP) analyzer (Ultima 2C Horiba Jobin-Yvon) with a flow rate of 3 $mL \cdot min^{-1}$, where the ions dissolved in the solution were quantified with a detection limit (DL) specific to each element, i.e., Ti (2.0 ppb), Nb (7.7 ppb), Ta (8.6 ppb), Mn (0.7 ppb) and Fe (3.2 ppb).

The electrochemical flow cell set-up employed for the quantification of the metal ions released under polarization condition, was coupled to a potentiostat (Reference 600™, Gamry) and consisted of a three-electrode cell with a saturated calomel electrode (SCE) and a Pt wire as a reference and counter electrode, respectively. For the measurements, the samples were mounted in an epoxy resin and then mechanically polished using emery/sandpaper grit up to #4000, cleaned by sonication in an alcohol bath for 10 min, and dried by blowing compressed air. Then, the samples were immersed in SBF during 30 days at 37±1 °C, using an arrangement coupled with an ICP system as demonstrated in Figure 1 (b). In this case, a pumping system allowed a continuous injection and extraction of the SBF, and the extracted liquid was guided directly to the ICP-AES chamber (Ultima 2C Horiba Jobin-Yvon). A steady influx of the SBF at room temperature was introduced directly to the ICP-AES analysis at the rate of 3 $mL \cdot min^{-1}$. The measurements were carried out first at OCP, followed by applied potential of constant value (1 V or 2 V), and then during a linear sweep voltammetry carried out at the rate of 0.25 $mV \cdot s^{-1}$. During all the electrochemical manipulation, the ICP measurements elapsed in-line. Finally, the C_M and v_M (dissolution rate) were calculated using a standard calibration method of AESEC (atomic emission spectroelectrochemistry) technique [67].

11.3 Results

11.3.1 Morphological characterization and surface analysis

11.3.1.1 Porosity

Table 2 shows the quantity of space-holder added and the apparent porosity of samples estimated by Archimedes methods. A sample ID was assigned in reference to the resulting apparent porosity.

Table 2. Summary of alloy foams and their corresponding porosities.

Alloy	Space holder added v/v (%)	Total apparent porosity v/v (%)	Sample ID
Ti-Nb-Ta-Fe-Mn	0	25	25%
	10	31	31%
	20	33	33%
	30	37	37%

The adsorption/desorption isotherms of the Ti-based alloy are shown in Figure 2. A reversible isotherm is observed, indicative of a typical macro-porous material according to the IUPAC classification [140]. Analysis of the isotherms by means of the BET equation [141] revealed that the micro- and meso-porosity area prior to exposure increased with the apparent porosity from 3450 to 31069 and 41771 $cm^2.g^{-1}$ for the 25%, 31% and 37% samples, respectively. After exposure, the micro- and meso-porosities decreased to 1575, 1419 and 3290 cm^2g^{-1} for the 25%, 31% and 37% samples, respectively, thus becoming similar. These results indicate that interconnected micro- and mesopores, originated from the fabrication, undergo modification during exposure.

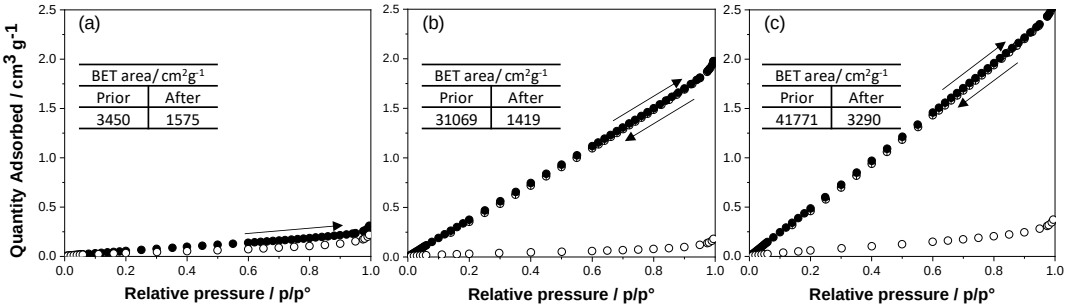

Figure 2. Nitrogen adsorption/desorption isotherms of (a) 25% (b) 31% and (c) 37% samples, prior (●) and after (○) 91 days of exposure in SBF.

11.3.1.2 FE-SEM

FE-SEM images of the Ti-based alloy as foams are shown in Figure 3. For samples with 31% porosity prior to exposure the size of some pores was close to 10 μm, which might indicate an agglomeration of the space holders because such features were not observed in the 25% porosity sample (Figure 3 (a-b)). After exposure, those pores were not significantly affected, but a slight increase in macro-porosity could be observed (see Figure 3 (d-f)). It should be noted that the darker and lighter grey colors in the SEM images are indicative of different electronic density which is consistent with the formation of two crystallographic phases corresponding to the alpha (α-Ti) and beta (β-Ti) phases [142].

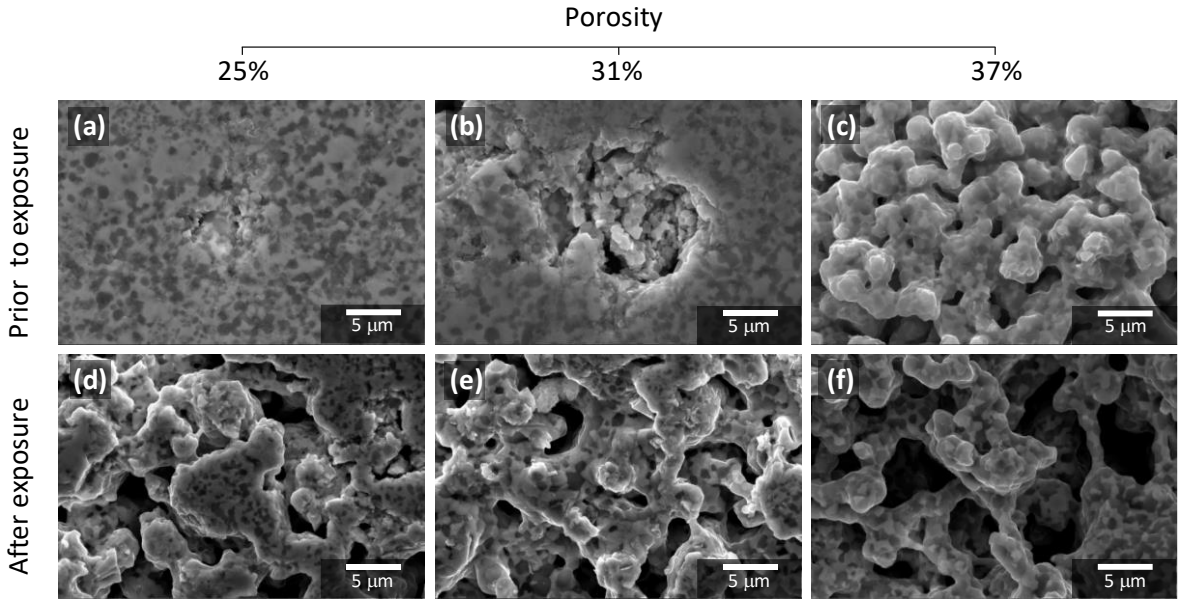

Figure 3. FE-SEM micrographs of the Ti-Nb-Ta-Fe-Mn alloy. (a,b,c) Prior exposure and (d,e,f) after 91 days of exposure to SBF.

11.3.1.3 Elastic modulus

The elastic modulus was measured through the ultrasound method as a function of porosity percentage. Table 3 shows the variation in E values when porosity increases, prior to and after exposure. Bulk material exhibited E value around 84.3 GPa, which decreases due to the added porosity. The E values prior to and after exposure did not show significant differences.

Table 3. Elastic modulus as a function of porosity percentage prior to and after exposure

Synthesis method	Porosity %	Prior to exposure		After 91 days	
		E / GPa	Error %	E / GPa	Error %
Arc Melting	3.5	84.3	48.3	-	-
Powder Metallurgy	25	11.7	18.3	11.2	14.2
Powder Metallurgy	31	8.8	9.6	8.8	11.1
Powder Metallurgy	37	4.5	11.7	5.3	20.3

11.3.1.4 XPS

The XPS spectra of the 25% porosity sample are shown in Figure 4. The survey spectra revealed a lower number of counts before exposure as compared with after exposure (see Figure 4 (a)). Additionally, the deconvolution of the selected peaks corresponding to metals, presented in Figure 4(b), revealed the formation of species with different oxidation states prior and after exposure, the relative content of which is modified after exposure increasing

the content on the surface. Titanium was found mainly as Ti^{4+} with small amounts of Ti^{2+}. In addition, Ti^{3+}, not present in the as-fabricated material, was found after exposure. Further, a clear presence of Ta^{5+}, Nb^{2+}, Nb^{+5}, Fe^{2+} and Fe^{3+} peaks was observed, which are likely associated with metal oxides. A weak signal of manganese (Mn2p) was also observed.

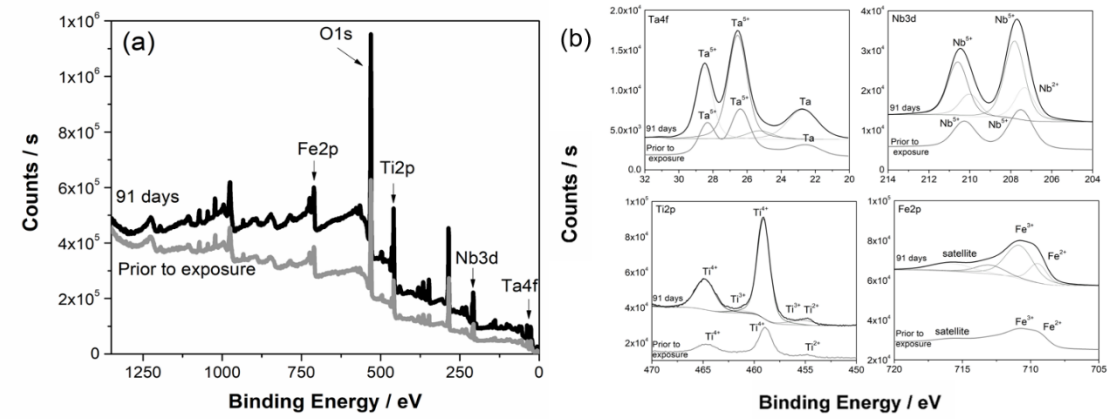

Figure 4. XPS spectra for samples with 25% porosity (a) survey scan where the lines represent samples (▭) prior to exposure, (▬) after 91 days of exposure, (b) high-resolution scans of selected signals prior and after 91 days of exposure with the corresponding peak decomposition.

The compositional depth profiles of selected elements are shown in Figure 5. The oxygen amount decreased from the average of 85 at% in the as-sintered sample to 70 at% after 91 days of exposure. The amount of alloying elements shown in Figure 5(b), revealed that the relative oxygen content decrease may be associated with the increase in Ti and Fe, whereas Ta and Nb decreased slightly after exposure.

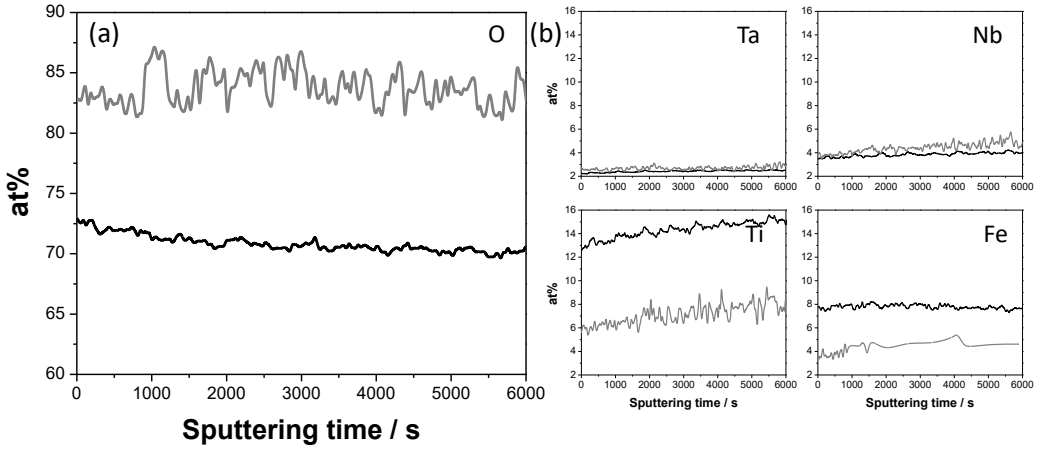

Figure 5. Depth profile of elemental composition obtained from XPS data for the 25% porosity sample for selected elements: (a) Oxygen, (b) Main alloying elements. Grey line (▭) prior exposure, and black line (▬) after 91 days of exposure.

11.3.2 Electrochemical characterization

11.3.2.1 Polarization curves

Figure 6 shows the evolution of OCP versus time and compares polarization curves recorded after 1 day and 91 days of exposure for sample with 37% of porosity. A systematic shift of OCP towards more negative values was observed during exposure and is consistent with the corrosion potential response. The shift in all cases was accompanied by a proportional increase of the overall current. Additionally, Figure 6 (b) shows the polarization curves for sample with 31% and 37% porosity after 1 day of exposure, revealing a shift of the corrosion potential toward more negative values with increased porosity. Similar cathodic and anodic current values are observed after 1-day exposure, but an increase in the current is revealed for longer exposure time, as shown in Figure 6 (c). It should be noted that the current values were reported without the effective electro-active area, which is discussed in detail in Section 4.2. Further, the polarization curves revealed a passive behavior with a slight increase of the anodic current in the anodic direction of polarization.

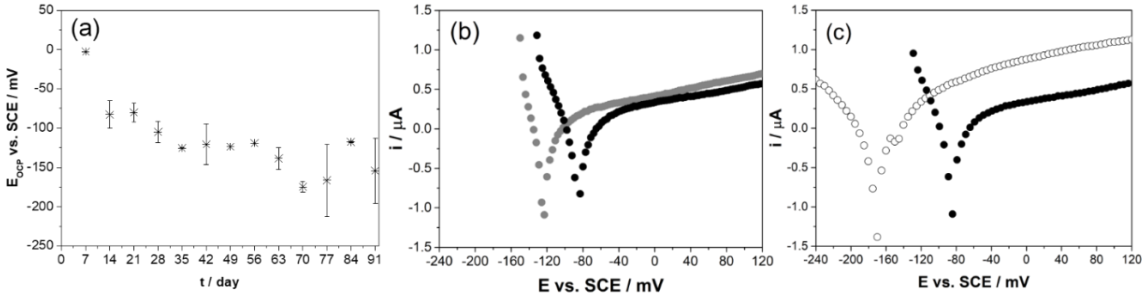

Figure 6. Electrochemical results of Ti-Nb-Ta-Fe-Mn after being exposed to SBF at 37 °C. (a) Open circuit potential as a function of exposure time for the sample with 37% porosity. Polarization curves after (b) 1 day of exposure for (●) 31% and (●) 37% porosity and (c) after (●) 1 and (○) 91 days exposure for 37% porosity.

11.3.2.2 Electrochemical impedance spectroscopy

Nyquist diagrams for each porous Ti-Nb-Ta-Fe-Mn alloy are shown in Figure 7 for selected sampling times. In all cases, a typical porous electrode behavior was observed in the selected frequency range validated by the Kramers-Kronig relation. In the low frequency range (LF), straight lines with a slight deviation from 90^{o} were observed, whereas in the high frequency range (HF) the impedance responses were characterized by straight lines with angle values close to 25° (see insert in Figure 7). It is worth noting that the impedance response related to the Ti-oxide film formation could not be detected in the frequency range studied due to the dielectric properties of the oxide film, which might appear at lower frequencies. Both experimental and fitted data adjusted by different porous electrode models proposed in the literature [24-25] will be discussed later in section 4.2.

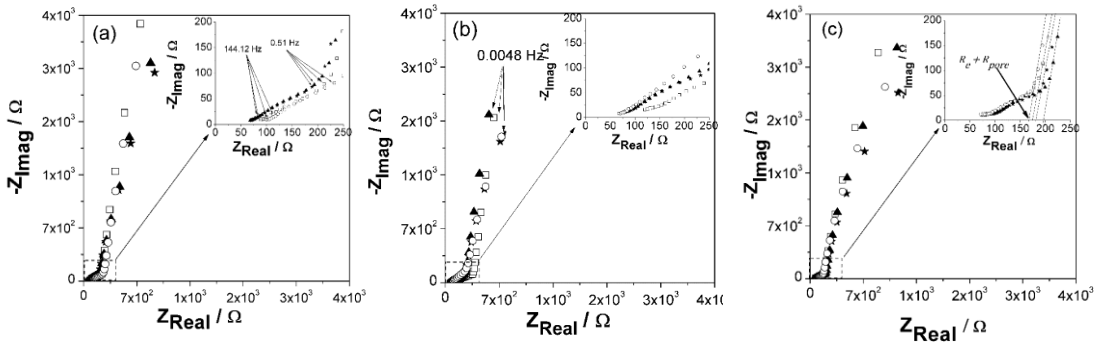

Figure 7. Nyquist diagrams of Ti-Ta-Nb-Mn-Fe samples with porosity of (a) 25%, (b) 31% and (c) 37% after exposure in SBF at 37 °C for the duration of 14 days (☐), 28 days (▲), 42 days (★), and 91 days (○).

Figure 8 shows the Bode plots for the sample with 37% porosity after correction by the electrolyte resistance [100]. The phase angle was found stable over the time of exposure with values near 75° in the LF frequency range and about 25° in the middle frequency (MF) and HF ranges. The impedance modulus also remained stable.

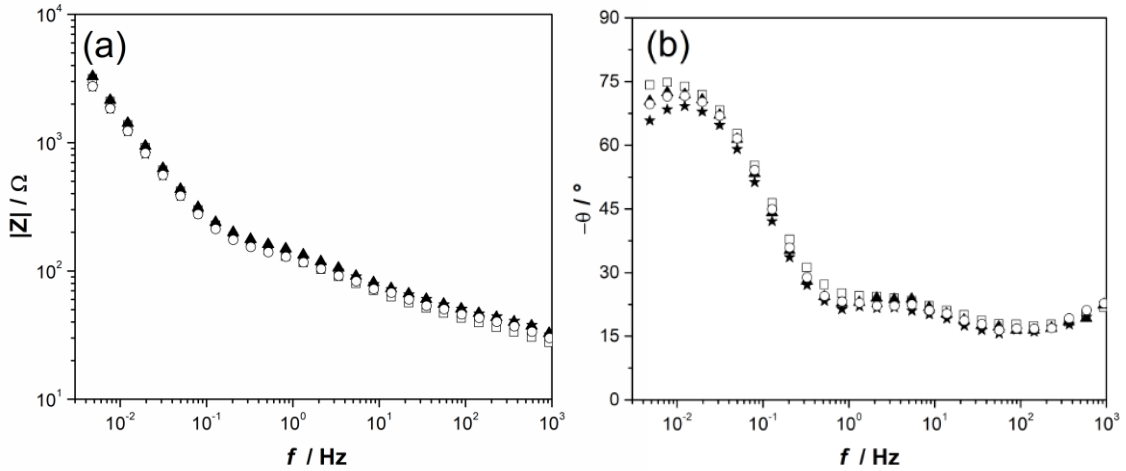

Figure 8. Bode plots of Ti-Ta-Nb-Mn-Fe sample with 37% after (☐) 14, (▲) 28, (★) 42, and (○) 91 days of exposure in SBF at 37 °C. Variation of (a) impedance module and (b) impedance phase. Data corrected by the electrolyte resistance.

11.3.3 ICP-AES monitoring

Table 4 shows the amount of each element (C_M) measured by ICP-AES from droplet SBF samples after 30 days of exposure of the sample with 33% of porosity to the SBF at 37 °C,

showing that the quantity of Ti, Nb and Ta ions released were below the detection limit (DL) of the equipment and only few ppb of Mn and Fe were detected.

Table 4. ICP-AES data from droplet samples of SBF after 30 days of exposure. DL: detection limit

M (element)	Ti	Nb	Ta	Mn	Fe
C_M / ppb	< DL	< DL	< DL	1.9	4.8

Figure 9 shows the elemental dissolution rate (ν_M) of Ti-Nb-Ta-Fe-Mn alloy measured by ICP-AES for the sample with 33% porosity after 30-day exposure in SBF at 37 °C. The simultaneous variation of the current density (i) and potential during data collection is also presented. The elemental dissolution rate was below the detection limit during the open circuit measurement. On the other hand, a slight increase in anodic current density was observed when an overpotential was applied during the linear sweep voltammetry. However, the presence of Ti or other alloying element dissolution process was not detected by the ICP-AES experiments, even considering the very low detection limit of the equipment (few ppb). As stoichiometric comparison of current to dissolution indicates that the anodic current is essentially due to the formation of insoluble oxides. The anodic current is on the order of 25-35 μA. Similarly, no elemental dissolution was observed when potentiostatic anodic over-potentials (1 and 2 V vs. SCE).

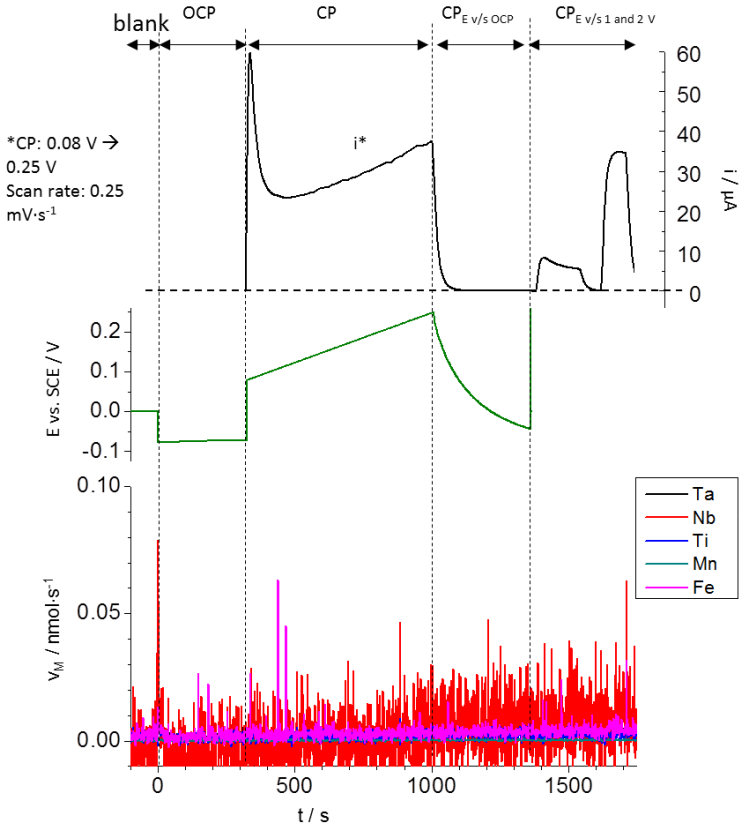

Figure 9: ICP-AES analysis of Ti-Nb-Ta-Fe-Mn alloy with 33% porosity after 30 days of exposure to SBF at 37 ºC.

11.4 Discussion

11.4.1 Microstructural effects

As mentioned previously, FE-SEM images revealed darker and lighter regions that via EDS analysis showed differences in their chemical composition (not shown here). This could be associated with the presence of different crystalline phases, such as α-Ti and β-Ti, as already discussed by Guerra et al. [28]. The α-Ti and β-Ti correspond to a hexagonal close packed (HCP) crystalline structure and a body centered cubic (BCC) crystalline structure, respectively. Pure Ti, and a great number of Ti-based alloys, exhibit an allotropy change at the β-transus temperature, below this temperature α-phase is stable and above β-phase is present [43]. The mechanical properties of Ti-based alloys can be strongly influenced by this allotropic phase transformation due to α-phase alloys exhibiting a high elastic modulus, good creep resistance, good weldability and excellent corrosion resistance whereas β-phase alloys exhibit high strength and fatigue resistance, low elastic modulus, good formability, high hardenability, and high corrosion resistance. Ti alloys are classified as α-phase, α+β-phase and β-phase depending upon their microstructure [43]. The α and β phases can be

stabilized using alloying elements. For instance, Al, O, N, C are considered as α-stabilizers and Ta, Nb, Z, W, V, Mo, Fe, Mn, Cr, Co, Ni, Cu, Si, H as β stabilizers. As mentioned above, the E of a bulk CP-Ti is close to 110 GPa [10] and in this work, the E values was around 84.3 GPa for the bulk sample and between 8.8-4.5 GPa for porous materials, which may be associated with the effect of the porosity but also to the presence of the alloying elements.
FE-SEM images also revealed an increase in pore sizes after exposure, which should only involve macro-porosity. After the immersion tests, the adsorption/desorption isotherms showed that the surface areas attributed to the micro- and meso-porosity were considerably reduced. These results suggest that meso- and micropores may be blocked by corrosion products related to the growth of a thin oxide layer (not visible in the FE-SEM images). The depth profiles of samples obtained by XPS after 91 days exposure showed a Ti and Fe enrichment on the surface, a consistency among Ta and Nb, and a decrease in O. This could indicate thickening of the oxide layer and an embodiment of these elements.

11.4.2 Electrochemical response

The OCP and E_{corr} were shifted towards more negative values with exposure time, whatever the samples porosities (see Figure 5). This behavior has been already reported by Li et al. [143], Blackwood et al. [121] and Xie et al. [27] who verified that the higher the porosity the more significant the potential shift. This was related to a negative effect for joint implant materials due to a rise of the corrosion current density. Nevertheless, the variation of those electrochemical parameters might be a consequence of an increase in the exposed surface area and not to a decrease of corrosion resistance. In fact, the FE-SEM images (see Figure 2(c,f)) and BET results (see Figure 3) showed this influence after exposure (see Table 2).
The impedance results showed a porous electrode behavior with a deviation from the De Levie model [137], which supposes a transmission line model with a simplified geometry of cylindrical pores of equal length (see Figures 6 and 7). According to De Levie, impedance of the system is described by Eqs. 3-5 [62,137]:

$$Z_{pore} = \frac{Z_{De\ Levie}}{n} \quad (3)$$

$$Z_{De\ Levie} = \sqrt{R_0 \cdot Z_0} \cdot coth\left(l\sqrt{\frac{R_0}{Z_0}}\right) \quad (4)$$

$$Z_0 = \frac{1}{j\omega C_{dl}} \quad (5)$$

where Z_0 and R_0 are the interfacial impedance (Ω·cm) and the electrolyte resistance for a one-unit length pore (Ω·cm^{-1}), respectively. R_0 is given by $R_0 = \frac{\rho}{\pi \cdot r^2}$, where ρ is the electrolyte resistivity (Ω·cm), whereas ℓ and r represent the pores length and radius. The interfacial impedance, Z_{pore}, is the impedance normalized by the number of pores "n" [137]. According to the De Levie model, the phase angle should be close to 45° and 90° in the HF

and LF range. However, three distinctive time constants are observed in Figures 6 and 7, with phase angle values lower than those proposed by De Levie, as summarized in Table 5 for the corresponding LF, MF and HF ranges.

Table 5. Impedance parameters of Ti-Nb-Ta-Fe-Mn alloy exposed to SBF at 37±1 °C estimated by graphical method.

ID sample	Time /days	$\lvert\theta_{HF}\rvert$ /deg	$\lvert\theta_{MF}\rvert$ /deg	$\lvert\theta_{LF}\rvert$ /deg	R_e+R_{pore} x10^4 / Ω·cm^2
25%	14	21 ± 5	26 ± 7	82 ± 4	0.66
	28	23 ± 2	28 ± 4	79 ± 1	0.74
	42	22 ± 2	29 ± 2	80 ± 5	0.91
	91	21 ± 0.3	27 ± 4	82 ± 1	1.15
31%	14	28 ± 3	26 ± 1	82 ± 11	3.93
	28	28 ± 2	29 ± 4	82 ± 5	3.14
	42	29 ± 0.1	29 ± 0.1	80 ± 7	3.13
	91	26 ± 2	31 ± 4	77 ± 3	4.32
37%	14	22 ± 3	24 ± 3	80 ± 6	2.55
	28	23 ± 2.	24 ± 4	80 ± 2	3.34
	42	22 ± 1	22 ± 2	79 ± 1	2.92
	91	23 ± 1	23 ± 4	80 ± 2	3.38

As proposed by Lasia [62], R_e+R_{pore} values were determined by the extrapolation of the LF range slope to the real impedance axis, as shown in Figure 7 (c). It should be noted that R_{pore} corresponds to the electrolyte resistance inside the pores. Table 5 shows that the R_e+R_{pore} depends on the introduced porosity and increases slightly with exposure time, which could indicate an increase of ρ_s inside the pore, if the l to r ratio remains constant. Thus, the increase of pore resistance can be attributed to the rise in the surface area effectively in contact with the electrolyte rather than significant weakening of the protective layer. Cooper et al. [138] suggested that deviations from the De Levie theory might be attributed to the pore shape [108]. Figure 10 shows the Nyquist plots of the 37% porosity sample after 91 days of exposure, reporting experimental and fitted data using the (a) De Levie's and (b) Itagaki (to be discussed later) models. Figure 10 (a) shows a poor fitting in the HF range, indicating that the pore structure must strongly deviate from that proposed by De Levie and evidenced by the high value of χ^2, close to 10.

Table 6. Fit parameters of impedance data obtained for the Ti-Nb-Ta-Fe-Mn alloy exposed to SBF at 37±1 °C estimated from De Levie model.

ID sample	Time /days	C_{dl}^{*} ×10^{-2} / F·cm^{-2}	C_{dl}^{**} ×10^{-6} / F·cm^{-2}
25%	14	3.54	40
	28	3.90	44
	42	3.90	44
	91	4.25	48
31%	14	4.96	56
	28	5.67	64
	42	6.38	72
	91	6.03	68
37%	14	5.32	60
	28	5.67	64
	42	6.40	72
	91	6.03	72

* from the geometrical surface area. ** from the electro-active area estimated by using n and ℓ parameters from the De Levie model.

Despite the discrepancy, De Levie's theory is still an interesting tool for impedance analysis of porous electrodes (see Figure 11 (a,b)) when exploring the deviation of pores' geometry from the idealized cylinder assumed by the model. For instance, it is possible to evaluate the effect of the electro-active surface area on the capacitance of the double-layer (C_{dl}). The values of C_{dl} can be estimated assuming geometrical area as the electro-active interface (C_{dl}^{*}) or using n and ℓ parameters from De Levie theory (C_{dl}^{**}). Table 6 shows that these values are orders of magnitude different indicating a considerable contribution of the effective electro-active area. In consequence, the values of current densities of porous electrodes reported in literature should be revisited for proper interpretation of corrosion rate.

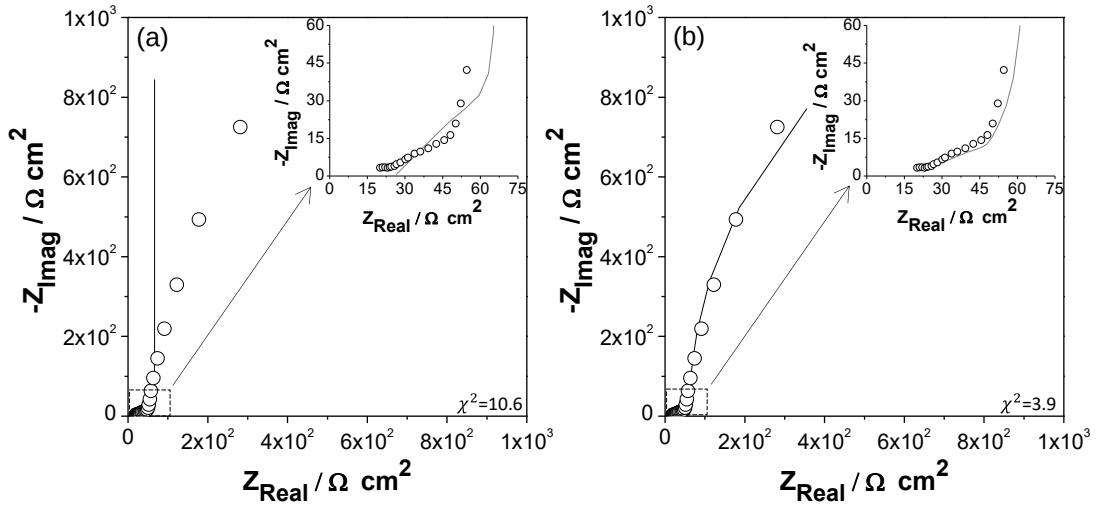

Figure 10. Nyquist diagrams of Ti-Nb-Ta-Fe-Mn sample with 37% porosity after 91 days of exposure in SBF at 37 °C with (○) experimental and (—) fit data using: (a) De Levie model, and (b) Itagaki model with triple pore structure.

A better quality fit of the EIS data is obtained by using the fractal model proposed by Itagaki et al. [60] (Figure 10(b)). The improvement was achieved by considering secondary and ternary porous structures at different levels of topological hierarchy, each level having a different effect on the electric double-layer. The model can be summarized by Equations 6-10:

$$Z_{ma} = \frac{\sqrt{R^*_{ma} \cdot Z^*_{ma}} \cdot coth\left(l_{ma}\sqrt{\frac{R^*_{ma}}{Z^*_{ma}}}\right)}{n_{ma}} \quad (6)$$

$$Z^*_{ma} = \frac{1}{\left(\left(\frac{1}{\left(\frac{Z_{me}}{n_{me}}\cdot(1-\xi)\right)}\right)+j\omega\xi C^*_{dl}\right)} \quad (7)$$

$$Z_{me} = \frac{\sqrt{R^*_{me} \cdot Z^*_{me}} \cdot coth\left(l_{me}\sqrt{\frac{R^*_{me}}{Z^*_{me}}}\right)}{n_{me}} \quad (8)$$

$$Z^*_{me} = \frac{1}{\left(\left(\frac{1}{\left(\frac{Z_{mi}}{n_{mi}}\cdot(1-\xi)\right)}\right)+j\omega\xi C^*_{dl}\right)} \quad (9)$$

$$Z_{mi} = \frac{1}{j\omega C^*_{dl}} \quad (10)$$

where $Z_{ma,me,mi}$ described the interfacial impedance per unit area of macro/meso/micropores, $R^*_{ma,me}$ was the solution resistance per unit length of macro/mesopores, $n_{ma,me}$ represented the number of macro/mesopores on the electrode surface of macro/mesopores, $Z^*_{ma,me}$ was considered as the impedance of electric double-

layer interface part of macro/mesopores, $l_{ma,me}$ as the depth of macro/mesopores, ξ represented the ratio of area for electric double-layer part to whole inner wall, and C_{dl}^{*} was defined as the electric double-layer capacitance. By using the new fractal model, the C_{dl} values were also estimated, but this model allowed the differentiation between macro-, meso- and micropores. It should be noted that the electro-active area can play an even more significant role. For instance, C_{dl} values related to macro-pores varied between 0.3-2.8 x10^{-3} F·cm^{-2} for 25% porosity, 35.5-49.6 x10^{-3} F·cm^{-2} for 31% porosity, and 0.2-0.6 x10^{-3} F·cm^{-2} for 37% porosity with exposure time, using the geometrical area. Nevertheless, the C_{dl} values for meso- and micro-pores were significantly larger than those for macro-pores, being close to 3 F·cm^{-2}.

Corroborating the EIS analysis, a physical interpretation of the impedance models was proposed for the porous Ti-based alloy/electrolyte interface as shown in Figure 11(c). The impedance related to the oxide film formation could be neglected due to its dielectric properties, implying a larger impedance than the porous electrode response.

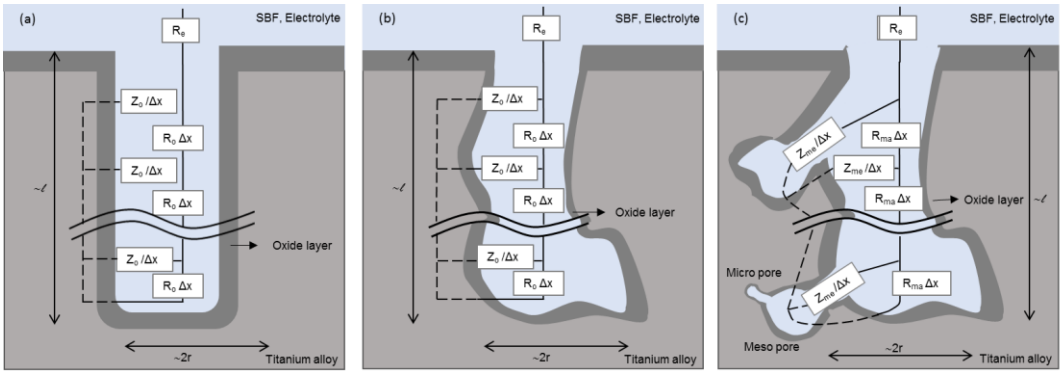

Figure 11. Schematic representation of the physical model for porous Ti-Nb-Ta-Mn-Fe electrodes obtained by PM technique based in the transmission line model. (a) Perfect cylindric pores, (b) non-idealized cylindric pores, and (c) micro, meso and macro-pores.

Finally, the elemental dissolution concentration measured by ICP-AES for a Ti-Nb-Ta-Fe-Mn alloy with 33% porosity after 30 days of exposure were not quantifiable, remaining under the detection limit. However, ICP-AES analysis from a droplet of SBF detected a very low concentration of Fe and Mn, both at the ppb level. This is accordance with polarization and EIS results, which allows deducting that the oxide layer initially present in the as-fabricated foams thickens during exposure, providing more effective protection; whereas the apparent increase in anodic current should be attributed to the increase of effective area of the electro-active interface.

11.5 Conclusions

The effect of introducing additional porosity to a Ti-based alloy has been studied for orthopedic applications, focusing on the microstructural and electrochemical perspectives. An increase of macroporosity was shown by analysis of FE-SEM images, whereas a closure of smaller pores was indicated by the absorption/desorption isotherms. The formation and thickening of an oxide film were detected by XPS, and the electrochemical response revealed passivity of the oxide film sustained for the duration of exposure but was not influenced by a longer exposure. To conclude, the metallic ions released during exposure were found sufficiently low leading to the idea that the Ti-Nb-Ta-Fe-Mn alloy with added porosity can be a promising candidate in replacing trabecular/cortical bone tissue.

The application of the fractal model proposed by Itagaki et al. [60] provided a good fitting of the EIS diagrams, supporting the complex pore structure indicated by the absorption/desorption isotherms.

12 ARTICLE IV

Tribological Performance of Porous Ti-Nb-Ta-Fe-Mn Alloy in Dry Condition

Carolina Guerra[1], Magdalena Walczak[1,2]*, Mamié Sancy[2,3], Carola Martinez[3,4], Claudio Aguilar[4] and Marek Kalbarczyk[5,6]

[1]Departamento de Ingeniería Mecánica y Metalúrgica, Pontificia Universidad Católica de Chile (PUC), Santiago 7820436 and Chile
[2]Centro de Investigación en Nanotecnología y Materiales Avanzados, CIEN-UC, PUC, Santiago 7820436, Chile.
[3]Escuela de Construcción Civil, Pontificia Universidad Católica de Chile, Santiago 7820436, Chile.
[4]Departamento de Ingeniería Metalúrgica y de Materiales, Universidad Técnica Federico Santa María, Valparaíso 2390123, Chile.
[5]Łukasiewicz Research Network, Institute for Sustainable Technologies, Radom 26-600, Poland.
[6]Faculty of Mechanical Engineering, Kazimierz Pułaski University of Technology and Humanities in Radom 26-600, Poland.

*Correspondence: mwalczak@ing.puc.cl; Tel: +56 2 23544627

Keywords: Ti-based alloy; porosity; XRD; coefficient of friction; wear

12.1 Introduction

Ti-based alloys have been widely used in the orthopedic industry and today as porous materials have gained particular interest due to the possibility of mimicking the elastic modulus (E) of natural bone and thus avoiding failures by stress shielding [10,14]. Nonetheless, the addition of porosity to the metal matrix may also modify other properties related to biocompatibility [69], corrosion [29], and wear resistance [144,145]. Although some studies have shown that the corrosion resistance may decrease if porosity is added to Ti-based alloys [25]. However, in a previous study, the new Ti-Nb-Ta-Fe-Mn alloy was shown to remain passivated after 91 days of exposure to a simulated body fluid despite high degree of porosity. Also, no ion release was observed after high overpotential was applied, suggesting that passive layer composed by Ti, Nb, and Fe protect the surface against corrosion [29]. On the other hand, regarding tribological properties, Ti-based alloys have been generally considered of poor resistance attributed to low capacity for work hardening [23], even when sliding against a softer material [10,24], requiring targeted alloying or coating. In this context, only a few studies have been focused on the tribological response of porous alloys. Liu et al. [41] reported the porosity-reduced resistance to wear of CP-Ti (commercially pure Ti), which was demonstrated by an increase in the coefficient of friction (COF) and wear volume. Whereas, Choi et al. [42] showed a considerable rise in the wear mass loss of Ti bulk over the sliding distance of 300-2000 m as compared with porous samples. Additionally, they studied the porous Ti-W alloy reporting an improved wear resistance of the foam attributed to the incorporation W, which would increase hardness of

the alloy. Indeed, intermetallic compounds demonstrate generally superior mechanical properties as compared to solid solutions, increasing stiffness and thus improving wear resistance [146]; although some specific types of intermetallic compounds might also be associated with lower machinability [147]. There is, however, no agreement on the influence that porosity has on wear and friction performance, in particular the individual aspects of porosity percentage, pore shape and size, for a given alloy composition [144,145].
Therefore, the present work aims at evaluating the tribological performance of a novel porous Ti-Nb-Ta-Fe-Mn alloy. Samples were prepared with a variation of porosity percentages, then were characterized by XRD, FE-SEM as well as tribological tests under dry conditions. Clarifying the effect of porosity on tribological performance offers an opportunity for biomedical applications for which the alloys has already been shown of interest for its mechanical properties and corrosion resistance.

12.2 Experimental

12.2.1 Preparation of Samples

The Ti-20Nb-11Ta-16Fe-1Mn (at.%) composition was obtained by mechanical alloying in a planetary mill. The bulk sample (considered as 0% porosity) was obtained by Spark Plasma Sintering (SPS) at 1000 °C and 60 MPa for 7 min holding time. The 30% and 60% porosity samples were obtained by the Powder Metallurgy (PM) technique using ammonium bicarbonate (NH_4HCO_3) as space holder. The materials were compacted at 430 MPa and then sintered in two steps (1.5 h at 180 °C followed by 3 h at 1300 °C) and cooled at the rate of 5 °C·min^{-1} as described in Ref. [29] .

12.2.2 Material Characterization

Chemical composition of the sintered alloys was conducted using elemental mapping (EM) and dispersive X-Ray spectroscopy (EDX) coupled to an emission-scanning electron microscope (FE-SEM) QUANTA FEG 250 in high vacuum ($3.7 \cdot 10^{-4}$ Pa). Phase composition was characterized by X-ray diffraction (XRD), using a multipurpose powder diffractometer STOE STADI MP, equipped with Cu-Kα_1 radiation source (λ =1.54056 Å, curved Germanium (111) monochromator of the Johann-type) and a microstrip detector DECTRIS MYTHEN 1K. The phases were identified using MATCH! software version 3.9.0.158 equipped with the Crystallography Open Database (COD). Electrochemical characterization and data on corrosion products can be found in Ref. [29].

12.2.3 Tribological Characterization

For the tribological testing, the samples were mounted in a thermosetting resin, cut and polished to obtain a suitable surface of low roughness, then cleaned using isopropyl alcohol. A ball-on-disc tribotester (NTR2 nano tribometer produced by CSM instruments) was used,

set to oscillating mode, operated at 20 ± 1 °C under technically dry conditions. As counter specimen Al_2O_3 balls of 2 mm of diameter were used, applying 1000 mN of load with stroke of 0.6 mm (0.3 mm amplitude). The maximum linear speed was 1 $cm \cdot s^{-1}$, and the test was run for 100,000 cycles. Ball material and test parameters were selected on the base of preliminary tests. The wear tracks of tested specimens (three per sample) were analyzed using optical profilometer (Talysurf CCI- Lite Non-contact 3D profiler), extracting three profiles from each sliding path: one central and two adjacent (100 µm from the central).

12.3 3. Results and Discussion

12.3.1 Morphological and Microstructural Characterization

Figure 1 (a,b) exemplifies the microstructure and phase composition of the 30% porosity sample. The superior view FE-SEM images reveal the interconnected porous structure produced during sintering, where two types of pores are apparent: the fine pores (~5 µm) inherent in the manufacturing method, and larger pores (~450 µm) produced by removal of the space holder as are indicating into the figure. Figure 1(c) shows the elemental contrast by a high magnification cross-section FE-SEM image, revealing a bi-modal composition of darker and lighter regions corresponding to Ti-rich and Nb-Ta-rich phases. The overall distribution of the alloying elements (Figure 1(b)) shown a homogenous distribution of the alloying elements with relatively low content of Mn, which is indicative of the solid-state reaction was achieved. On the other hand, analysis of the X-ray diffraction pattern in Figure 1(d), reveals the presence of Ti compounds. In the peak around 38.5° the contribution of two phases β-type (cubic, Im3m) are found, which are identified as TiNb and TiTa. In addition, four compounds are associated with the remaining peaks, among them TiFe (cubic, Fd3m), TiO_2 (cubic, Fm3m), $Nb_{0.3}Ti_{0.7}$ (orthorhombic, Cmcm) and FeNb (rhombohedral, R3m). Thus, the alloy consists mainly of the β-phase, known to provide stiffness and ductility without compromising mechanical strength of a Ti-alloy [10]. Whereas, intermetallic compounds, such as the $Nb_{0.3}Ti_{0.7}$, would provide hardness to the softer matrix, reinforcing the alloy [146,148,149].

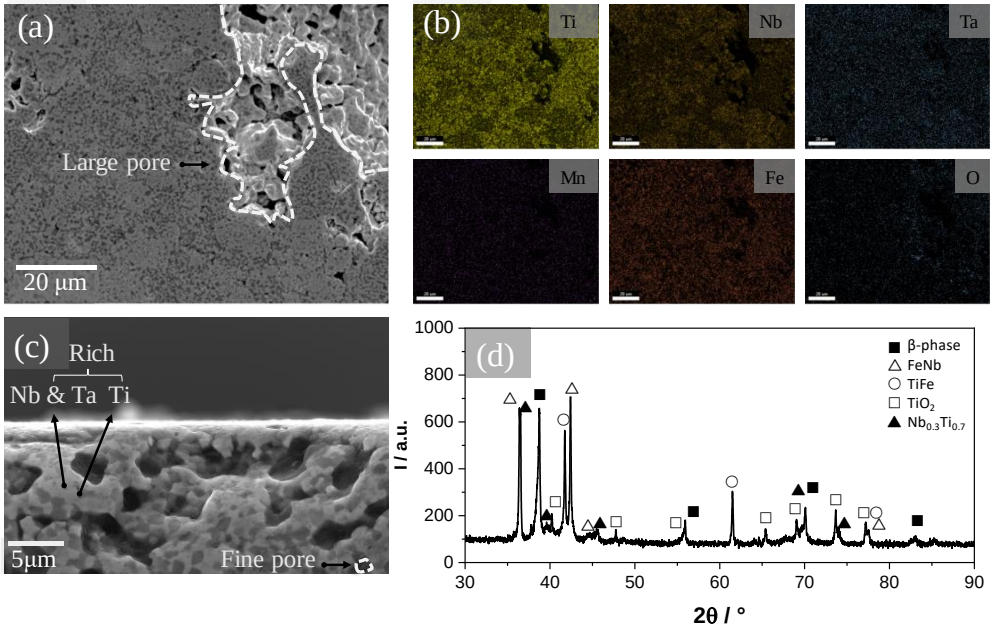

Figure 1**.** Microstructure and composition of as-sintered 30% porosity sample: (a) superior FE-SEM micrograph, (b) Elemental mapping of the alloying elements in image (a), (c) cross-section FE-SEM micrograph and (d) XRD pattern with peaks marked with the corresponding phases.

12.3.2 Friction Performance

Figure 2 summarizes the evolution of COF during the tests, revealing that the friction response differs for the bulk and porous materials. For the bulk and 60% porosity samples, a stable COF is observed, with the average values of 0.78 and 0.22, respectively. The 30% porosity sample experienced a shift of COF from 0.2 to 0.75 after a variable duration of the early stage, indicated by an arrow in Figure 2(b).

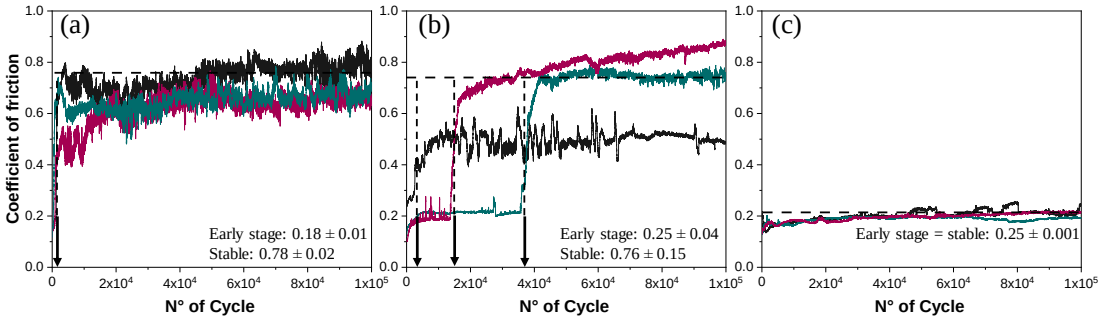

Figure 2. Evolution of COF during test: (a) bulk sample, (b) 30% porosity and (c) 60% porosity samples. Each curve is an independent measurement. The arrows indicate duration of the early stage.

The COF at steady-state registered for bulk and 30% porosity samples is similar to bulk Ti-6Al-4V, which is typically reported around 0.7 for comparable test conditions [150,151]. This observation indicates that the shift in the COF of the 30% porosity sample is associated with the change of friction mechanism, possibly associated with the accumulation of wear debris inside the pores. Such effect was shown by other authors for a Ti-6Al-4V coating, in which porosities percentage and pore diameters of approx. 13% and 25 µm, respectively, contributed to the accumulation of debris by the pore-filling mechanism [144]. The randomness in response of the sample with 30% porosity is attributed to variability of number of pores that are included in the initial contact area. This interpretation would also explain the prolonged steady state of the sample with 60% porosity that can absorb more debris. A similar result has been observed in TiNbC coatings, where debris was stacked at the bottom of the wear track, not participating in the process [152].

12.3.3 Wear Performance

Figure 3 shows representative 3D images and center cross-sections of the sliding track. The track on the 60% sample is the narrowest and most shallow (note the scale of the depth axis). The average depth of wear track on the bulk and 30% samples is similar, but the cross-section area for 30% sample is higher, also revealing large pores. Since the surface selected for the test was free of large pores before testing, these pores must have emerged during the test.

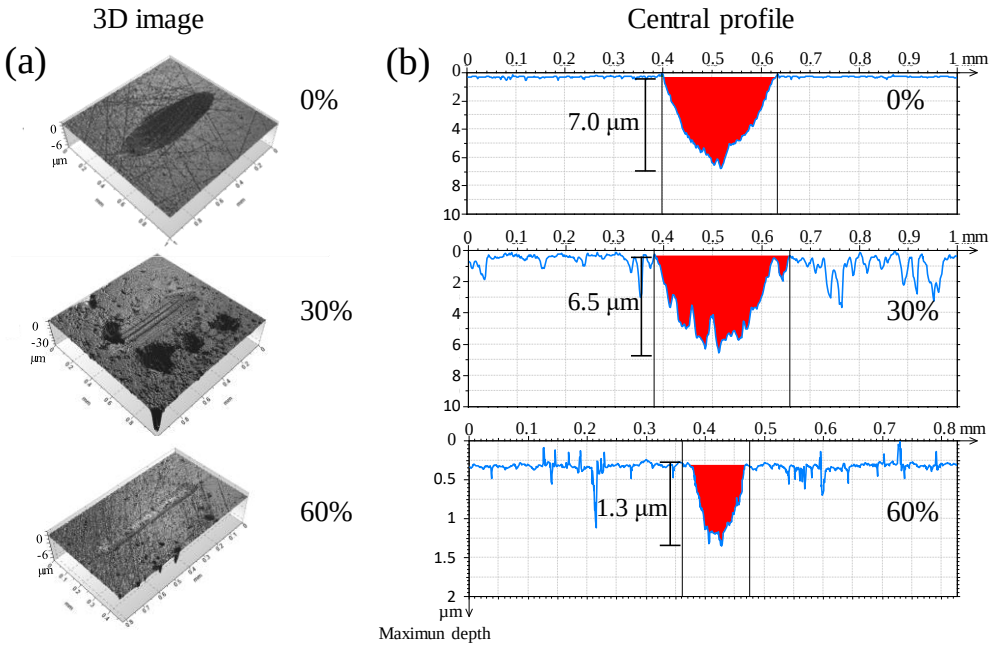

Figure 3. Images of wear tracks on the surface obtained by (a) optical profilometer for samples with different porosity and (b) the scratch profile after the being tested.

The wear track for bulk and 30% porosity samples reveal that the alumina ball penetrated deeper than in the 60% porosity sample, in case of which, after 100,000 cycles the ball hardly penetrated the most porous surface. This observation is indicative of a distinctive wear system that developed between the two bodies, in which both effective surface of contact and the debris generated in the process would play a different role. In addition, the amount of surface oxides, present in the interior of the sintered structure should be taken into account as is known to be potentially detrimental, when released as debris [144,145]. The lesser penetration in the more porous sample is then indicative of debris removal. Such an effect was observed by Dubrujeaud et al. [145] *in* a Distaloy AE of various porosity tested in dry conditions. Their explanation was that the debris, in this case mainly iron oxide particles, was trapped inside the pores. Moreover, the effect was most notorious for pores larger than 12 μm. For smaller pores, the debris would be participating in the wear process as a third body, leaving wear tracks similar to those shown in Figure 3(a) for the 30% porosity.

Table 1 summarizes the numerical values of the wear results and selected functional parameters determined from Abbot-Firestone curves [153,154] measured prior tribotesting: core roughness depth (S_k), which represents the efficient roughness, and the areal height difference (S_{dc}) calculated for upper 50% of surface points were determined. The high value of S_k is associated with irregularities susceptible to shear stress, and generation of hard debris enhancing the "third body" abrasion mechanism, i. e. a system composed by debris, ball and sample. The S_k value for 30% porosity sample is higher than the other, demonstrating to be non-uniform and to be rougher, compared with the others, and therefore would be more susceptible to suffer wear as was observed by Czyrska-Filemonowicz et al. [155]. In general, the higher bearing ratio is related to the larger contact area [156]. Although the test load was the same in each test, it resulted in higher contact pressures for samples with lower bearing ratio, thus rising wear intensity. The 60% porosity sample provides a higher bearing ratio, and because the pores are small and shallow, the S_{dc} value is lower compared with the 30% porous sample. Thus, the pace of bearing ratio rises. In the case of 30% porosity, new pores emerge during the wear progress, limiting the bearing ratio and reducing the contact area, leading to higher contact stresses and enhanced wear intensity, as is observed also through S_{dc} and S_k [154].

Table 1. Summary of wear data and functional parameters

ID / %	E / GPa	Max. depth / μm	Cross-section areas / μm^2	S_k / μm	S_{dc} / μm	Wear rate / $m^3 \cdot N^{-1} \cdot m^{-1}$
bulk	48.8±19.2	6.3±1.2	856.6±204.8	0.07	0.08	$6.0\pm2.0\times10^{-7}$
30	8.8±2.1	5.4±2.6	1,111.0±130.1	0.50	0.81	$5.5\pm4.2\times10^{-7}$
60	5.7*	0.6±0.3	28.8±0.2	0.07	0.16	$2.7\pm1.2\times10^{-7}$

*Estimated by Gibson-Ashby relation [16].

The elastic modulus as is observed from the table decrease as a function of porosity percentage achieving values around 6 GPa for higher porosity sample [14]. The wear rate of the sample with the highest porosity was twice less than the bulk, which is related to the type of abrasion, where in the first one, a two-body abrasion occurred while in the bulk take place three-body abrasion [157]. However, it is expected when the sample with 60% filled their pores with debris, the wear rate and COF increase.

On the other hand, considering the phase composition of the alloy, good resistance of the bulk metal to wear can be expected owing to a combination of low elastic modulus and effective hardness provided by the presence of intermetallic compounds as explained by other authors [146,158]. Also, the presence of niobium oxide (Nb_2O_5) formed inside the pores during sintering [29], can be expected to provide lubrication, which is beneficial for lowering the wear of implants, as reported by Dinu et al. [159].

Figure 4 shows the appearance of the Al_2O_3 balls, which reveals the effective contact area after 100,000 cycles. This contact area is significantly lower for the 60% porosity sample, which is in agreement with the observed above by COF and wear track. Although the contact area is similar for bulk and 30% porosity, the mechanism of wear is different. Whereas scars and grooves are observed for 30%-Al_2O_3 pair, layers of material are visibly transferred from the sample to the ball [145]. These observations are indicative of abrasive and adhesive wear mechanisms [24,150], respectively.

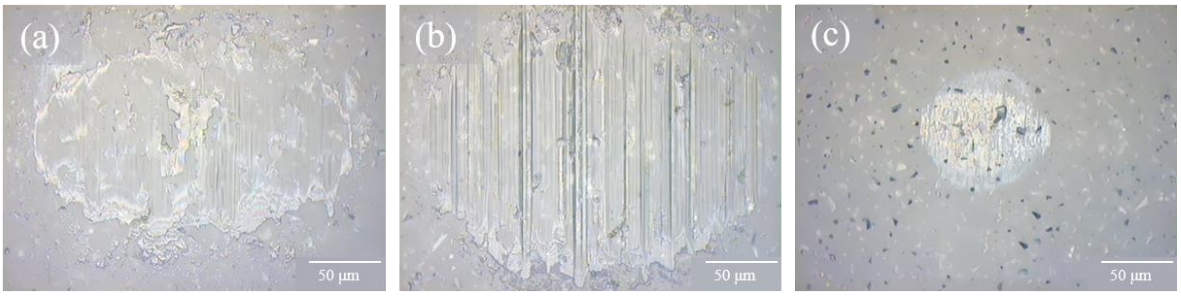

Figure 4. Optical images of the contact areas observed on the alumina balls after completing 100,000 test cycles on (a) bulk, (b) 30% and (c) 60% porosity samples.

Such a difference in wear mechanism may be caused by a dissimilarity in the relative hardness or by the appearance of the wear products at the interface between the target alloy and the counter surface, i.e. the test ball. Since the hardness of the sintered matrix can be expected similar, the difference should be attributed to the debris, as observed by Dubrujeaud et al. [145] and Munagala et al. [144]. For the bulk sample, at the early stage, abrasive wear is likely to set in, but after accumulating plastic deformation, a debris was evidently generated and transferred to the surface of the ball, which is consistent with the observation of Haftlang et al. [160]. However, the wear mode of the 30% porosity sample is dominated by the three-body mechanism, consisting of the target surface, the ball, and the unrestricted debris, which can be deduced from the deep and marked wear tracks at the ball surface. On

the other hand, the 60% porosity surface paired with the Al_2O_3 ball, has shown the least damage of a type characteristic to the two-body, which corroborates with the conclusion that the debris must have been absorbed by the pores in this case.

12.4 Conclusions

The highly porous Ti-Nb-Ta-Fe-Mn alloy was shown to have a superior tribological response as compared to a bulk sample, exhibiting a consistently lower COF. The wear rate was twice as low as that of the bulk sample and stable in time. In the case of intermediate porosity, the COF was significantly lower, but after an initial period of variable duration, it increased to the value of bulk coefficient.

Both friction and wear behavior are mainly explained by the bearing ratio of the porous materials and the debris generated during testing. The debris can be lodged in the pores, modulating the friction and wear responses. On the other hand, the combination of β-titanium and presence of intermetallic phases provided mechanical properties that favor resistance to wear. However, once the pores are filled with the wear debris, the COF increases, and large pores are generated in association with increased contact pressures. Since the pores may collaborate in delaying wear of the porous Ti-based alloy, a beneficial tribological performance can be expected in application for joint replacement.

13 REFERENCES

[1] Organización Mundial de la Salud, La esperanza de vida ha aumentado en 5 años desde el año 2000, pero persisten las desigualdades sanitarias, WHO. (2016). http://www.who.int/mediacentre/news/releases/2016/health-inequalities-persist/es/ (accessed 11 December 2017).

[2] U. Martín, S. Esnaola, C. Audicana, A. Bacigalupe, Impacto de la morbilidad en la salud de la población del país vasco 2002-2007: Una visión integral a través de las esperanzas de salud, Rev. Esp. Salud Publica. 85 (2011) 469–479. https://doi.org/10.1590/s1135-57272011000500006.

[3] J.M. Grosflam, E.A. Wright, P.D. Cleary, J.N. Katz, Predictors of blood loss during total hip replacement surgery, Arthritis Care Res. (Hoboken). 8 (1995) 167–173. https://doi.org/10.1002/art.1790080309.

[4] D. Ancelin, N. Reina, E. Cavaignac, S. Delclaux, P. Chiron, Total hip arthroplasty survival in femoral head avascular necrosis versus primary hip osteoarthritis: Case-control study with a mean 10-year follow-up after anatomical cementless metal-on-metal 28-mm replacement, Orthop. Traumatol. Surg. Res. 102 (2016) 1029–1034. https://doi.org/10.1016/j.otsr.2016.08.021.

[5] O. of the S.G. (US), Bone Health and Osteoporosis, Office of the Surgeon General (US), 2004. http://www.ncbi.nlm.nih.gov/pubmed/20945569 (accessed 12 December 2017).

[6] E. Gentleman, R.J. Swain, N.D. Evans, S. Boonrungsiman, G. Jell, M.D. Ball, T.A. V. Shean, M.L. Oyen, A. Porter, M.M. Stevens, Comparative materials differences revealed in engineered bone as a function of cell-specific differentiation, Nat. Mater. 8 (2009) 763–770. https://doi.org/10.1038/nmat2505.

[7] J. Gallo, J. Vaculova, S.B. Goodman, Y.T. Konttinen, J.P. Thyssen, Contributions of human tissue analysis to understanding the mechanisms of loosening and osteolysis in total hip replacement, Acta Biomater. 10 (2014) 2354–2366. https://doi.org/10.1016/j.actbio.2014.02.003.

[8] M.I.Z. Ridzwan, S. Shuib, A.Y. Hassan, A.A. Shokri, M.N. Mohammad Ibrahim, Problem of stress shielding and improvement to the hip implant designs: A review, J. Med. Sci. 7 (2007) 460–467. https://doi.org/10.3923/jms.2007.460.467.

[9] C. Caouette, L.H. Yahia, M.N. Bureau, Reduced stress shielding with limited micromotions using a carbon fibre composite biomimetic hip stem: a finite element model., Proc. Inst. Mech. Eng. H. 225 (2011) 907–19. https://doi.org/10.1177/0954411911412465.

[10] M. Geetha, A.K. Singh, R. Asokamani, A.K. Gogia, Ti based biomaterials, the ultimate choice for orthopaedic implants - A review, Prog. Mater. Sci. 54 (2009) 397–425. https://doi.org/10.1016/j.pmatsci.2008.06.004.

[11] X. WANG, J. LI, R. HU, H. KOU, Mechanical properties and pore structure deformation behaviour of biomedical porous titanium, Trans. Nonferrous Met. Soc. China. 25 (2015) 1543–1550. https://doi.org/10.1016/S1003-6326(15)63756-6.

[12] G. Manivasagam, D. Dhinasekaran, A. Rajamanickam, Biomedical Implants: Corrosion and its Prevention, Recent Patents Corros. Sci. 2 (2010) 40–54. https://doi.org/10.2174/1877610801002010040.

[13] M. Niinomi, Y. Liu, M. Nakai, H. Liu, H. Li, Biomedical titanium alloys with

Young's moduli close to that of cortical bone, Regen. Biomater. 3 (2016) 173–185. https://doi.org/10.1093/RB/RBW016.

[14] C. Aguilar, C. Guerra, S. Lascano, D. Guzman, P.A. Rojas, M. Thirumurugan, L. Bejar, A. Medina, Synthesis and characterization of Ti-Ta-Nb-Mn foams, Mater. Sci. Eng. C. 58 (2016) 420–431. https://doi.org/10.1016/j.msec.2015.08.053.

[15] C. Salvo, C. Aguilar, D. Guzmán, I. Alfonso, R. V Mangalaraja, Mechanically enhanced novel Ti-based alloy foams obtained by hot pressing, Mater. Sci. Eng. A. 759 (2019) 112–123. https://doi.org/10.1016/j.msea.2019.05.022.

[16] J. Stráský, P. Harcuba, K. Václavová, K. Horváth, M. Landa, O. Srba, M. Janeček, Increasing strength of a biomedical Ti-Nb-Ta-Zr alloy by alloying with Fe, Si and O, J. Mech. Behav. Biomed. Mater. 71 (2017) 329–336. https://doi.org/10.1016/j.jmbbm.2017.03.026.

[17] G. Xie, F. Qin, S. Zhu, D. V. Louzguine-Lugzin, Corrosion behaviour of porous Ni-free Ti-based bulk metallic glass produced by spark plasma sintering in Hanks' solution, Intermetallics. 44 (2014) 55–59. https://doi.org/10.1016/j.intermet.2013.08.013.

[18] J.W.H. and H.N.G.W. M.F. Ashby, A.G. Evans, N.A. Fleck, L.J. Gibson, Metal Foams : A Design Guide, Butterwort, 2000.

[19] P.G. Esteban, E.M. Ruiz-Navas, E. Gordo, Influence of Fe content and particle size the on the processing and mechanical properties of low-cost Ti-xFe alloys, Mater. Sci. Eng. A. 527 (2010) 5664–5669. https://doi.org/10.1016/j.msea.2010.05.026.

[20] P. Li, H. Zhang, T. Tong, Z. He, The rapidly solidified β-type Ti–Fe–Sn alloys with high specific strength and low elastic modulus, J. Alloys Compd. 786 (2019) 986–994. https://doi.org/10.1016/j.jallcom.2019.01.346.

[21] S. Ehtemam-Haghighi, G. Cao, L.C. Zhang, Nanoindentation study of mechanical properties of Ti based alloys with Fe and Ta additions, J. Alloys Compd. 692 (2017) 892–897. https://doi.org/10.1016/j.jallcom.2016.09.123.

[22] S. Zhou, Y. Xu, B. Liao, Y. Sun, X. Dai, H. Pan, In-situ synthesis of Ti-Fe-based alloys prepared by the combination of mechanical alloying and laser melting deposition: Microstructure and corrosion resistance, J. Alloys Compd. 768 (2018) 697–706. https://doi.org/10.1016/j.jallcom.2018.07.276.

[23] M.A. Hussein, A.S. Mohammed, N. Al-Aqeeli, Wear characteristics of metallic biomaterials: A review, Materials (Basel). 8 (2015) 2749–2768. https://doi.org/10.3390/ma8052749.

[24] G.D. Revankar, R. Shetty, S.S. Rao, V.N. Gaitonde, Wear resistance enhancement of titanium alloy (Ti-6Al-4V) by ball burnishing process, J. Mater. Res. Technol. 6 (2017) 13–32. https://doi.org/10.1016/j.jmrt.2016.03.007.

[25] F. Xie, X. He, J. Yu, M. Wu, X. He, X. Qu, Fabrication and characterization of porous Ti–4Mo alloy for biomedical applications, J. Porous Mater. (2016) 1–8. https://doi.org/10.1007/s10934-016-0133-z.

[26] F. Xie, X. He, S. Cao, M. Mei, X. Qu, Influence of pore characteristics on microstructure, mechanical properties and corrosion resistance of selective laser sintered porous Ti-Mo alloys for biomedical applications, Electrochim. Acta. 105 (2013) 121–129. https://doi.org/10.1016/j.electacta.2013.04.105.

[27] F.X. Xie, X.B. He, S.L. Cao, X. Lu, X.H. Qu, Structural characterization and electrochemical behavior of a laser-sintered porous Ti-10Mo alloy, Corros. Sci. 67

(2013) 217–224. https://doi.org/10.1016/j.corsci.2012.10.036.
[28] A.C. Alves, I. Sendão, E. Ariza, F. Toptan, P. Ponthiaux, A.M.P. Pinto, Corrosion behaviour of porous Ti intended for biomedical applications, J. Porous Mater. (2016) 1–8. https://doi.org/10.1007/s10934-016-0185-0.
[29] C. Guerra, M. Sancy, M. Walczak, C. Martínez, A. Ringuedé, M. Cassir, J. Han, K. Ogle, H.G. de Melo, V. Salinas, C. Aguilar, Effect of added porosity on a novel porous Ti-Nb-Ta-Fe-Mn alloy exposed to simulated body fluid, Mater. Sci. Eng. C. 111 (2020). https://doi.org/10.1016/j.msec.2020.110758.
[30] N. Eliaz, Corrosion of metallic biomaterials: A review, Materials (Basel). 12 (2019). https://doi.org/10.3390/ma12030407.
[31] C. Guerra, C. Aguilar, D. Guzmán, M. Arancibia, P.A. Rojas, S. Lascano, L. Perez, Production and characterisation of mechanical properties of Ti-Nb-Ta-Mn alloys foams for biomedical applications, Powder Metall. 58 (2015) 12–15. https://doi.org/10.1179/0032589914Z.000000000211.
[32] Y. Alshammari, F. Yang, L. Bolzoni, Mechanical properties and microstructure of Ti-Mn alloys produced via powder metallurgy for biomedical applications, J. Mech. Behav. Biomed. Mater. 91 (2019) 391–397. https://doi.org/10.1016/j.jmbbm.2018.12.005.
[33] D. V. Louzguine, H. Kato, A. Inoue, High strength and ductile binary Ti-Fe composite alloy, J. Alloys Compd. 384 (2004) 10–12. https://doi.org/10.1016/j.jallcom.2004.03.114.
[34] F. Zhang, E. Burkel, Novel Titanium Manganese Alloys and Their Macroporous Foams for Biomedical Applications Prepared by Field Assisted Sintering, Biomed. Eng. Trends Mater. Sci. (2011). https://doi.org/10.5772/12874.
[35] R. Singh, P.D. Lee, R.J. Dashwood, T.C. Lindley, Titanium foams for biomedical applications: a review, Mater. Technol. 25 (2010) 127–136. https://doi.org/10.1179/175355510X12744412709403.
[36] S. Kaur, K. Ghadirinejad, R.H. Oskouei, An overview on the tribological performance of titanium alloys with surface modifications for biomedical applications, Lubricants. 7 (2019). https://doi.org/10.3390/lubricants7080065.
[37] G. Cotogno, E. Commission, Total Hip Arthroplasty, State of the Art, Challenges and Prospects, Italy, 2012. https://doi.org/10.2788/31286.
[38] F. D'Angelo, L. Murena, G. Zatti, P. Cherubino, The unstable total hip replacement, Indian J. Orthop. 42 (2008) 252–259. https://doi.org/10.4103/0019-5413.39667.
[39] H. Dong, Tribological properties of titanium-based alloys, Woodhead Publishing Limited, 2010. https://doi.org/10.1533/9781845699451.1.58.
[40] Xia J, Development of novel surface engineering technology to combat wear of Al-containing intermetallics, The University of Birmingham, 2004.
[41] Z. Liu, F. Ji, M. Wang, T. Zhu, Study on the tribological properties of porous titanium sliding against tungsten carbide YG6, Metals (Basel). 7 (2017). https://doi.org/10.3390/met7010028.
[42] H. Choi, S. Shil'ko, J. Gubicza, H. Choe, Study of the compression and wear-resistance properties of freeze-cast Ti and Ti–5W alloy foams for biomedical applications, J. Mech. Behav. Biomed. Mater. 72 (2017) 66–73. https://doi.org/10.1016/j.jmbbm.2017.04.020.
[43] S. Sathiyanarayanan, C. Marikkannu, P.B. Srinivasan, V. Muthupandi, Corrosion

behaviour of Ti6Al4V and duplex stainless steel (UNS31803) in synthetic bio-fluids, Anti-Corrosion Methods Mater. 49 (2002) 33–37. https://doi.org/10.1108/0003559021043584.

[44] C. Martínez, C. Guerra, D. Silva, M. Cubillos, F. Briones, L. Muñoz, M.A. Páez, C. Aguilar, M. Sancy, Effect of porosity on mechanical and electrochemical properties of Ti–6Al–4V alloy, Electrochim. Acta. (2020) 135858. https://doi.org/10.1016/j.electacta.2020.135858.

[45] S.B. Hong, N. Eliaz, E.M. Sachs, S.M. Allen, R.M. Latanision, Corrosion behavior of advanced titanium-based alloys made by three-dimensional printing (3DPTM) for biomedical applications, Corros. Sci. 43 (2001) 1781–1791. https://doi.org/10.1016/S0010-938X(00)00181-5.

[46] I. Gurappa, Characterization of different materials for corrosion resistance under simulated body fluid conditions, Mater. Charact. 49 (2002) 73–79. https://doi.org/10.1016/S1044-5803(02)00320-0.

[47] J. Fojt, L. Joska, J. Malek, V. Sefl, Corrosion behavior of Ti–39Nb alloy for dentistry, Mater. Sci. Eng. C. 56 (2015) 532–537. https://doi.org/10.1016/j.msec.2015.07.029.

[48] N.T.C. Oliveira, A.C. Guastaldi, Electrochemical stability and corrosion resistance of Ti-Mo alloys for biomedical applications, Acta Biomater. 5 (2009) 399–405. https://doi.org/10.1016/j.actbio.2008.07.010.

[49] K.T. Oh, H.M. Shim, K.N. Kim, Properties of titanium-silver alloys for dental application, J. Biomed. Mater. Res. - Part B Appl. Biomater. 74 (2005) 649–658. https://doi.org/10.1002/jbm.b.30259.

[50] M.J. Hwang, E.J. Park, W.J. Moon, H.J. Song, Y.J. Park, Characterization of passive layers formed on Ti-10wt% (Ag, Au, Pd, or Pt) binary alloys and their effects on galvanic corrosion, Corros. Sci. 96 (2015) 152–159. https://doi.org/10.1016/j.corsci.2015.04.007.

[51] L.H. De Almeida, I.N. Bastos, I.D. Santos, A.J.B. Dutra, C.A. Nunes, S.B. Gabriel, Corrosion resistance of aged Ti-Mo-Nb alloys for biomedical applications, J. Alloys Compd. 615 (2015) S666–S669. https://doi.org/10.1016/j.jallcom.2014.01.173.

[52] J. Lu, Y. Zhao, H. Niu, Y. Zhang, Y. Du, W. Zhang, W. Huo, Electrochemical corrosion behavior and elasticity properties of Ti-6Al-xFe alloys for biomedical applications, Mater. Sci. Eng. C. 62 (2016) 36–44. https://doi.org/10.1016/j.msec.2016.01.019.

[53] Y.F. Xu, Y.F. Xiao, D.Q. Yi, H.Q. Liu, L. Wu, J. Wen, Corrosion behavior of Ti-Nb-Ta-Zr-Fe alloy for biomedical applications in Ringer's solution, Trans. Nonferrous Met. Soc. China (English Ed. 25 (2015) 2556–2563. https://doi.org/10.1016/S1003-6326(15)63875-4.

[54] A.H. Hussein, M.A.H. Gepreel, M.K. Gouda, A.M. Hefnawy, S.H. Kandil, Biocompatibility of new Ti-Nb-Ta base alloys, Mater. Sci. Eng. C. 61 (2016) 574–578. https://doi.org/10.1016/j.msec.2015.12.071.

[55] P.S. Nnamchi, C.S. Obayi, I. Todd, M.W. Rainforth, Mechanical and electrochemical characterisation of new Ti-Mo-Nb-Zr alloys for biomedical applications, J. Mech. Behav. Biomed. Mater. 60 (2016) 68–77. https://doi.org/10.1016/j.jmbbm.2015.12.023.

[56] I. Cvijović-Alagić, Z. Cvijović, S. Mitrović, V. Panić, M. Rakin, Wear and corrosion behaviour of Ti-13Nb-13Zr and Ti-6Al-4V alloys in simulated physiological solution,

Corros. Sci. 53 (2011) 796–808. https://doi.org/10.1016/j.corsci.2010.11.014.
[57] P. Fernandes Santos, M. Niinomi, H. Liu, K. Cho, M. Nakai, A. Trenggono, S. Champagne, H. Hermawan, T. Narushima, Improvement of microstructure, mechanical and corrosion properties of biomedical Ti-Mn alloys by Mo addition, Mater. Des. 110 (2016) 414–424. https://doi.org/10.1016/j.matdes.2016.07.115.
[58] R. Chelariu, G. Bolat, J. Izquierdo, D. Mareci, D.M. Gordin, T. Gloriant, R.M. Souto, Metastable beta Ti-Nb-Mo alloys with improved corrosion resistance in saline solution, Electrochim. Acta. 137 (2014) 280–289. https://doi.org/10.1016/j.electacta.2014.06.021.
[59] V.A. Alves, R.Q. Reis, I.C.B. Santos, D.G. Souza, T.D.F. Gonçalves, M.A. Pereira-da-silva, A. Rossi, L.A. Silva, In situ impedance spectroscopy study of the electrochemical corrosion of Ti and Ti – 6Al – 4V in simulated body fluid at 25 ° C and 37 ° C, Corros. Sci. 51 (2009) 2473–2482. https://doi.org/10.1016/j.corsci.2009.06.035.
[60] M. Itagaki, Y. Hatada, I. Shitanda, K. Watanabe, Complex impedance spectra of porous electrode with fractal structure, Electrochim. Acta. 55 (2010) 6255–6262. https://doi.org/10.1016/j.electacta.2009.10.016.
[61] J. Huang, J. Zhang, Theory of Impedance Response of Porous Electrodes: Simplifications, Inhomogeneities, Non-Stationarities and Applications, J. Electrochem. Soc. 163 (2016) A1983–A2000. https://doi.org/10.1149/2.0901609jes.
[62] A. Lasia, Electrochemical Impedance Spectroscopy and its Applications, Springer New York, New York, NY, 2014. https://doi.org/10.1007/978-1-4614-8933-7.
[63] C. Guerra, M. Sancy, M. Walczak, D. Silva, C. Martínez, B. Tribollet, C. Aguilar, Evolution of oxide film on the internal porosity of Ti-30Nb-13Ta-2Mn alloy foam, Electrochim. Acta. 283 (2018) 676–682. https://doi.org/10.1016/J.ELECTACTA.2018.05.010.
[64] ASTM, ASTM C373-14 Standard Test Method for Water Absorption, Bulk Density, Apparent Porosity, and Apparent Specific Gravity of Fired Whiteware Products, Astm C373-88. 88 (1999) 1–2. https://doi.org/10.1520/C0373-88R06.much.
[65] European Committee for Standardization, EN 1330-4:2010 Non-destructive testing. Terminology-Part4: Terms used in ultrasonic testing, 2010.
[66] S.D.-05 ASTM, Standard Test Method for Laboratory Determination of Pulse Velocities and Ultrasonic Elastic Constants of Rock, Astm. i (2005) 5–11. https://doi.org/10.1520/D2845-08.2.
[67] K. Ogle, S. Weber, Anodic dissolution of 304 stainless steel using atomic emission spectroelectrochemistry, J. Electrochem. Soc. 147 (2000) 1770–1780. https://doi.org/10.1149/1.1393433.
[68] G. Ryan, A. Pandit, D.P. Apatsidis, Fabrication methods of porous metals for use in orthopaedic applications, Biomaterials. 27 (2006) 2651–2670. https://doi.org/10.1016/j.biomaterials.2005.12.002.
[69] F. Matassi, A. Botti, L. Sirleo, C. Carulli, M. Innocenti, Porous metal for orthopedics implants, Clin. Cases Miner. Bone Metab. 10 (2013) 111–115. https://doi.org/10.11138/ccmbm/2013.10.2.111.
[70] W. Sas, K. Gabrys, A. Szymanski, Determination of Poisson's ratio by means of resonant column tests, Electron. J. Polish Agric. Univ. Ser. Civ. Eng. 16 (2013).
[71] V.N. Burlayenko, Modelling Thermal Shock in Functionally Graded Plates with

Finite Element Method, Adv. Mater. Sci. Eng. 2016 (2016). https://doi.org/10.1155/2016/7514638.

[72] V. Kontis, J.E. Bennett, C.D. Mathers, G. Li, K. Foreman, M. Ezzati, Future life expectancy in 35 industrialised countries: projections with a Bayesian model ensemble, Lancet. 389 (2017) 1323–1335. https://doi.org/10.1016/S0140-6736(16)32381-9.

[73] D.A. González-Chica, S. Vanlint, E. Hoon, N. Stocks, Epidemiology of arthritis, chronic back pain, gout, osteoporosis, spondyloarthropathies and rheumatoid arthritis among 1.5 million patients in Australian general practice: NPS MedicineWise MedicineInsight dataset, BMC Musculoskelet. Disord. 19 (2018) 1–10. https://doi.org/10.1186/s12891-018-1941-x.

[74] American Joint Replacement Registry, Fifth AJRR Annual Report on Hip and Knee Arthroplasty Data, 2018.

[75] M. Merola, S. Affatato, Materials for hip prostheses: A review of wear and loading considerations, Materials (Basel). 12 (2019). https://doi.org/10.3390/ma12030495.

[76] J.Y. Rho, R.B. Ashman, C.H. Turner, Young's modulus of trabecular and cortical bone material: Ultrasonic and microtensile measurements, J. Biomech. 26 (1993) 111–119. https://doi.org/10.1016/0021-9290(93)90042-D.

[77] R. Oftadeh, M. Perez-Viloria, J.C. Villa-Camacho, A. Vaziri, A. Nazarian, Biomechanics and mechanobiology of trabecular bone: a review., J. Biomech. Eng. 137 (2015) 0108021. https://doi.org/10.1115/1.4029176.

[78] M. Navarro, A. Michiardi, O. Castaño, J.A. Planell, J.R.S. Interface, M. Navarro, A. Michiardi, O. Castan, Biomaterials in orthopaedics, J. R. Soc. Interface. 5 (2008) 1137–1158. https://doi.org/10.1098/rsif.2008.0151.

[79] P. Silva-Bermudez, S.E. Rodil, An overview of protein adsorption on metal oxide coatings for biomedical implants, Surf. Coatings Technol. 233 (2013) 147–158. https://doi.org/10.1016/j.surfcoat.2013.04.028.

[80] M. Ruzickova, H. Hildebrand, S. Virtanen, On the Stability of Passivity of Ti-Al Alloys in Acidic Environment, 2005. https://doi.org/10.1524/zpch.2005.219.11.1447.

[81] M.-J. Han, H.-C. Choe, C.-H. Chung, Surface characteristics of clinically used dental implant screws, Met. Mater. Int. 11 (2005) 449–456. https://doi.org/10.1007/BF03027494.

[82] D. Martini, M. Fini, M. Franchi, V. De Pasquale, B. Bacchelli, M. Gamberini, A. Tinti, P. Taddei, G. Giavaresi, V. Ottani, M. Raspanti, S. Guizzardi, A. Ruggeri, Detachment of titanium and fluorohydroxyapatite particles in unloaded endosseous implants., Biomaterials. 24 (2003) 1309–16. https://doi.org/10.1016/s0142-9612(02)00508-2.

[83] M. Nakagawa, S. Matsuya, T. Shiraishi, M. Ohta, Effect of fluoride concentration and pH on corrosion behavior of titanium for dental use., J. Dent. Res. 78 (1999) 1568–72. https://doi.org/10.1177/00220345990780091201.

[84] N. Schiff, B. Grosgogeat, M. Lissac, F. Dalard, Influence of fluoride content and pH on the corrosion resistance of titanium and its alloys., Biomaterials. 23 (2002) 1995–2002. https://doi.org/10.1016/s0142-9612(01)00328-3.

[85] Y. Li, C. Yang, H. Zhao, S. Qu, X. Li, Y. Li, New developments of ti-based alloys for biomedical applications, Materials (Basel). 7 (2014) 1709–1800. https://doi.org/10.3390/ma7031709.

[86] A. Mrzejewskiea, R. Hud, J. Sidun, Mechanical Properties and Microstructure of DMLS Ti6Al4V Alloy Dedicated to Biomedical Applications, Materials (Basel). (2019). https://doi.org/10.3390/ma12010176.

[87] K. Karolewska, B. Ligaj, Comparison analysis of titanium alloy Ti6Al4V produced by metallurgical and 3D printing method Comparison Analysis of Titanium Alloy Ti6Al4V Produced by Metallurgical and 3D Printing Method, in: AIP Conf. Proc. 2077, 2019. https://doi.org/10.1063/1.5091886.

[88] A. Mohammadhosseini, D. Fraser, S.H. Masood, M. Jahedi, Microstructure and mechanical properties of Ti-6Al-4V manufactured by electron beam melting process, in: Mater. Res. Innov., 2013. https://doi.org/10.1179/1432891713Z.000000000302.

[89] B. Zhang, X. Pei, C. Zhou, Y. Fan, Q. Jiang, A. Ronca, U.D. Amora, Y. Chen, H. Li, Y. Sun, X. Zhang, The biomimetic design and 3D printing of customized mechanical properties porous Ti6Al4V scaffold for load-bearing bone reconstruction, Mater. Des. 152 (2018) 30–39. https://doi.org/10.1016/j.matdes.2018.04.065.

[90] V. Weißmann, R. Bader, H. Hansmann, N. Laufer, Influence of the structural orientation on the mechanical properties of selective laser melted Ti6Al4V open-porous scaffolds, Mater. Des. 95 (2016) 188–197. https://doi.org/10.1016/j.matdes.2016.01.095.

[91] R. Kumari, W. Pfleging, H. Besser, J. Dutta, Microstructure and corrosion behavior of laser induced periodic patterned titanium based alloy, Opt. Laser Technol. 116 (2019) 196–213. https://doi.org/10.1016/j.optlastec.2019.03.017.

[92] A. Hemmasian, C. Zeng, S. Guo, J. Raush, Corrosion behavior of additively manufactured Ti-6Al-4V parts and the e ff ect of post annealing, Addit. Manuf. 28 (2019) 252–258. https://doi.org/10.1016/j.addma.2019.05.011.

[93] Y.H. Li, N. Chen, H.T. Cui, F. Wang, Fabrication and characterization of porous Ti–10Cu alloy for biomedical application, J. Alloys Compd. 723 (2017) 967–973. https://doi.org/10.1016/j.jallcom.2017.06.321.

[94] D. Sri Maha Vishnu, J. Sure, Y. Liu, R. Vasant Kumar, C. Schwandt, Electrochemical synthesis of porous Ti-Nb alloys for biomedical applications, Mater. Sci. Eng. C. 96 (2019) 466–478. https://doi.org/10.1016/j.msec.2018.11.025.

[95] ASTM E92, Standard Test Method for Vickers Hardness of Metallic Materials, ASTM Int. 82 (2000).

[96] M. Lawrence, Y. Jiang, Bio-aggregates Based Building Materials, 2017. https://doi.org/10.1007/978-94-024-1031-0.

[97] A.K. Swarnakar, O. Van Der Biest, B. Baufeld, Thermal expansion and lattice parameters of shaped metal deposited Ti-6Al-4V, J. Alloys Compd. 509 (2011) 2723–2728. https://doi.org/10.1016/j.jallcom.2010.12.014.

[98] S. Tamilselvi, V. Raman, N. Rajendran, Corrosion behaviour of Ti-6Al-7Nb and Ti-6Al-4V ELI alloys in the simulated body fluid solution by electrochemical impedance spectroscopy, Electrochim. Acta. 52 (2006) 839–846. https://doi.org/10.1016/j.electacta.2006.06.018.

[99] H. Fakhr Nabavi, M. Aliofkhazraei, Morphology, composition and electrochemical properties of bioactive-TiO2/HA on CP-Ti and Ti6Al4V substrates fabricated by alkali treatment of hybrid plasma electrolytic oxidation process (estimation of porosity from EIS results), Surf. Coatings Technol. 375 (2019) 266–291. https://doi.org/10.1016/j.surfcoat.2019.07.032.

[100] M.E. Orazem, B. Tribollet, Constant-Phase Elements in: Electrochemical Impedance Spectroscopy, (2017) 395–419. https://doi.org/10.1002/9781119363682.
[101] A. Son, N. Causse, M. Musiani, M.E. Orazem, N. Pébère, B. Tribollet, V. Vivier, Progress in Organic Coatings Determination of water uptake in organic coatings deposited on 2024 aluminium alloy : Comparison between impedance measurements and gravimetry, Prog. Org. Coatings. 112 (2017) 93–100. https://doi.org/10.1016/j.porgcoat.2017.07.004.
[102] J. Newman, Frequency Dispersion in Capacity Measurements at a Disk Electrode, J. Electrochem. Soc. 117 (1970) 198–203. https://doi.org/10.1149/1.2407464.
[103] J. Newman, T.-A. Karen E, Electrochemical Systems, J. Wiley, 2005.
[104] O. Gharbi, A. Dizon, M.E. Orazem, M.T.T. Tran, B. Tribollet, V. Vivier, From frequency dispersion to ohmic impedance: A new insight on the high-frequency impedance analysis of electrochemical systems, Electrochim. Acta. 320 (2019) 134609. https://doi.org/10.1016/j.electacta.2019.134609.
[105] V.M.W. Huang, V. Vivier, M.E. Orazem, N. Pébère, B. Tribollet, The apparent constant-phase-element behavior of an ideally polarized blocking electrode: A global and local impedance analysis, J. Electrochem. Soc. 154 (2007). https://doi.org/10.1149/1.2398882.
[106] M. Nobial, O. Devos, O.R. Mattos, B. Tribollet, The nitrate reduction process: A way for increasing interfacial pH, J. Electroanal. Chem. 600 (2007) 87–94. https://doi.org/10.1016/j.jelechem.2006.03.003.
[107] B. Hirschorn, M.E. Orazem, B. Tribollet, V. Vivier, I. Frateur, M. Musiani, Electrochimica Acta Determination of effective capacitance and film thickness from constant-phase-element parameters, Electrochim. Acta. 55 (2010) 6218–6227. https://doi.org/10.1016/j.electacta.2009.10.065.
[108] F. Hilario, V. Roche, A.M. Jorge, R.P. Nogueira, Application of the transmission line model for porous electrodes to analyse the impedance response of TiO 2 nanotubes in physiological environment, Electrochim. Acta. 253 (2017) 599–608. https://doi.org/10.1016/j.electacta.2017.09.045.
[109] V. Barranco, M.L. Escudero, M.C. García-Alonso, 3D, chemical and electrochemical characterization of blasted TI6Al4V surfaces: Its influence on the corrosion behaviour, Electrochim. Acta. 52 (2007) 4374–4384. https://doi.org/10.1016/j.electacta.2006.12.031.
[110] J. Navarro Laboulais, A. Amigó Mata, V. Amigó Borrás, A. Igual Muñoz, Electrochemical characterization and passivation behaviour of new beta-titanium alloys (Ti35Nb10Ta-xFe), Electrochim. Acta. 227 (2017) 410–418. https://doi.org/10.1016/j.electacta.2016.12.125.
[111] D.N.G. Krishna, R.P. George, J. Philip, Determination of nanoscale titanium oxide thin film phase composition using X-ray photoelectron spectroscopy valence band analysis, Thin Solid Films. 681 (2019) 58–68. https://doi.org/10.1016/j.tsf.2019.04.044.
[112] K.W. Kang, S. Limandri, G. Castellano, S. Suárez, J. Trincavelli, Thickness determination of anodic titanium oxide films by electron probe microanalysis, Mater. Charact. 130 (2017) 50–55. https://doi.org/10.1016/j.matchar.2017.05.027.
[113] M. Geetha, A.K. Singh, R. Asokamani, A.K. Gogia, Ti based biomaterials, the ultimate choice for orthopaedic implants - A review, Prog. Mater. Sci. 54 (2009) 397–

425. https://doi.org/10.1016/j.pmatsci.2008.06.004.
[114] S. Kurtz, K. Ong, E. Lau, F. Mowat, M. Halpern, Projections of Primary and Revision Hip and Knee Arthroplasty in the United States from 2005 to 2030, 2007. https://doi.org/10.2106/00004623-200704000-00012.
[115] S. Kurtz, K. Ong, E. Lau, F. Mowat, M. Halpern, Projections of Primary and Revision Hip and Knee Arthroplasty in the United States from 2005 to 2030, 2007. https://doi.org/10.2106/00004623-200704000-00012.
[116] J. Lu, P. Ge, Q. Li, W. Zhang, W. Huo, J. Hu, Y. Zhang, Y. Zhao, Effect of microstructure characteristic on mechanical properties and corrosion behavior of new high strength Ti-1300 beta titanium alloy, J. Alloys Compd. 727 (2017) 1126–1135. https://doi.org/10.1016/j.jallcom.2017.08.239.
[117] X. Rao, C.L. Chu, Y.Y. Zheng, Phase composition, microstructure, and mechanical properties of porous Ti–Nb–Zr alloys prepared by a two-step foaming powder metallurgy method, J. Mech. Behav. Biomed. Mater. 34 (2014) 27–36. https://doi.org/10.1016/J.JMBBM.2014.02.001.
[118] A.M.G. Tavares, W.S. Ramos, J.C.G. de Blas, E.S.N. Lopes, R. Caram, W.W. Batista, S.A. Souza, Influence of Si addition on the microstructure and mechanical properties of Ti-35Nb alloy for applications in orthopedic implants, J. Mech. Behav. Biomed. Mater. 51 (2015) 74–87. https://doi.org/10.1016/j.jmbbm.2015.06.035.
[119] A. Lasia, Electrochemical Impedance Spectroscopy and its Applications, Modern Aspects of Electrochemistry, Plenum Publishers, New York, NY, 1999.
[120] R. Jurczakowski, C. Hitz, A. Lasia, Impedance of porous Au based electrodes, J. Electroanal. Chem. 572 (2004) 355–366. https://doi.org/10.1016/J.JELECHEM.2004.01.008.
[121] R. Thampuran, A.W.C. Chua, S.H. Teoh, D.J. Blackwood, K.H.W. Seah, Corrosion behaviour of porous titanium–graphite composites designed for surgical implants, Corros. Sci. 42 (2002) 481–503. https://doi.org/10.1016/s0010-938x(99)00103-1.
[122] S. Affatato, The history of biomaterials used in total hip arthroplasty (THA), Perspect. Total Hip Arthroplast. (2014) 19–36. https://doi.org/10.1533/9781782420392.1.19.
[123] D. Taylor, Long-term performance and failure of orthopaedic devices, Second Edi, Elsevier Ltd, 2009. https://doi.org/10.1533/9781845696610.2.324.
[124] S.C.P. Cachinho, R.N. Correia, Titanium scaffolds for osteointegration: Mechanical, in vitro and corrosion behaviour, J. Mater. Sci. Mater. Med. 19 (2008) 451–457. https://doi.org/10.1007/s10856-006-0052-7.
[125] J. Fojt, Corrosion behaviour of porous Ti – 39Nb alloy for biomedical applications, 71 (2013) 78–83. https://doi.org/10.1016/j.corsci.2013.03.007.
[126] G. Wang, J. Li, K. Lv, W. Zhang, X. Ding, G. Yang, X. Liu, X. Jiang, Surface thermal oxidation on titanium implants to enhance osteogenic activity and in vivo osseointegration, Sci. Rep. 6 (2016). https://doi.org/10.1038/srep31769.
[127] T. Kunii, Y. Mori, H. Tanaka, A. Kogure, M. Kamimura, N. Mori, S. Hanada, N. Masahashi, E. Itoi, Improved Osseointegration of a TiNbSn Alloy with a Low Young's Modulus Treated with Anodic Oxidation, Sci. Rep. 9 (2019). https://doi.org/10.1038/s41598-019-50581-7.
[128] Y.Y. Chang, H.L. Huang, H.J. Chen, C.H. Lai, C.Y. Wen, Antibacterial properties and cytocompatibility of tantalum oxide coatings, Surf. Coatings Technol. 259 (2014) 193–198. https://doi.org/10.1016/j.surfcoat.2014.03.061.

[129] G. Engin, B. Aydemir, H. Özkan Gülsoy, Injection molding of micro-porous titanium alloy with space holder technique, Rare Met. 30 (2011) 565–571. https://doi.org/10.1007/s12598-011-0430-2.
[130] N. Taniguchi, S. Fujibayashi, M. Takemoto, K. Sasaki, B. Otsuki, T. Nakamura, T. Matsushita, T. Kokubo, S. Matsuda, Effect of pore size on bone ingrowth into porous titanium implants fabricated by additive manufacturing: An in vivo experiment, Mater. Sci. Eng. C. 59 (2016) 690–701. https://doi.org/10.1016/j.msec.2015.10.069.
[131] A. Kennedy, Porous Metals and Metal Foams Made from Powders, in: Powder Metall., United Kingdom, 2012.
[132] R.I.M. Asri, W.S.W. Harun, M. Samykano, N.A.C. Lah, S.A.C. Ghani, F. Tarlochan, M.R. Raza, Corrosion and surface modification on biocompatible metals: A review, Mater. Sci. Eng. C. 77 (2017) 1261–1274. https://doi.org/10.1016/j.msec.2017.04.102.
[133] X. Chen, Q. Fu, Y. Jin, M. Li, R. Yang, X. Cui, M. Gong, In vitro studying corrosion behavior of porous titanium coating in dynamic electrolyte, Mater. Sci. Eng. C. 70 (2017) 1071–1075. https://doi.org/10.1016/j.msec.2016.03.044.
[134] A.M. Salantiu, C. Fekete, L. Muresan, P. Pascuta, F. Popa, C. Popa, Anodic oxidation of PM porous titanium for increasing the corrosion resistance of endosseous implants, Mater. Chem. Phys. 149 (2015) 453–459. https://doi.org/10.1016/j.matchemphys.2014.10.044.
[135] M. Chen, E. Zhang, L. Zhang, Microstructure, mechanical properties, bio-corrosion properties and antibacterial properties of Ti-Ag sintered alloys, Mater. Sci. Eng. C. 62 (2016) 350–360. https://doi.org/10.1016/j.msec.2016.01.081.
[136] E. Yılmaz, A. Gökçe, F. Findik, H.O. Gulsoy, O. İyibilgin, Mechanical properties and electrochemical behavior of porous Ti-Nb biomaterials, J. Mech. Behav. Biomed. Mater. 87 (2018) 59–67. https://doi.org/10.1016/j.jmbbm.2018.07.018.
[137] O.E. Barcia, E. D'Elia, I. Frateur, O.R. Mattos, N. Pébère, B. Tribollet, Application of the impedance model of de Levie for the characterization of porous electrodes, in: Electrochim. Acta, Pergamon, 2002: pp. 2109–2116. https://doi.org/10.1016/S0013-4686(02)00081-6.
[138] S.J. Cooper, A. Bertei, D.P. Finegan, N.P. Brandon, Simulated impedance of diffusion in porous media, Electrochim. Acta. 251 (2017) 681–689. https://doi.org/10.1016/j.electacta.2017.07.152.
[139] G. Xie, H. Kanetaka, H. Kato, F. Qin, W. Wang, Intermetallics Porous Ti-based bulk metallic glass with excellent mechanical properties and good biocompatibility, Intermetallics. 105 (2019) 153–162. https://doi.org/10.1016/j.intermet.2018.12.002.
[140] A. V Neimark, M. Thommes, K.S.W. Sing, F. Rodriguez-Reinoso, J.P. Olivier, K. Kaneko, J. Rouquerol, Physisorption of gases, with special reference to the evaluation of surface area and pore size distribution (IUPAC Technical Report), Pure Appl. Chem. 87 (2015) aop. https://doi.org/10.1515/pac-2014-1117.
[141] M.T. Lowell, S. Joan E. Shields, Martin A. Thomas, Characterization of porous solids and powders: surface area, pore size, and density, Kluwer Academic Publishers, 2004. https://doi.org/10.1007/978-1-4020-2303-3.
[142] L. Xu, Metastable Beta Titanium Alloys:Tuning Their Beta Phase Stability and Low-Temperature Martensitic Transformation, Delft University of Technology, 2015.
[143] Q. Li, Y. Zhang, G. He, M. Xu, G. Jiang, D. Wang, A novel approach to fabrication

of three-dimensional porous titanium with controllable structure, Mater. Sci. Eng. C. 71 (2016) 1046–1051. https://doi.org/10.1016/j.msec.2016.11.119.
[144] V.N.V. Munagala, S. Bessette, R. Gauvin, R.R. Chromik, Sliding wear of cold sprayed Ti6Al4V coatings: Effect of porosity and normal load, Wear. 450–451 (2020). https://doi.org/10.1016/j.wear.2020.203268.
[145] B. Dubrujeaud, M. Vardavoulias, M. Jeandin, The role of porosity in the dry sliding wear of a sintered ferrous alloy, Wear. 174 (1994) 155–161. https://doi.org/10.1016/0043-1648(94)90097-3.
[146] C. Guo, J. Chen, J. Zhou, J. Zhao, L. Wang, Y. Yu, H. Zhou, Microstructure and tribological properties of TiAg intermetallic compound coating, Appl. Surf. Sci. 257 (2011) 10692–10698. https://doi.org/10.1016/j.apsusc.2011.07.081.
[147] W.S. Ebhota, T.-C. Jen, Intermetallics Formation and Their Effect on Mechanical Properties of Al-Si-X Alloys, in: Intermet. Compd. - Form. Appl., InTech, 2018: p. 29. https://doi.org/10.5772/intechopen.73188.
[148] D.D. La Grange, N. Goebbels, A. Santana, R. Heuberger, T. Imwinkelried, L. Eschbach, A. Karimi, Effect of niobium onto the tribological behavior of cathodic arc deposited Nb–Ti–N coatings, Wear. 368–369 (2016) 60–69. https://doi.org/10.1016/j.wear.2016.09.003.
[149] X. Liu, P.K. Chu, C. Ding, Surface modification of titanium, titanium alloys, and related materials for biomedical applications, Mater. Sci. Eng. R Reports. 47 (2004) 49–121. https://doi.org/10.1016/j.mser.2004.11.001.
[150] W. Li, C. Cao, S. Yin, Solid-state cold spraying of Ti and its alloys: A literature review, Prog. Mater. Sci. (2019) 100633. https://doi.org/10.1016/j.pmatsci.2019.100633.
[151] L. Ceschini, E. Lanzoni, C. Martini, D. Prandstraller, G. Sambogna, Comparison of dry sliding friction and wear of Ti6Al4V alloy treated by plasma electrolytic oxidation and PVD coating, Wear. 264 (2008) 86–95. https://doi.org/10.1016/j.wear.2007.01.045.
[152] K.A. Kuptsov, A.N. Sheveyko, O.S. Manakova, D.A. Sidorenko, D. V. Shtansky, Comparative investigation of single-layer and multilayer Nb-doped TiC coatings deposited by pulsed vacuum deposition techniques, Surf. Coatings Technol. 385 (2020) 125422. https://doi.org/10.1016/j.surfcoat.2020.125422.
[153] E.R. Booser, Tribology data handbook: an excellent friction, lubrication, and wear resource, 1997.
[154] P. Pawlus, R. Reizer, M. Wieczorowski, G. Krolczyk, Material ratio curve as information on the state of surface topography—A review, Precis. Eng. 65 (2020) 240–258. https://doi.org/10.1016/j.precisioneng.2020.05.008.
[155] A. Czyrska-Filemonowicz, P.A. Buffat, M. Łucki, T. Moskalewicz, W. Rakowski, J.lekki, T. Wierzchoń, Transmission electron microscopy and atomic force microscopy characterisation of titanium-base alloys nitrided under glow discharge, Acta Mater. 53 (2005) 4367–4377. https://doi.org/10.1016/j.actamat.2005.05.035.
[156] L. Chen, Z. Liu, B. Wang, Q. Song, Y. Wan, L. Chen, Surface characterization and tribological performance of anodizing micro-textured aluminum-silicon alloys, Materials (Basel). 12 (2019). https://doi.org/10.3390/ma12111862.
[157] Q. Chen, D.Y. Li, B. Cook, Is porosity always detrimental to the wear resistance of materials?-A computational study on the effect of porosity on erosive wear of TiC/Cu

composites, Wear. 267 (2009) 1153–1159. https://doi.org/10.1016/j.wear.2008.12.058.

[158] J. Ureña, E. Tabares, S. Tsipas, A. Jiménez-Morales, E. Gordo, Dry sliding wear behaviour of β-type Ti-Nb and Ti-Mo surfaces designed by diffusion treatments for biomedical applications, J. Mech. Behav. Biomed. Mater. 91 (2019) 335–344. https://doi.org/10.1016/j.jmbbm.2018.12.029.

[159] M. Dinu, L. Braic, S.C. Padmanabhan, M.A. Morris, I. Titorencu, V. Pruna, A. Parau, N. Romanchikova, L.F. Petrik, A. Vladescu, Characterization of electron beam deposited Nb2O5 coatings for biomedical applications, J. Mech. Behav. Biomed. Mater. 103 (2020) 103582. https://doi.org/10.1016/j.jmbbm.2019.103582.

[160] F. Haftlang, A. Zarei-Hanzaki, H.R. Abedi, In-situ frictional grain refinement of Ti–29Nb–14Ta–4.5Zr bio-alloy during high-speed sliding wear, Mater. Lett. 261 (2020) 127083. https://doi.org/10.1016/j.matlet.2019.127083.